IN-SITU TEM STUDIES: HEAT-TREATMENT AND CORROSION

Proefschrift

ter verkrijging van de graad van doctor
aan de Technische Universiteit Delft,
op gezag van de Rector Magnificus prof. ir. K.C.A.M. Luyben,
voorzitter van het College voor Promoties,
in het openbaar te verdedigen
op dinsdag 4 februari 2014 om 10:00 uur

door

Sai Rama Krishna MALLADI
Master of Technology in Materials Science & Engineering,
Indian Institute of Technology Kanpur, India
Geboren te Haiderabad, India

Dit proefschrift is goedgekeurd door de promotor(en):

Prof.dr. H.W. Zandbergen

Samenstelling promotiecommissie:

Rector Magnificus,	voorzitter
Prof.dr. H.W. Zandbergen	Technische Universiteit Delft, promotor
Dr.ir. F.D. Tichelaar	Technische Universiteit Delft
Prof.dr. C. Dekker	Technische Universiteit Delft
Prof.dr. E.H. Brück	Technische Universiteit Delft
Prof.dr. R.E. Dunin-Borkowski	ER-C, Forschungszentrum Jülich RWTH Aachen University, DTU Denmark
Prof.dr. C.A. Volkert	Georg-August-Universität Göttingen
Dr.ir. F. Hannour	TATA Steel Europe
Prof.dr. J. Sietsma	Technische Universiteit Delft, reservelid

This research was carried out under project number MC6.05222 in the framework of the Research Program of Materials innovation institute M2i in the Netherlands (www.m2i.nl)

Keywords: Transmission Electron Microscopy, *in situ*, heat-treatment, corrosion, aluminium alloys
Printed by: Ipskamp Drukkers B.V.
Cover design: Sairam Malladi, thanks to Olaf Weller for improvements

ISBN 978-9-491-90904-7

Author email: srk.malladi@gmail.com

Dedicated to
Late Professor Ramamurthy Balasubramaniam
15/04/1961 — 9/12/2009
Teacher par excellence

CONTENTS

Chapter 1

Chapter 2

Chapter 3

Chapter 4

Chapter 5

Chapter 6

Chapter 7

Chapter 8

Chapter 1 ALUMINIUM ALLOYS

"This valuable metal possesses the whiteness of silver, the indestructibility of gold, the tenacity of iron, the fusibility of copper, the lightness of glass. It is easily wrought, is very widely distributed, forming the base of most rocks, is three times lighter than iron, and seems to have been created for express purpose of furnishing us with the material for our projectile." - Jules Verne, "From the Earth to the Moon", 1865

Aluminium (Al) is the most abundant metallic element in the earth's crust,[1] usually existing in a combined state with other elements like iron (Fe), silicon (Si) and oxygen (O). Bauxite, which is a mixture of one or more aluminium hydroxide ($Al(OH)_3$) minerals, is the chief mineral for Al production. Pure aluminium oxide (Al_2O_3) is extracted from bauxite by the *Bayer Process* and pure metallic Al is obtained from this oxide by electrolysis, known as the *Hall Process*.[2] Al and its alloys are attractive due to a combination of unique properties[i] like: exceptional strength-weight ratio — pure Al has a specific strength of 214 kN.m/kg, comparable to that of stainless steel;[3] ductility and malleability — Al is the second most malleable and the sixth most ductile metal,[4] excellent thermal and electrical conductivity — Al comes only behind silver (Ag), copper (Cu) and gold (Au) in terms of conductivity;[5,6] good corrosion resistance — pure Al shows passivation, the formation of a protective oxide film which enhances its corrosion resistance[7]; recyclability — recycling Al uses about 5 % of the energy required for its extraction from bauxite;[8] as well as non-toxicity, hence used in food packaging.[9] These distinctive properties make Al and its alloys an important class of materials and are ranked second only to Fe and steel in the metals market.[3]

Al alloys find major applications in automotive and aerospace industry, building and construction, containers and packaging, electrical and heat transfer engineering. The pie chart in Figure 1.1 illustrates the main end-use markets for Al products in Europe in 2011.[10] The transportation industry (automotive and aerospace) consumes a large share of Al alloys and Figure 1.2 shows the key components made out of Al alloys for an automobile and a commercial jet.

---

[i] As there are several Al alloys for specific applications, the most common properties derived from pure Al are mentioned here

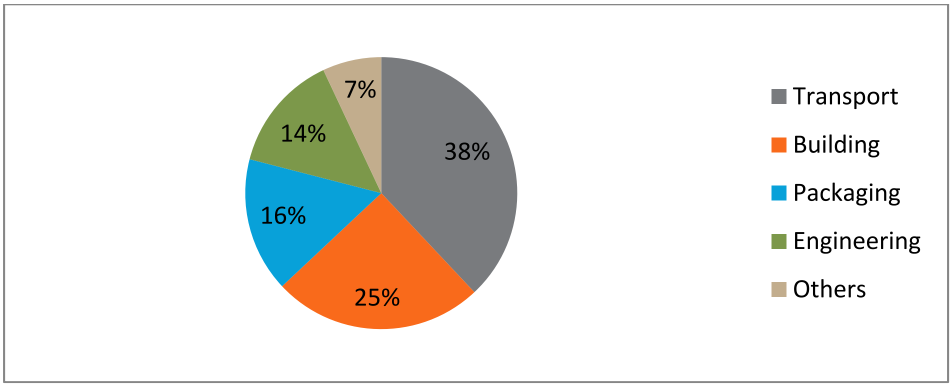

Figure 1.1: Main end-use markets for Al products in Europe, 2011.[10]

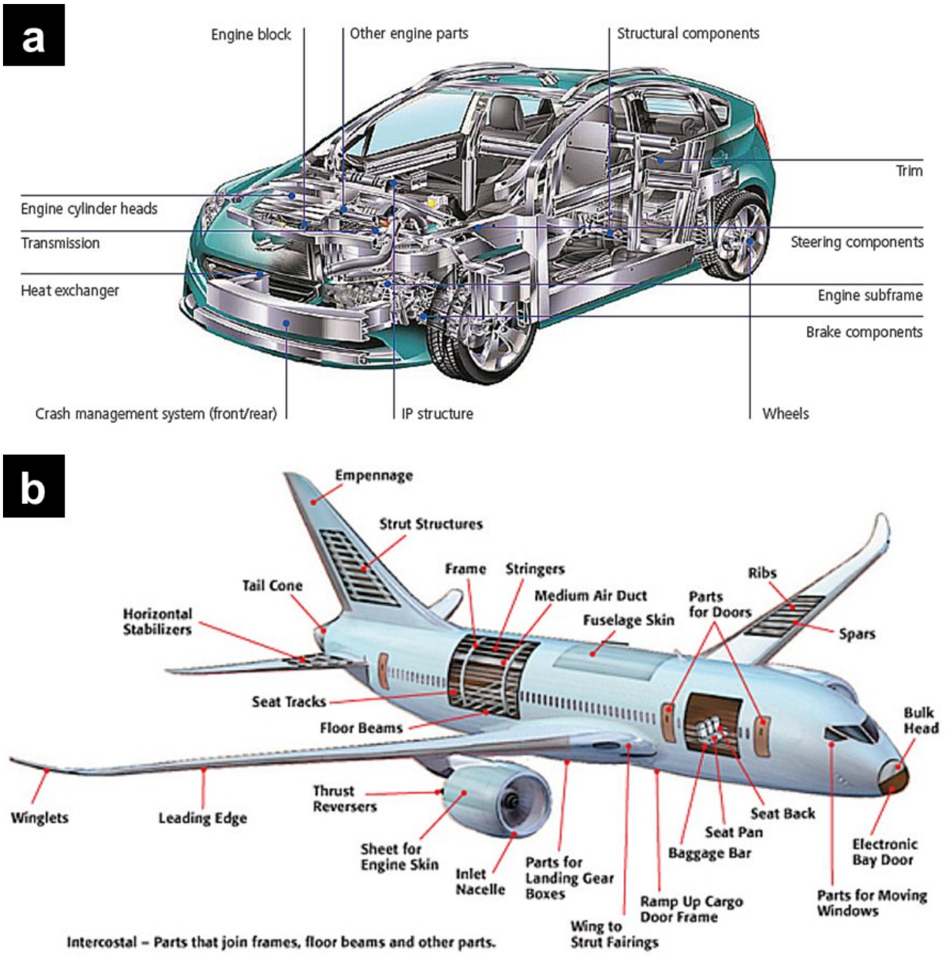

Figure 1.2: Key components of (a) an automobile[11] *and (B) a commercial air craft manufactured from Al alloys.*[12]

It is estimated that approximately 80% of the weight of a commercial jet is contributed by Al alloys.[13] Owing to good strength, low weight, as well as good corrosion resistance at a reasonable cost, there is an ever increasing demand for Al alloys in the automotive and aerospace industry. According to a recent report by the European Aluminium Association, the amount of Al used per car produced in Europe almost tripled between 1990 and 2012, increasing from 50 kg to 140 kg. This amount is predicted to rise to 160 kg by 2020, and even reach as much as 180 kg.[11]

1. Classification and designation of Al alloys

Like all pure metals, Al cannot be readily used in applications which demand good mechanical properties. Therefore, other elements are added to Al, primarily to improve strength.[2,3] Most metals alloy with Al but only a few have sufficient solid solubility to serve as major alloying additions. Over three hundred Al alloy compositions are generally recognised, and many additional variations have been developed.[14] Of the commonly used elements, zinc (Zn), magnesium (Mg), Cu and Si have significant solubilities and several other elements with solubilities as low as 1 atomic% confer improvements to alloy properties. Transition metals like chromium (Cr), manganese (Mn) and zirconium (Zr) are used primarily to form compounds that control the grain structure.[15]

The simplest classification of Al alloys is based on the fabrication process and they are classified either as cast or wrought alloys.[3] A more elaborate classification of these alloys is based on the hardening mechanism. The first group consists of those alloys in which the mechanical properties are controlled by work hardening and annealing, like commercially pure Al and alloys based on Al-Mg and Al-Mn. The other group is the alloys which respond to precipitation hardening. The major examples of this class are alloys such as Al-Cu-Mg, Al-Mg-Si and Al-Zn-Mg-Cu. To identify the Al alloys, a four digit numerical designation system is adapted, the details of which are given in Appendix A.

2. Physical metallurgy of Al alloys

The structure — both crystal structure of the phases present, as well as the microstructure — determines most of the properties of a material. The properties of Al alloys depend on a complex interaction of chemical composition, morphology and the distribution of phases developed during solidification, thermal treatments and deformation processing.[16] As it is not possible to discuss every microstructural aspect, only a few significant ones influencing the mechanical properties as well as the corrosion behaviour of Al alloys are briefly discussed here.

In Al alloys, the strengthening can occur by either one or a combination of these mechanisms: solid solution strengthening, work- or strain- hardening, and in case of heat-treatable alloys by precipitation hardening.[15-17]

In case of solid solution strengthening, the alloying elements dissolve completely in the Al matrix to form a solid solution. The local distortion at solute atoms of the Al lattice obstructs the dislocation motion leading to increased strength.[17] Work- or strain-hardening occurs during the deformation of metals and alloys. During deformation, if the dislocation generation and multiplication occurs faster than annihilation by dynamic recovery, the dislocation density increases. During this process, dislocation tangles, cells and sub-grain walls (deformation substructures) are formed resulting in a change in the grain shapes and internal structure. All these microstructural changes decrease the mean free slip distance and enhance the strength.[17,18] Strain-hardening is the main strengthening process for those alloys which do not respond to heat-treatment. For heat-treatable alloys, strain-hardening may supplement the strength developed by precipitation hardening.[15] Precipitation hardening is a form of dispersion strengthening, which is achieved when alloying elements are added to form very fine insoluble dispersion of intermetallic phases.[19]

A common feature observed in most of the Al alloys is a very high density of intermetallic particles, Figure 1.3. The particles precipitating on certain crystallographic planes contribute to the strength by increasing the resistance to deformation by slip. The intermetallic particles in Al alloys can be classified into the following categories:[20]

i. Precipitates formed by nucleation and growth from a supersaturated solid solution during natural or low-temperature artificial ageing.
    a. These range in size from 1 nm to fractions of a micrometre.
    b. Can be spherical, needles, laths, plates among other shapes.
    c. Mainly elements like Cu, Mg, Si, Zn, and Lithium (Li) lead to precipitation.
ii. Constituent particles which are formed during alloy solidification and are not appreciably dissolved during subsequent processing.
    a. Range from few tenths of a micrometre up to 10 micrometres.
    b. Comparatively large and irregularly shaped.
    c. Cu, Fe, Si, Mn and Mg are most commonly found in these particles.
iii. Dispersoids, which are small particles comprising alloying elements that are highly insoluble in Al. These elements tend to segregate as clusters/nodules in the solutionised state, and typically are responsible for grain refining.
    a. Size typically ranges from 0.05 - 0.5 micrometre.
    b. Usually nodular shaped or sometimes irregularly shaped.
    c. Cr, titanium (Ti), Zr and Mn are common dispersoid formers.

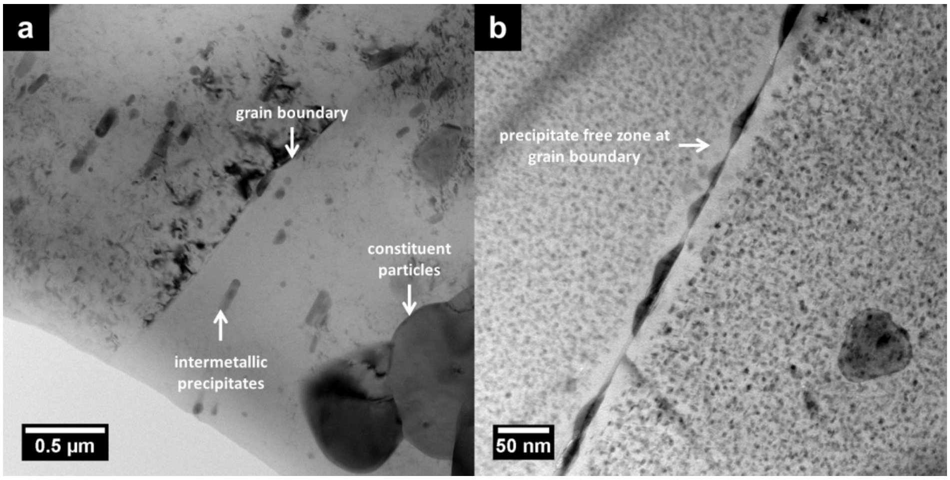

Figure 1.3: Bright-field transmission electron micrographs showing the typical microstructural variations in specimens of Al alloys (a) 2024-T3 and (b) 7075-T76

The formation of intermetallic precipitates is achieved by controlled precipitation during heat-treatment.[3] If there is a decrease in solid solubility of one or more of the alloying elements with decreasing temperature, the precipitation can precisely be controlled by heat treatment.[21] The heat-treatment, commonly known as age hardening involves the following stages:

i. Solution treatment at a relatively high temperature within the single-phase region to dissolve the alloying elements.
ii. Rapid cooling or quenching to a low temperature (usually room temperature) to obtain a super saturated solid solution (SSSS) of these elements in Al.
iii. Controlled decomposition of this SSSS to form a finely dispersed precipitate either at ambient temperatures (natural ageing) or at elevated temperatures (artificial ageing) for convenient times.

Success in stimulating the formation of dispersions of precipitates is achieved by employing different strategies like duplex-ageing treatments, co-precipitation of two or more equilibrium phases, intermediate phases and dispersoids.[15] The presence of these fine intermetallic precipitates in the Al matrix is vital for improving the strength of the Al alloys. Alternatively, variations in the local density of precipitates, the compositional variations associated with the precipitates,[22] the formation of solute free zones,[23] grain boundary segregation of solute elements, formation of precipitate free zones, effect the material properties.[24] For example, grain boundary segregation in metals and alloys is known to be severely detrimental to many important mechanical properties, causing the problems of grain boundary fracture in temper brittleness, creep embrittlement, Stress relief cracking of weldments, grain boundary corrosion, intergranular stress corrosion cracking, hydrogen embrittlement and environmentally assisted fatigue. Segregation can also affect grain boundary migration rates as well as grain boundary diffusivity.[24] Finally, it can be summarised that the most dominant microstructural feature of many of the commercial Al alloys is the presence of intermetallic particles.

3. Corrosion behaviour of Al alloys

Corrosion is an inevitable problem for most metal alloys in everyday use. Pure Al in general has excellent corrosion and oxidation resistance, owing to its stable passive film.[7] Nonetheless, most of the Al alloys are prone to certain forms of corrosion, depending on the environment.[25] Corrosion in Al alloys depends on number of factors that are intrinsic to the alloy, the medium and conditions of use. The intrinsic factors can be the type of alloying elements added, the formation of intermetallic precipitates, the presence of segregated areas like precipitate-free zones, solute depleted zones etc., which exhibit distinctly different electrochemical characteristics[20,22] compared to the surrounding microstructure, leading to the formation of galvanic couples.[ii] When exposed to an environment, the inherent galvanic couples make the Al alloys susceptible to a spontaneous electrochemical reaction[iii] leading to the initiation of corrosion. Depending on the electrochemical potential and the type of the reaction, the microstructural variations could behave either *anodic* or *cathodic* with respect to the surrounding region.[iv] The anodic phases can dissolve straight away in the corrosive environment, but if these second phases act as cathodes, they promote the reduction of hydrogen or oxygen and to support the anodic reaction and a corrosive attack in the matrix around the cathodic sites is observed.[26-28] Furthermore, the alloying elements may react with oxidising environments at different rates, resulting in an inhomogeneous oxide film. This may either strengthen the protective properties of the oxide film by forming mixed oxides, if their structures are compatible, or, weaken these protective properties. Also, the presence of reactive species in the environment is severely detrimental to the corrosion resistance. Certain anions like chloride (Cl^-) initiate pitting in the passive film which may lead to an aggressive localised attack.[27-29]

In Al and its alloys, pitting corrosion, intergranular corrosion and exfoliation are the most commonly observed forms of localised corrosion.[25] Although classified as different forms, all of them are more or less interrelated. Localised corrosion of Al alloys, as illustrated in Figure 1.4, may initiate randomly at any grain boundary or precipitate-matrix interface. Pitting is characterised by formation of irregularly shaped cavities on the surface of the metal.[30,31] This type of attack is normally encountered in almost all alloys and in all environments. Pitting can be locally accelerated by crevices

---

[ii] Microstructural variations with different electrochemical potentials can act either as anode or cathode, when in contact with each other form a galvanic couple.

[iii] Any chemical reaction that involves a transfer of charge (electrons) is called an electrochemical reaction.

[iv] Charge transfer can either happen by gain of electrons, reduction, which happens at the *cathode*, or by the loss of electrons, oxidation, which happens at *anode*.

and contact with dissimilar metals. The depths of these pits depend on several parameters related to the type of alloy and environmental conditions and can reach a limiting value. Intergranular (intercrystalline) corrosion (IGC) can occur randomly over the entire surface of an alloy but the corrosion is limited to the immediate grain boundary region and is often not apparent.[25]

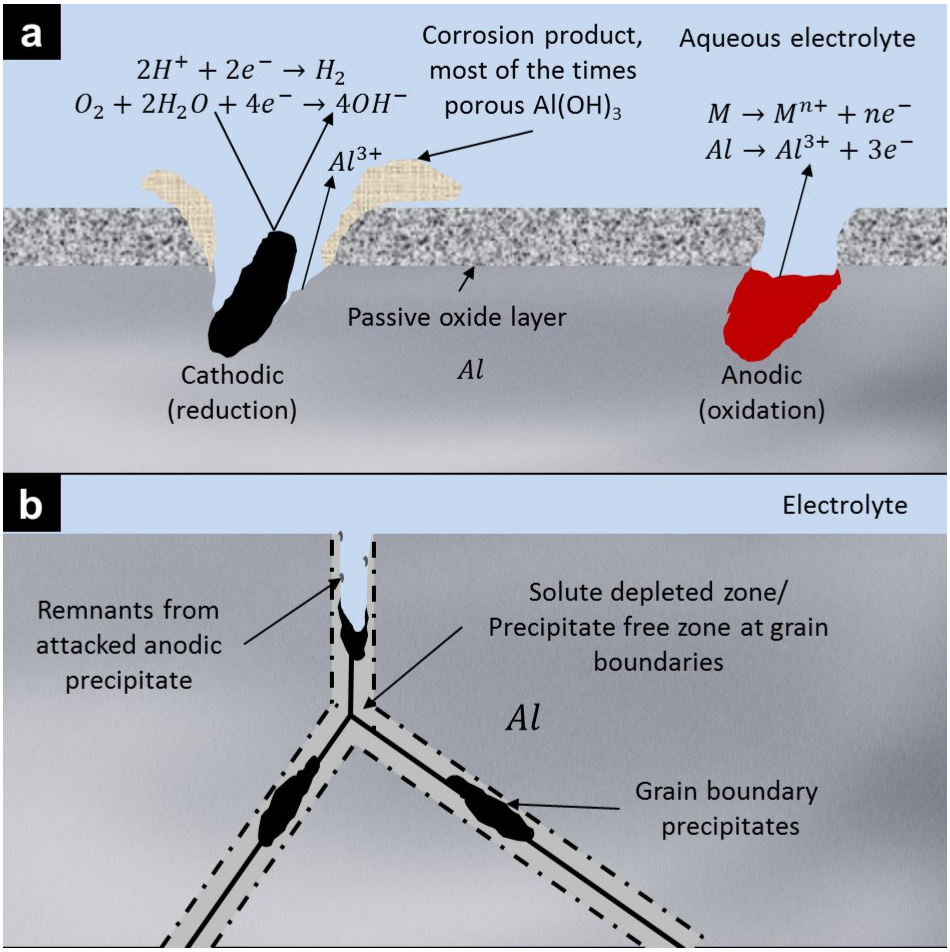

Figure 1.4: Schematic illustrations showing cross-sectional view of localised corrosive attack in Al alloys: (a) around a cathodic precipitate, usually regarded as peripheral trenching, and the selective attack of an anodic precipitate, called de-alloying. The common anodic and cathodic reactions possible in the aqueous environments are also given here; (b) When a network of precipitates is distributed along grain boundaries (also shown in Figure 1.3b), the corrosive attack propagates along the grain boundaries and the solute depleted zones, causing an intergranular attack.

The compositional differences between precipitates on the grain boundaries, solute depleted grain margins and the solute grain interior, lead to a localised galvanic couple. IGC propagates more aggressively than pitting but also reaches a limiting depth. Once the limiting depth is reached, the intergranular attack spreads laterally and results in splitting or exfoliation of the grains. Furthermore, the IGC cracks have much sharper tips than pitting corrosion, hence act as drastic stress risers and have a more damaging contribution to corrosion fatigue. However, it can be said that both pitting and IGC result from a local breakdown of the passive film that forms on the surface. When an intermetallic particle or the matrix of a grain is attacked, it is called pitting, whereas attack restricted to grain boundary regions is called IGC. It therefore follows that understanding the corrosion behaviour of Al alloys is an important area of study due to the complexity of the alloy system as well as the randomness of the initiation and propagation of the corrosion attack.[30-33]

The simplest methods to evaluate corrosion damage are based on the idea that when a material is exposed to corrosive environment for prolonged periods, the weight change due to corrosion can be monitored.[25] However, when it comes to localised corrosion like in the case of Al alloys, the weight loss or gain due to corrosion or the formation of corrosion product are not significant and hence the areas attacked are visually inspected. The methods to evaluate the localised corrosion damage in Al alloys are given in Appendix B.[34] The electrochemical methods to investigate corrosion are based on the principle of probing the electrical double layer which is formed at the metal-electrolyte interface.[35] These include techniques like potentiodynamic polarisation, Tafel extrapolation, polarisation resistance, electrochemical impedance spectroscopy; polarisation techniques to investigate localised corrosion like scratch re-passivation, potential step re-passivation to name a few.[36-38] More recently, the development of surface probe microscopy techniques like scanning vibrating electrode technique (SVET),[39] scanning tunnelling microscopy (STM),[40] atomic force microscopy (AFM),[41] scanning electrochemical microscopy (SECM)[42] and scanning kelvin probe force microscopy (SKPFM)[43] allows the possibility to investigate the localised corrosion quasi *in situ*.[v] All these experimental techniques combined with surface analysis techniques[44] (Appendix C) on model[22,32,45-49] as well as commercial alloys[26,30,31,33,50-55] have contributed to a wealth of knowledge on localised corrosion in Al alloys, which can briefly be summarised as follows:

i. The dominant feature of alloy microstructures responsible for localised corrosion is the distribution of second phase particles and the metallurgical processes like heat treatment given to the alloys severely affect the distribution of these second phase particles.
ii. In pure metals, pitting resistance is dependent on the stability of the passive film, however in case of Al alloys, pitting is influenced by the intermetallic particles which exhibit different surface film characteristics to the matrix.
iii. The pit initiation also depends on the electrolyte and this is favoured mostly in the presence of strong anions like the halides.

---

[v] In a quasi *in situ* study, the same location on a sample is re-visited after exposing to the corrosive environment repeatedly for short time intervals

iv. When the particles are more noble than the matrix, a circumferential attack is observed in the matrix and the other kind of attack is the selective dissolution of the intermetallic particle itself.

v. On enrichment of grain boundaries either by intermetallic precipitates or by specific alloying elements, due to the galvanic coupling there is an attack at grain boundaries.

4. Scope of present research

Corrosion studies carried out thus far have predominantly been *ex situ*,[vi] giving an indication of the behaviour of second phase particles (around micron size), analysed over a relatively large area. Quite often, the origin of corrosion is due to second phase particles of the order of a few tens of nanometres and interfaces which are sometimes only a nanometre thick and in order to gain understanding of what is happening at this scale, it is necessary to use a microscopic technique like scanning probe microscopy or transmission electron microscopy (TEM). There have been a few attempts using AFM and SKPFM to follow the corrosion attack quasi *in situ*.[40,41,56,57] However, using the surface probe microscopic techniques it is difficult to follow the exact moment of initiation and propagation of a corrosive attack instantaneously as the images are obtained by scanning a tip over an area and the creation of trenches as well as gas evolution during the reaction could interfere with the image acquisition. TEM on the other hand has been used to investigate the localised corrosion in Al alloys *ex situ*.[58-64] In order to gain insights into the initiation and propagation of localised corrosion, it is necessary to carry out *in situ*[vii] studies. The objective of the current study is to investigate localised corrosion in a commercial Al alloy *in situ* in a TEM using a microelectromechanical system (MEMS) based device called a nanoreactor. The aim of this study is to follow the corrosion phenomena at a sub-nanometre scale during the exposure to a liquid-gas mixture, to gain insights on the initiation of the corrosion process.

5. Organisation of the thesis

This thesis is divided in to the following sections: the general introduction to Al alloys and TEM in chapters 1 and 2, the experimental studies and results in chapters 3 to 7, and the conclusions and suggestions for future work in chapter 8. The general introduction to Al alloys, their microstructure and properties, principles of localised corrosion in Al alloys have been introduced in chapter 1. This is followed by a general introduction to TEM, analytical TEM techniques in chapter 2. The specimen preparation methods and *in situ* TEM studies have also been introduced here. The

---

[vi] The post-mortem study after corrosion attack, either by exposing to a reactive environment in a chamber or in an electrochemical cell

[vii] The studies using surface probe microscopy techniques in the literature are often claimed as *in situ* studies, which are in fact quasi *in situ*. The term *in situ* is more appropriate for studies carried out in a TEM

details on microstructural evolution while heating a commercial Al alloy AA2024-T3 *in situ* are given in chapter 3. For carrying out *in situ* corrosion studies, the following approach has been adapted: first a suitable electrolyte for carrying *in situ* TEM studies is decided through *ex situ* TEM studies, in chapter 4, and a quasi *in situ* approach to investigate the localised corrosion in AA2024-T3 is presented in chapter 5. The real *in situ* experiments using the nanoreactor are given in chapter 6. As it is important to not just look at initiation of corrosion but also the inhibition of corrosion, the quasi *in situ* approach has been adapted in chapter 7 to investigate the corrosion protection of AA2024-T3 in sodium chloride-cerium chloride solutions. Finally, the thesis ends with chapter 8 on conclusions and possibilities for future studies.

References

1 *Abundance in Earth's Crust for all the elements in the Periodic Table*, <http://www.periodictable.com/Properties/A/CrustAbundance.html> (

2 Polmear, I. J. in *Light Alloys - From traditional alloys to nanocrystals* Ch. 1, 1-28 (Butterworth-Heinemann, 2006).

3 Smith, W. F. in *Structure and properties of engineering alloys* Ch. 5, 177-230 (McGraw-Hill, 1993).

4 *Aluminium*, <http://www.fact-index.com/a/al/aluminium.html> (

5 *Thermal Conductivity for all the elements in the Periodic Table*, <http://www.periodictable.com/Properties/A/ThermalConductivity.html> (

6 *Electrical Conductivity for all the elements in the Periodic Table*, <http://www.periodictable.com/Properties/A/ElectricalConductivity.html> (

7 Vargel, C. in *Corrosion of Aluminium* Ch. B.1, 81-109 (Elsevier, 2004).

8 in *The Economist* (2007).

9 *All about aluminium*, <http://www.aluminiumleader.com/en/around/packing/> (

10 *Consumption - End-use markets for aluminium products 2010*, <http://www.alueurope.eu/consumption-end-use-markets-for-aluminium-products-2010/> (

11 Aluminium in cars: Unlocking the light-weighting potential. (Brussels, Belgium, 2013).

12 *Aerospace Aluminum | Aircraft Aluminum, Aerospace Aluminum Sheet, Plate, Rod, Bar, Tube, Redraw Rod, Extrusion Billet, Forge Stock*, <http://www.kaiseraluminum.com/markets-we-serve/aerospace/> (

13 *Aluminum | Aircraft*, <http://www.aluminum.org/Content/NavigationMenu/TheIndustry/TransportationMarket/Aircraft/default.htm> (

14 Rooy, E. L. in *ASM Metal Hanbook: Properties and Selection: Nonferrous Alloys and Special-Purpose Materials* Vol. 2 17-38 (ASM International, 1992).

15 Polmear, I. J. in *Light Alloys - From traditional alloys to nanocrystals* Ch. 2, 29-96 (Butterworth-Heinemann, 2006).

16 Tiryakioglu, M. & Staley, J. T. in *Handbook of Aluminium: Physical Metallurgy and Processes* Vol. 1 (eds George E Totten & Scott D MacKenzie) Ch. 3, 81-210 (Marcel-Dekker, 2003).

17 Katgerman, L. & Eskin, D. in *Handbook of Aluminiun: Physical Metallurgy and Processes* Vol. 1 (eds George E Totten & Scott D MacKenzie) Ch. 5, 259-303 (Marcel-Dekker, 2003).

18 Padhila, A. F. & Plaut, R. L. in *Handbook of Aluminium: Alloy Production and Materials Manufacturing* Vol. 2 (eds George E Totten & Scott D MacKenzie) Ch. 6, 193-220 (Marcel-Dekker, 2003).

19 Gladman, T. Precipitation hardening in metals. *Materials Science and Technology* **15**, 30-36 (1999).

20 Birbilis, N. & Buchheit, R. G. Electrochemical Characteristics of Intermetallic Phases in Aluminum Alloys. *Journal of The Electrochemical Society* **152**, B140-B151, doi:10.1149/1.1869984 (2005).

21 in *ASM Metal Handbook: Heat Treating* Vol. 4 1861-1959 (ASM International, 1991).

22 Buchheit, R. G. A Compilation of Corrosion Potentials Reported for Intermetallic Phases in Aluminum Alloys. *Journal of The Electrochemical Society* **142**, 3994-3996 (1995).

23 Unwin, P. N. T., Lorimer, G. W. & Nicholson, R. B. The origin of the grain boundary precipitate free zone. *Acta Metallurgica* **17**, 1363-1377 (1969).

24 Seah, M. P. Grain boundary segregation. *Journal of Physics F: Metal Physics* **10**, 1043 (1980).

25 Vargel, C. in *Corrosion of Aluminium* Ch. B.2, 81-109 (Elsevier, 2004).

26 Guillaumin, V. & Mankowski, G. Localized corrosion of 2024 T351 aluminium alloy in chloride media. *Corrosion Science* **41**, 421-438 (1999).

27 Foley, R. T. & Nguyen, T. H. The Chemical Nature of Aluminum Corrosion. *Journal of The Electrochemical Society* **129**, 464-467 (1982).

28 Foley, R. T. Localized corrosion of Aluminium Alloys - A Review. *Corrosion* **42**, 277-288 (1986).

29 Dallek, S. & Foley, R. T. Mechanism of Pit Initiation on Aluminum Alloy Type 7075. *Journal of The Electrochemical Society* **123**, 1775-1779 (1976).

30 Blanc, C. & Mankowski, G. Susceptibility to pitting corrosion of 6056 aluminium alloy. *Corrosion Science* **39**, 949-959 (1997).

31 Blanc, C. & Mankowski, G. Pit propagation rate on the 2024 and 6056 aluminium alloys. *Corrosion Science* **40**, 411-429 (1998).

32 Galvele, J. R. & de De Micheli, S. M. Mechanism of intergranular corrosion of Al-Cu alloys. *Corrosion Science* **10**, 795-807 (1970).

33 Blanc, C., Lavelle, B. & Mankowski, G. The role of precipitates enriched with copper on the susceptibility to pitting corrosion of the 2024 aluminium alloy. *Corrosion Science* **39**, 495-510 (1997).

34 Lifka, B. W. in *Corrosion Tests and Standards* (ed R Baboian) Ch. 47, 547-557 (ASTM International, 2005).

35 Tait, S. W. in *An introduction to electrochemical corrosion testing for practicing engineers and scientists* Ch. 1, 1-16 (Pari O Docs, 1994).

36 Scully, J. R. & Taylor, D. W. in *ASM Metal Hanbook: Corrosion* Vol. 13 473-492 (ASM International, 1987).

37 Scully, J. R. in *Corrosion Tests and Standards* (ed R Baboian) Ch. 7, 107-138 (ASTM International, 2005).

38 Meng, Q. & Frankel, G. S. Effect of Cu Content on Corrosion Behavior of 7xxx Series Aluminum Alloys. *Journal of The Electrochemical Society* **151**, B271-B283-B271-B283 (2004).

39 Isaacs, H. S. The measurement of the galvanic corrosion of soldered copper using the scanning vibrating electrode technique. *Corrosion Science* **28**, 547-558, doi:Doi: 10.1016/0010-938x(88)90023-6 (1988).

40 González-Martín, A., Bhardwaj, R. C. & Bockris, J. O. M. Some *in-situ* STM contributions to the characterization of electrochemical systems. *Journal of Applied Electrochemistry* **23**, 531-546 (1993).

41 Kowal, K., DeLuccia, J., Josefowicz, J. Y., Laird, C. & Farrington, G. C. In Situ Atomic Force Microscopy Observations of the Corrosion Behavior of Aluminum-Copper Alloys. *Journal of The Electrochemical Society* **143**, 2471-2481 (1996).

42 Bard, A. J., Fan, F. R. F., Kwak, J. & Lev, O. Scanning electrochemical microscopy. Introduction and principles. *Analytical Chemistry* **61**, 132-138 (1989).

43 de Wit, J. H. W. New knowledge on localized corrosion obtained from local measuring techniques. *Electrochimica Acta* **46**, 3641-3650 (2001).

44 Graham, M. J. The application of surface techniques in understanding corrosion phenomena and mechanisms. *Corrosion Science* **37**, 1377-1397 (1995).

45 Muller, I. L. & Galvele, J. R. Pitting potential of high purity binary aluminium alloys-I. Al-Cu alloys. Pitting and intergranular corrosion. *Corrosion Science* **17**, 179-193 (1977).

46 Muller, I. L. & Galvele, J. R. Pitting potential of high purity binary aluminium alloys-II. Al-Mg and Al-Zn alloys. *Corrosion Science* **17**, 995-1007 (1977).

47 Mazurkiewicz, B. & Piotrowski, A. The electrochemical behaviour of the Al_2Cu intermetallic compound. *Corrosion Science* **23**, 697-707 (1983).

48 Scully, J., Peebles, D., Romig, A., Frear, D. & Hills, C. Metallurgical factors influencing the corrosion of aluminum, Al-Cu, and Al-Si alloy thin films in dilute hydrofluoric solution. *Metallurgical and Materials Transactions A* **23**, 2641-2655 (1992).

49 Blanc, C., Freulon, A., Lafont, M.-C., Kihn, Y. & Mankowski, G. Modelling the corrosion behaviour of Al2CuMg coarse particles in copper-rich aluminium alloys. *Corrosion Science* **48**, 3838-3851 (2006).

50 Augustin, C., Andrieu, E., Blanc, C., Mankowski, G. & Delfosse, J. Intergranular Corrosion of 2024 Alloy in Chloride Solutions. *Journal of The Electrochemical Society* **154**, C637-C644-C637-C644 (2007).

51 Lacroix, L., Ressier, L., Blanc, C. & Mankowski, G. Statistical Study of the Corrosion Behavior of Al2CuMg Intermetallics in AA2024-T351 by SKPFM. *Journal of The Electrochemical Society* **155**, C8-C15-C18-C15 (2008).

52 Lacroix, L., Ressier, L., Blanc, C. & Mankowski, G. Combination of AFM, SKPFM, and SIMS to Study the Corrosion Behavior of S-phase particles in AA2024-T351. *Journal of The Electrochemical Society* **155**, C131-C137-C131-C137 (2008).

53 Andreatta, F., Lohrengel, M. M., Terryn, H. & de Wit, J. H. W. Electrochemical characterisation of aluminium AA7075-T6 and solution heat treated AA7075 using a micro-capillary cell. *Electrochimica Acta* **48**, 3239-3247 (2003).

54 Andreatta, F., Terryn, H. & de Wit, J. H. W. Effect of solution heat treatment on galvanic coupling between intermetallics and matrix in AA7075-T6. *Corrosion Science* **45**, 1733-1746 (2003).

55 Andreatta, F., Terryn, H. & de Wit, J. H. W. Corrosion behaviour of different tempers of AA7075 aluminium alloy. *Electrochimica Acta* **49**, 2851-2862 (2004).

56 Schmutz, P. & Frankel, G. S. Corrosion Study of AA2024-T3 by Scanning Kelvin Probe Force Microscopy and In Situ Atomic Force Microscopy Scratching. *Journal of The Electrochemical Society* **145**, 2295-2306 (1998).

57 Davoodi, A., Pan, J., Leygraf, C. & Norgren, S. In Situ Investigation of Localized Corrosion of Aluminum Alloys in Chloride Solution Using Integrated EC-AFM/SECM Techniques. *Electrochemical and Solid-State Letters* **8**, B21-B24-B21-B24 (2005).

58 Burleigh, T. D., Ludwiczak, E. & Petri, R. A. Intergranular Corrosion of an Aluminum-Magnesium-Silicon-Copper Alloy. *Corrosion* **51**, 50-55 (1995).

59 Gao, M., Feng, C. & Wei, R. An analytical electron microscopy study of constituent particles in commercial 7075-T6 and 2024-T3 alloys. *Metallurgical and Materials Transactions A* **29**, 1145-1151 (1998).

60 Wei, R., Liao, C.-M. & Gao, M. A transmission electron microscopy study of constituent-particle-induced corrosion in 7075-T6 and 2024-T3 aluminum alloys. *Metallurgical and Materials Transactions A* **29**, 1153-1160 (1998).

61 Vukmirovic, M. B., Dimitrov, N. & Sieradzki, K. Dealloying and corrosion of Al alloy 2024-T3. *Journal of The Electrochemical Society* **149**, B428-B439, doi:Doi 10.1149/1.1498258 (2002).

62 Birbilis, N., Cavanaugh, M. K., Kovarik, L. & Buchheit, R. G. Nano-scale dissolution phenomena in Al–Cu–Mg alloys. *Electrochemistry Communications* **10**, 32-37 (2008).

63 Larsen, M. H., Walmsley, J. C., Lunder, O., Mathiesen, R. H. & Nisancioglu, K. Intergranular Corrosion of Copper-Containing AA6xxx AlMgSi Aluminum Alloys. *Journal of The Electrochemical Society* **155**, C550-C556-C550-C556 (2008).

64 Sun, D. M. *et al.* Ex situ TEM observation of localized attack on AA 6061. *Materials and Corrosion* **61**, 105-110 (2010).

Appendix A

Classification of Al Alloys

To identify the Al alloys, Table A.1, a four digit numerical designation system is adapted, the details of which are as follows:

i. The first digit indicates the alloy group.
ii. The last two digits identify the alloy or indicate Al purity.
iii. The second digit indicates the modifications of the original alloy or impurity limits.

Table A.1: Classification of Al Alloys

Major Alloying Element	Wrought Designation	Cast Designation
Aluminium (Al, min 99%)	1xxx	1xx.x
Copper (Cu)	2xxx	2xx.x
Silicon with added Cu or Magnesium	-	3xx.x
Silicon (Si)	4xxx	4xx.x
Manganese (Mn)	3xxx	-
Magnesium (Mg)	5xxx	5xx.x
Mg and Si	6xxx	-
Zinc (Zn)	7xxx	7xx.x
Tin (Sn)	-	8xx.x
Other element	8xxx	9xx.x
Unused series	9xxx	6xx.x
Zinc (Zn)	7xxx	7xx.x

The only difference between the designations of cast and wrought alloys is that the last digit, which indicates the product form (casting/ingot), is separated from the rest by a decimal point. Quite often the last digit after the decimal point is neglected and the cast alloys are indicated by just three digits. Based on the tempering process, a temper designation is given to these alloys. The temper designation follows the alloy designation after a hyphen, e.g. 2024-T3. The details of these designations are given in Table A.2.

Table A.2: Temper designation of Al Alloys

Designation	**Temper Description**
Basic temper designation	
F	As fabricated, no control over the amount of strain hardening, no mechanical property limits
O	Annealed and recrystallised. Temper with lowest strength and highest ductility
H	Strain hardened
T	Heat-treated to produce stable tempers
Strain-hardened subdivisions:	
H1	Strain hardened only. The degree of strain hardening is indicated by the second digit and varies from quarter hard (H12) to full Hard (H18) which is produced with approximately 75% reduction in area
H2	Strain hardened and partially annealed. Tempers ranging from quarter hard to full hard obtained by partial annealing of cold worked materials with strengths initially greater than desired. Tempers are H22, H24, H26 and H28.
H3	Strain hardened and stabilised. Tempers for age-softening Al-Mg alloys that are strain hardened and then heated at low temperature to increase ductility and stabilise the mechanical properties. H32, H34, H36 and H38.
Heat-Treated subdivisions:	
W	Solution Treated
T	Age Hardened
T1	Cooled from fabrication temperature and naturally aged
T2	Cooled from fabrication temperature, cold-worked and naturally aged
T3	Solution-treated, cold-worked and naturally aged
T4	Solution-treated, cold-worked and naturally aged
T5	Cooled from the fabrication temperature and artificially aged
T6	Solution-treated and artificially aged
T7	Solution-treated and stabilised by over-ageing
T8	Solution-treated, cold-worked and artificially aged
T9	Solution-treated, artificially aged and cold-worked
T10	Cooled from the fabrication temperature, cold-worked and artificially aged

Appendix B

Table B.1: Methods to evaluate localised corrosion in Al alloys

Type of Corrosion	**Methods of Evaluation**
Pitting Corrosion	Visual examination including low magnification photographs, measurement of depth, and assessment of size and number of pits (ASTM G 46). Determination of its effect on mechanical properties.
Intergranular Corrosion	Metallographic determination of extent and depth of attack (ASTM G 110). Determination of effect on mechanical properties.
Exfoliation Corrosion	Visual and metallographic examination, photographs, photomicrographs (ASTM G 34 and G 66).
Stress-Corrosion Cracking	Determination of minimum stress level required for failure, number of failures, time to failure (log-normal distribution), and probability of survival (or failure) versus time, crack propagation rate and threshold stress intensity.
Filiform Corrosion	Visual and metallographic examination. Photographs.
Staining	Visual examination and photographs. Measurement of reflectivity or image clarity.
Uniform Etching Corrosion	Rarely occurs, except in highly acidic or alkaline corrodents. Gravimetric methods (ASTM G 1).

Appendix C

Table C.1: Common surface analysis techniques used to evaluate corrosion products.[44]

Technique	Measured Particle	Process	Information	Surface Depth	Spatial Resolution
Auger electron spectroscopy (AES)	Auger electrons	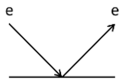	Elemental analysis Depth profiles Images	1-2 nm	>25 nm
Secondary ion mass spectrometry (SIMS)	Ions	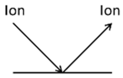	Elemental trace analysis Depth profiles Images	< 1 nm	>40 nm
X-ray photo-electron spectroscopy (XPS or ESCA)	Photo-electrons	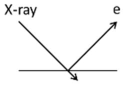	Elemental analysis Chemical bonding Depth profiles	1-2 nm	>50 µm
Reflection high energy electron diffraction (RHEED)	Electron (X-ray for X-ray emission (XRE))	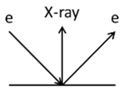	Surface structure	1-2 nm	>1 mm
Fe-conversion electron Mössbauer spectroscopy (CEMS)	Conversion and Auger electrons produced by y-rays	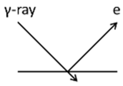	Fe-containing phase identification	1 nm - 0.5 µm	>1 mm
Transmission electron microscopy (TEM)	Electron (X-ray for e X-ray EDX)	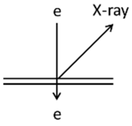	Morphology Crystal structure EELS	N/A	<1 nm

Chapter 2 METHODS

The experimental methods relevant to this study are described in this chapter. First a brief introduction to transmission electron microscopy (TEM) and relevant analytical techniques are described. Being a dedicated TEM study on aluminium alloys, the details on specimen preparation techniques for in situ as well as supporting ex situ and quasi in situ studies are given in the next section. Finally, in the last section of the chapter in situ experiments in TEMs have been introduced and our approach to carry out these studies is discussed.

1. Transmission Electron Microscopy[i]

Understanding of a material is complete only when we have the knowledge of the following aspects: processing, structure, properties and performance. The tools that enable us establish the links between these aspects are characterisation tools and one of the major characterisation tools that has played a significant role in understanding the structure and properties of materials down to the atomic scale, thereby opening the doors for synthesizing newer materials with exciting properties, is transmission electron microscopy (TEM).[1] Originally, the TEMs have been developed because of the limited image resolution in optical microscopes. It has been established that the resolution of an optical microscope is governed by the Rayleigh criterion, which states that the smallest resolvable distance, δ, is given approximately by the relation:[2]

$$\delta = \frac{0.61\lambda}{\mu \sin\beta} \qquad (1)$$

where, λ is the wavelength of the radiation, μ is the refractive index of the viewing medium, and β is the semi-angle of collection of the magnifying lens. As the resolution of an optical microscope is limited by the wavelength of the light, it has been decided to use an electron source to obtain images of higher resolution.[ii] In a TEM, a beam of highly energetic electrons is transmitted through a thin-specimen, interacting with the specimen as it passes through. The image formed by the transmitted beam is collected on a detector. The very first TEM developed by Max Knoll and Ernst Ruska in 1931, operated at an accelerating voltage of 50 kV and could achieve a modest magnification

---

[i] Most of the text in this section has been adapted from reference 1

[ii] the visible light has a wavelength between 380 – 750 nm whereas a 200 kV electron beam has a wavelength of approximately 0.0025 nm

of 17.4 ×.[3] From thereon, realizing the inverse relationship between the energy and the wavelength of the accelerated electron, microscopes with very high accelerating voltages (1 – 3 MeV) have been developed till the 1980s. However, owing to the disadvantages with the radiation damage at these high voltages plus the development of better lenses, the intermediate voltage (200 – 400 keV) TEMs became more popular from 1990 onwards. Recently with the development of aberration correctors, the information limit of the TEMs has improved to as good as 50 pm.[4] With such a powerful microscope, it is possible to look at the arrangement of atomic columns in most of the materials, known as high resolution TEM (HRTEM). There is another mode of operation where the electron is focussed to a probe and scanned over the specimen, known as scanning transmission electron microscopy (STEM), which expands the operational capabilities of a TEM. Apart from these techniques, low-voltage TEMs allow imaging materials showing knock-out damage and cryo-TEMs allow imaging biological specimens. The wide range of possibilities to quantitatively characterise a specimen, make the TEM a superior characterisation tool and a diverse as well as a very important field of study. For the sake of understanding, the construction of a TEM can be considered analogous to an optical microscope.[5]

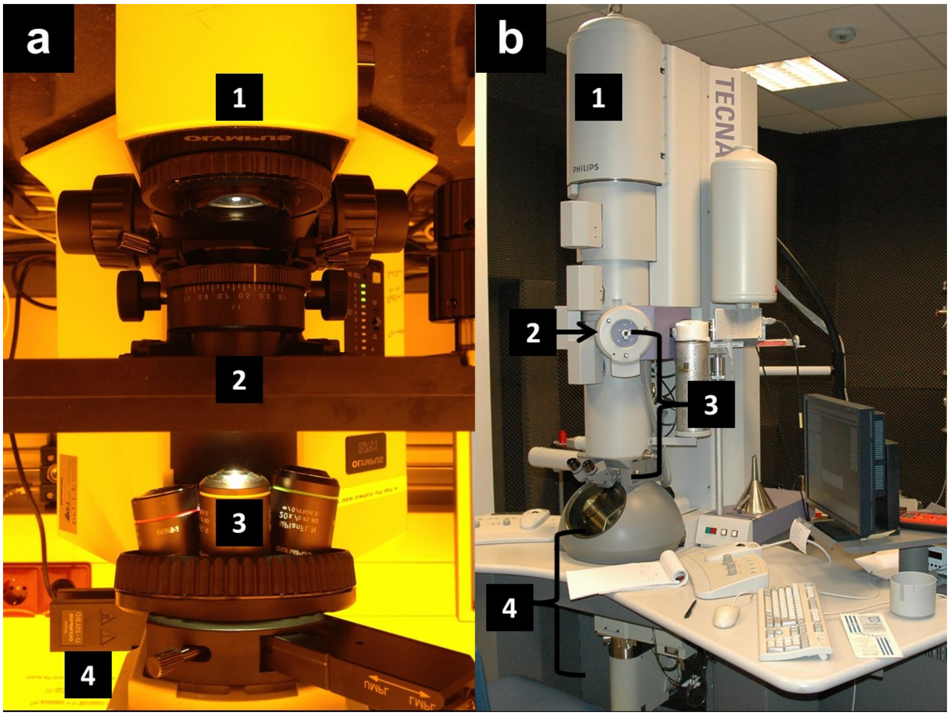

Figure 2.1: Photographs showing the similarities in the construction of (a) optical microscope and (b) a transmission electron microscope. The parts labelled correspond to 1) illumination system: visible light and electrons, 2) Specimen area: table and compustage/goniometer, 3) Lenses: glass and electromagnetic, 4) Output: Eyepiece / CCD camera and Fluorescent screen / CCD camera respectively for optical microscope and TEM.

In principle, the components of the TEM are similar to that of an optical microscope with illumination from the bottom for transparent specimens, Figure 2.1, when visualised upside down. Both these instruments have an illumination system, visible light in case of optical microscope and electron gun in case of a TEM. The probing signal then transmits through the specimen, while the external atmosphere has no influence on the optical microscope, TEM is under ultra-high vacuum such that the electrons are unaffected by scattering due to the surrounding atmosphere. The signal transmitted through the specimen goes through the lens system towards the detector where the information from the specimen is visualised. In an optical microscope, there are glass lenses, objective and an eyepiece so as to reconstruct a magnified image whereas in a TEM the transmitted electrons go through the objective-intermediate and projector lenses to form an image on the detector as shown in Figure 2.2.[5]

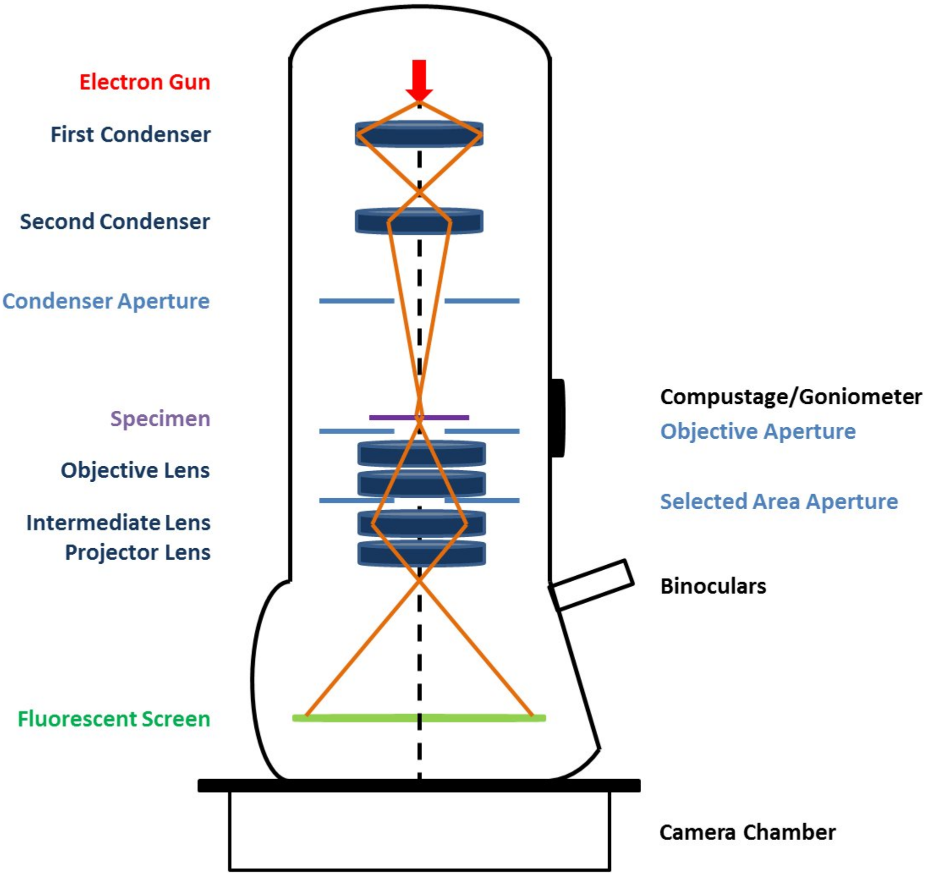

Figure 2.2: Ray diagram of a typical TEM, The electrons are accelerated through the column under a high-voltage and with the help of a series of electromagnetic lenses, an image is formed on the detector.

In a TEM, the most important phenomenon is the interaction between the electrons and the specimen. When a beam of electrons interacts with the specimen, incoming electrons are scattered by the specimen and in the process, several signals are generated as shown in Figure 2.3. A large fraction of the electrons are elastically scattered, i.e. there is a deviation in the transmitted electrons due to the specimen without any loss of energy while the remaining electrons that lose energy undergo inelastic scattering, resulting in several other signals like X-rays and inelastically scattered electrons. In a conventional TEM, we utilise the transmitted electrons or the forward scattered electrons for most of the study. The conventional TEM techniques are imaging and diffraction. In imaging, the mechanisms for contrast in TEM images would be discussed shortly while in diffraction, the electron beams that satisfy the Bragg's law in a crystalline specimen are diffracted at specific angles forming a periodic diffraction pattern. By a combination of these imaging and diffraction techniques, it is possible to do a complete crystal structural analysis of specimens in a TEM.[2]

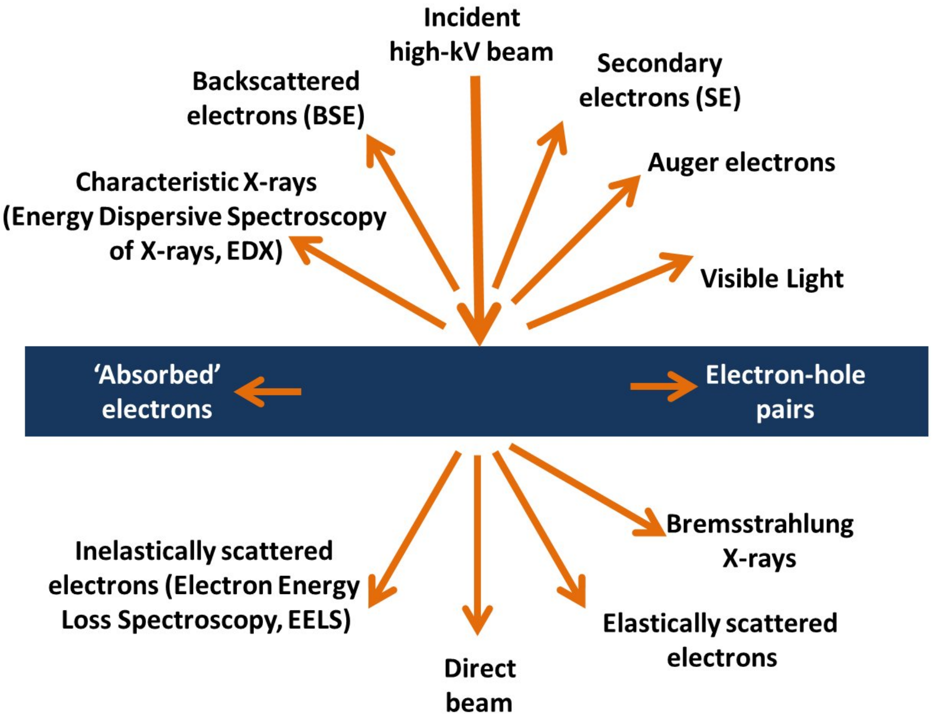

Figure 2.3: Signals generated when a high-energy beam of electrons interacts with a thin specimen. Most of these signals can be detected in different types of TEM. The directions shown for each signal do not always represent the physical direction of the signal. The techniques EDX and EELS have been used to analyse the composition as well as the electronic structure of the specimens in this study.

1.1. Imaging in (S)TEM

The imaging in a TEM is realised by one of the following methods: static beam and scanning beam. Static beam imaging is straightforward; all the forward scattered electrons are collected on the detector. Scanning in TEM is achieved by incorporating electromagnetic beam deflection coils in the illumination system, as shown in Figure 2.4. The electron beam is converged by the condenser lens to a spot called ‘probe’ (typical probe sizes range from 0.05 to 0.2 nm). The probe is scanned over the specimen and the forward scattered electrons are collected using an annular detector to form an image.[5]

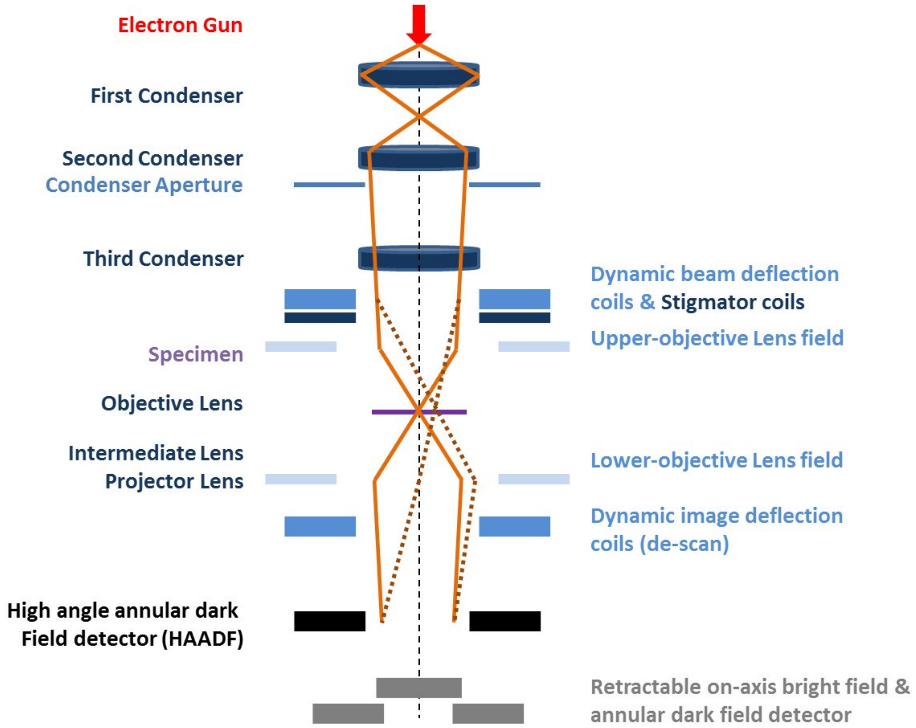

Figure 2.4: Ray diagram for STEM mode in a 3 condenser-lens TEM. Most of the modern TEMs have the third condenser coupled with the objective lens, also known as the condenser-objective lens system. The relevant on-axis and off-axis detectors for different imaging modes are also shown here.

The contrast of images in a (S)TEM can broadly be classified as either amplitude contrast or phase contrast and most of the images in TEM are obtained by a combination of both of these contrasts. The amplitude contrast has two principal types, diffraction contrast (TEM, STEM) and mass-thickness contrast (TEM, STEM). Z-contrast is another term that arises while looking at high-resolution STEM images, where detectable scattering arises from single atoms or column of atoms.[6]

Any difference in the specimen like: the presence of precipitates, defects like dislocations, grain boundaries or orientation differences between the electron beam and specimen due to tilting; lead to a change in diffraction conditions which gives rise to diffraction contrast. Any microstructural variations causing a change in diffraction contrast can be imaged by using a suitable objective aperture. For instance, the contrast of an image can by enhanced by just selecting the direct beam, also called bright-field (BF) imaging; or by suitably selecting a diffraction spot, the features corresponding to that particular spot can be highlighted, called dark-field (DF) imaging.[5]

Each element has its own scattering power and heavy atoms have a stronger interaction with electrons than lighter atoms. If the specimen thickness is homogeneous, variations in the atomic mass of the constituent elements results in the mass and atomic number contrast. On the other hand, if there is a variation in the thickness of the specimen, the electrons are scattered more in thicker areas than in thinner areas resulting in a thickness contrast. Phase contrast arises from the interference of the primary beam and the diffracted beams. Phase contrast is responsible for the appearance of lattice fringes in TEM images.[7] When a crystalline sample is oriented along one of the low-index zone axes, in microscopes equipped with field emission guns (FEGs), the images obtained at high magnifications show contrast variations perceived as discrete peaks. The diffracted beams from the parallel planes of crystalline specimen can be imaged at the back focal plane of the objective lens as spots, which recombine in the image plane and are then magnified by the projector lenses resulting in an image with periodic lattice fringes. These images are referred to as lattice images and under certain conditions these peaks correspond to the atom columns. The phase relationship between the electrons leaving the specimen is responsible for the contrast obtained in these images and it severely depends on the thickness of the specimen. This technique of obtaining atomic-resolution images is called high-resolution transmission electron microscopy (HRTEM).

While imaging in STEM mode, using the high angle annular dark field (HAADF) detector, it is possible to visualise the lattice with Z-contrast (atomic number contrast). It is understood that the images collected from beams elastically scattered at higher angles (50 – 150 mrad) show a dependency on the atomic number approximately as $Z^{1.7}$. In these images, there is no coherency between the high angle scattered beams which are collected on an annular detector. Therefore in a high resolution STEM (HRSTEM) image obtained with a HAADF detector, the intensities from individual scattering centres (atoms) along the beam path can be added enabling a direct interpretation of atom types and positions. Combining all these imaging techniques, it is possible to get complete morphological and structural information of a specimen at the atomic scale.

1.2. Microanalysis in (S)TEM

One of the primary advantages of TEM investigations is not just the high resolution imaging (50 pm in a probe corrected microscope), but also the combination of these imaging techniques with the other generated signals to analyse the chemistry of the specimens. A microscope capable to do this kind of study is called analytical transmission electron microscope (ATEM) and the study is called microanalysis. Most of the modern TEMs operating at intermediate voltages of 200/300 kV are equipped to carry out (scanning) transmission electron microscopy ((S)TEM) along with energy dispersive X-ray spectroscopy (EDX) as well as the complementary techniques of electron energy loss spectroscopy (EELS) and energy filtered transmission electron microscopy (EFTEM).[2,8]

1.2.1. EDX analysis

When the accelerating electrons ionise an atom in the TEM specimen, each of the possible transitions within the internal shells of the atom is associated with the emission of a characteristic X-ray, which has energy unique to that element. The emitted X-ray photons are collected using special detectors and plots of X-ray counts versus X-ray energy are generated. From the intensities of the peaks corresponding to specific elements, it is possible to quantify and estimate the elemental composition of a specimen. Conventional X-ray detectors are semiconductor based, lithium (Li) doped silicon (Si), protected by an ultrathin window cooled to liquid nitrogen (N_2) temperature to prevent the thermal noise during the collection.[9] In this study, apart from the EDX analysis using the conventional detectors, we have also carried out studies using the new 'Super-X' detector which allows obtaining 512 × 512 pixel maps in nearly 5 minutes. This is possible because four windowless Si drift detectors (SDD) are arranged symmetrically around the specimen area in the TEM column as shown in Figure 2.5.[10]

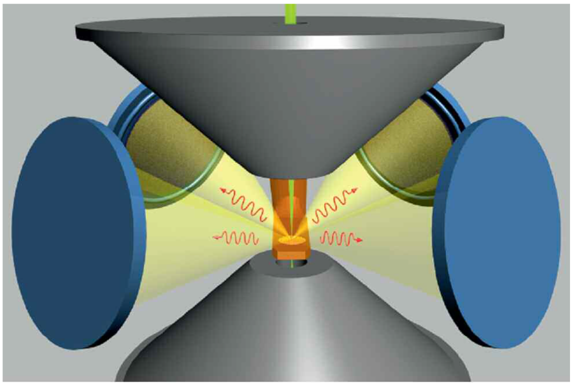

Figure 2.5: Diagram showing the positioning of the four windowless Si drift detectors around the pole piece of the objective lens in a TEM.[10] This way the signal from the specimen collection is improved significantly allowing genuinely quick EDX maps

The main difference between the SDD and traditional semiconductor Si(Li) detector arises due to the arrangement of electrodes in the detector. In the traditional Si(Li) detector, we have a Si wafer with a thin Li-doped layer (p-type) protected by a window exposed to the X-rays while the back side of the of detector(n-type) acts as the anode. When X-rays impinge the Si(Li) layer, electron-hole pairs are generated and are separated by the bias on the wafer which is read out as a signal. The SDD on the other hand has high purity Si on the entrance side, with a central small anode surrounded by concentric metallic electrodes on the opposite side. The Si substrate (n-type) is fully depleted by applying a negative bias with respect to the anode and the ring electrodes apply a field gradient on the back side. This way the electrons produced by ionisation due to an incoming X-ray spontaneously drift towards the anode which is read out instantaneously.[9,11] Once the intensity-energy plots for the X-rays are generated after detection, the amounts of elements present in the specimen are estimated from the relation between the weight fraction and generated intensities (ionisation cross-section), which is given by the Cliff-Lorimer equation:[12]

$$\frac{W_A}{W_B} = k_{AB}\frac{I_A}{I_B} \qquad (2)$$

Where W_A, W_B, I_A, I_B are the weight fractions and the intensities of the elements *A* & *B*; K_{AB} is a sensitivity factor known as the Cliff-Lorimer factor. The Cliff-Lorimer factor can be determined experimentally from a specimen of known composition or from a single phase compound and this value is instrument specific. There are several factors to be considered while estimating the composition from EDX analysis, like the effects of fluorescence and absorption. The equation (2) is valid when the fluorescence and the absorption effects are negligible. In case of the TEM specimens, being quite thin the absorption effects are usually quite negligible, and hence the Cliff-Lorimer method gives a reasonable compositional estimate.

1.2.2. EELS & EFTEM

By collecting the inelastically scattered electrons, i.e. the electrons that have lost some energy after interacting with the specimen, it is possible to gain valuable insights into the characteristics of a specimen.[8] Electron energy loss spectroscopy (EELS) and energy filtered TEM (EFTEM), are two techniques which utilise the inelastic scattering for analysis.[8,13] The energy loss events on one hand degrade the image quality as the electrons that have lost energy, focus differently from those that haven't lost any energy resulting in blurring; on the other hand give valuable information on the electronic structure of the specimen atoms like bonding, valence state, dielectric response, free electron density as well as band gap. The information obtained from forward scattered electrons in a TEM image can be visualised as the diagram shown in Figure 2.6. This information can be retrieved by a process called energy filtering.[13-16]

During energy filtering, the forward scattered inelastic electrons are separated according to their energies through a magnetic prism. The electrons are then separated according to their energies to an energy spectrum. By varying the settings of magnetic prism and a slit, these separated electrons can be restored to form an image through a lens.

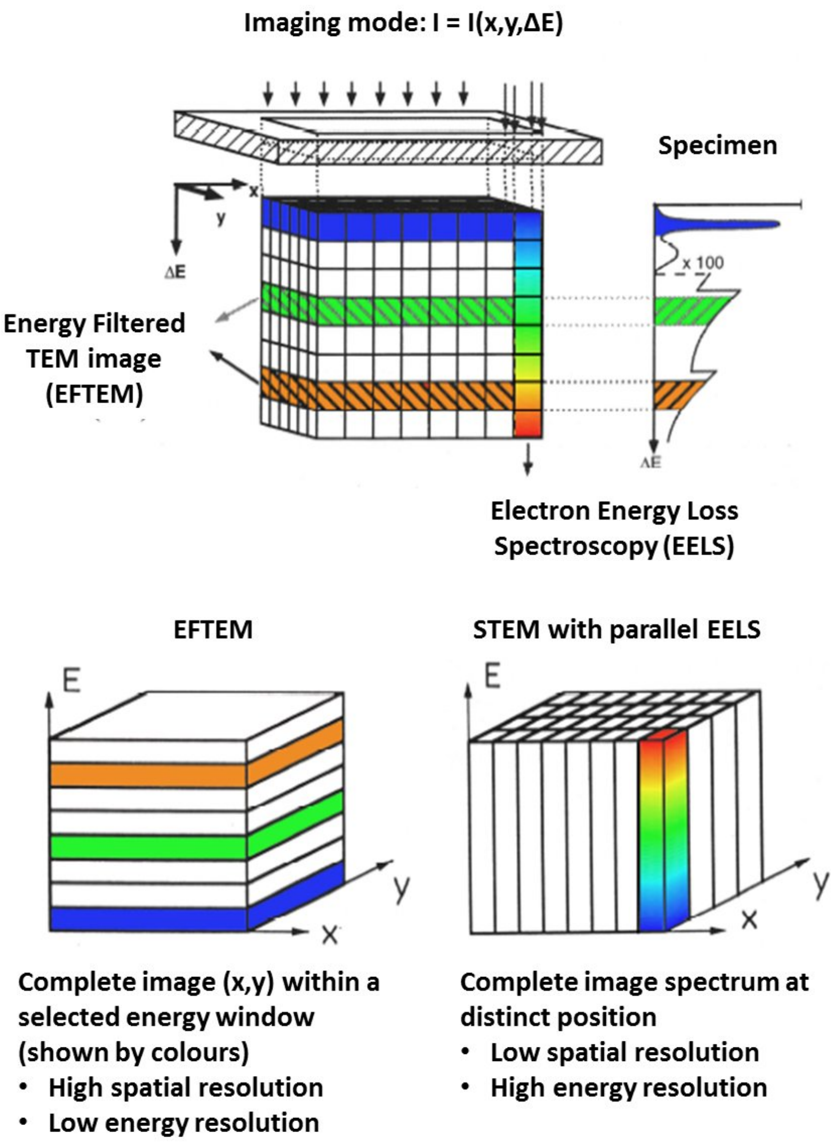

Figure 2.6: Information obtained from forward scattered electrons in a TEM.[16] *In EELS, the electrons are separated according to their energies and displayed as a spectrum, whereas in EFTEM a 2-dimensional map from an area within an energy range is displayed as an image. While imaging in scanning mode, it is possible to correlate each pixel of an image to its energy spectra, in which case it is called parallel EELS (PEELS).*

When the energy spectrum is displayed, it is called EELS whereas the image displayed within an energy range is EFTEM image. For understanding the key features observed from EEL-spectra, example spectra are shown in Figure 2.7.

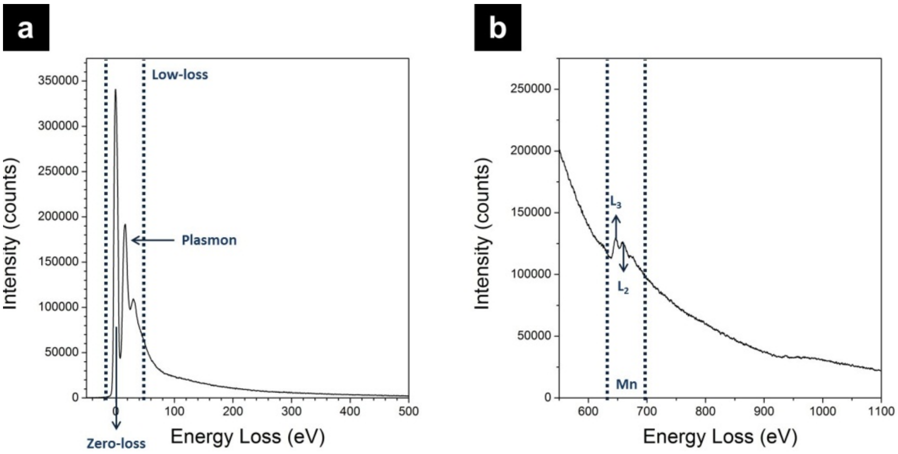

Figure 2.7: Example EEL-spectra from an AA2024-T3 specimen showing (a) low-loss spectra and (b) Mn $L_{2,3}$ ionisation edge at 640 eV.

EEL-spectra can broadly be classified based on the energy as: low-loss & no-loss regions, and characteristic ionisation edges. The low-loss & no-loss region consists of the zero-loss peak, i.e. the electrons that have elastically scattered and a large fraction of forward scattered electrons and the electrons that have lost energy of ~ 50 eV. The low-loss region has arbitrarily been fixed at ~ 50 eV and within this regime the information pertaining to dielectric response, the plasmon peaks, information related to band gap and specimen thickness can be obtained. When sufficient energy from the electron beam is transferred to one of the core-shell electrons of the atoms of the specimen, to move it outside the attractive field of the nucleus, ionisation happens and this is reflected as an ionisation edge in EEL-spectrum. Similar to characteristic X-rays, every element has energy associated the ionisation edges. Typically about 5 % of the forward scattered electrons are inelastically scattered and an inelastic scattering event causes atom to deviate the scattered beam at larger angles (typically around 5 - 10 mrad) also resulting in a low intensity. From the region ~ 50 eV next to the ionisation edge, the information about the chemical bonding can be retrieved and this technique is called energy-loss near-edge structure (ELNES). In principle, it is possible to quantitatively characterise all these features when the convergence and the collection angles of the electron beam are known. By selecting a suitable energy window around an ionisation edge, it is possible to collect the 2-dimensional energy distribution maps from an area in a specimen, known as EFTEM imaging. It is possible to obtain these maps while operating the TEM either in a static beam condition or by scanning a beam over the specimen. During the scan, EEL-spectra can be obtained at each pixel of the image. Both these approaches have advantages and disadvantages. The energy resolution in EFTEM is mainly limited by the non-isochromaticity, i.e. the differences in the energy between two locations in an EFTEM image arising due to the filter optics. In EELS, the energy resolution is limited by the energy resolution of source, for most of the commercial instruments operating with a FEG have an energy resolution of ~ 0.8 eV and this can be improved to as good as 20 – 30 meV[17] by using a monochromated source. While mapping PEEL-spectra in STEM mode, the lateral resolution in an image is limited by STEM probe size. Practically, the time required for recording a spectra can vary depending on the energy regime of interest and this could vary anywhere between 0.1 to 100 s.[14-16,18,19] Due to the longer recording times, a few other factors like sample drift, energy drift can cause an image distortion and a loss of resolution. In the present study, we have used EELS and EFTEM to study the localised corrosion in a commercial aluminium (Al) alloy, AA2024-T3.

2. Specimen preparation techniques

A successful TEM experiment depends largely on the quality of the specimen being investigated. As we need the electrons to transmit through the specimen, the specimen has to be as thin as possible. The ideal specimen thickness depends on several factors like the imaging technique being used, the atomic weight of the specimen. In general, the accepted thicknesses for TEM investigation are ≤ 100 nm.[2,20] For HRTEM studies, the specimen thicknesses should be even less than 50 nm. Also for EELS studies, the thinner the specimen the better it is. The material used for the present study is AA2024-T3, and being a relatively light element, thicknesses around 100 nm are acceptable for Al.[21] An important factor that has to be considered while investigating the TEM specimens is the influence of surfaces. As the TEM specimens are nearly 2-dimensional in nature having very large surface area to volume ratio lacking the constraints of the surrounding material found in bulk samples, one has to be very careful while interpreting the observations from a TEM specimen.

The specimens for this study have been prepared using three techniques, electropolishing, ion-milling and focused ion beam (FIB), which are described here very briefly. The as-received specimens are strips of dimensions $10 \times 10 \times 0.08$ cm^3. The first step before electropolishing and ion-milling, involves mechanical polishing. In this step, smaller squares of ~ 2×2 cm^2 are cut and are polished through a series of silicon carbide (SiC) abrasive papers to a thickness of ~100 µm for electropolishing and ~20 µm for ion milling. Discs of 3 mm diameter are then punched out and are subsequently electropolished or ion milled. The details of the specimen preparation relevant to the specific studies are described in the forthcoming chapters once again; therefore the principle involved in these techniques is described here. Figure 2.8 shows the different stages of electropolishing and ion milling.

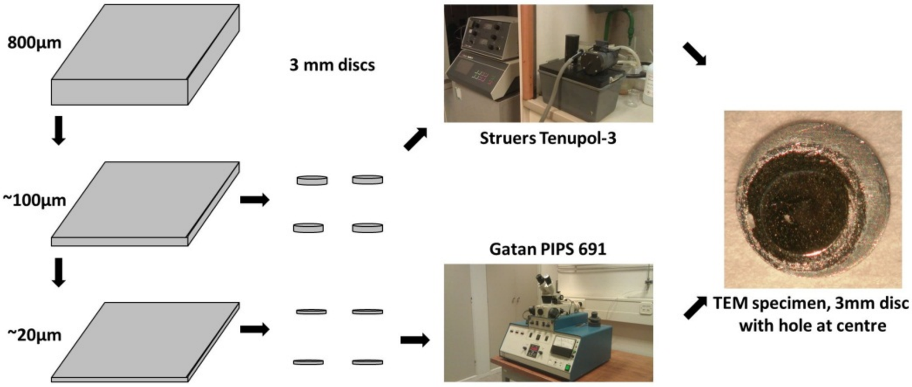

Figure 2.8: Sequence of operation for preparing specimens by electropolishing and ion milling: First the as-received specimen is mechanically polished to thicknesses of ~100 µm and ~20 µm and then electropolished and ion milled using the apparatus shown here.

2.1. Electropolishing

The idea involved in electropolishing is very closely related to the corrosion of a material. The specimen to be thinned down after mechanical grinding is connected as anode in an electrochemical cell and two jets of electrolyte are directed towards the specimen from either side. In this study, we used a Struers Tenupol-3 apparatus. Usually a high potential (15 - 30 V) is applied for most of the metallic specimens to achieve currents of around 0.5 – 1 A. Within a few seconds of polishing, usually 20 - 30 s, a hole is formed in the specimen. Due to the electrolyte jets from either side, the region surrounding the hole has nearly a wedge shape with thicknesses < 50 nm making these regions good for TEM investigation. In this method of preparing TEM specimens, operating at high voltages causes an aggressive dissolution of the Al matrix as well as the precipitates, leaving no particular signatures of localised attack around the intermetallic precipitates, however occasionally a few precipitates are removed completely leaving holes in the specimen and in a very few cases cracks along grain boundaries.

2.2. Ion-milling

In ion milling, the 3 mm discs of ~ 20 µm thicknesses are further thinned down by bombarding with a beam of argon (Ar) ions with low energies of 2 – 5 kV. To have an electron transparent area as large as possible, the Ar ions are directed at a low incidence angle of 5 - 10°. For this, we have used the Gatan precision ion polishing system (PIPS). Normally it takes about 45 min to 1 hr to obtain specimens good enough for TEM investigation.

There are several advantages and disadvantages using both these techniques of electropolishing and ion milling. The main advantage is that these are a relatively straightforward processes and it is easy to produce several specimens reasonably quickly once the 3 mm discs are punched and ready. Close to the hole formed at the centre, the specimen is usually very thin, < 50 nm and the thickness increases as we move outwards (wedge shaped). The drawbacks of these methods are no control over the exact location where the specimen has to be thinned down; however, the specimens are large enough that areas of interest can always be found. Furthermore, the milling artefacts have to be considered and should not be misinterpreted as a microstructural feature from the specimen.

2.3. Focused Ion Beam

A focused ion beam (FIB) is an instrument that looks like a scanning electron microscope and is built upon similar principles and pretty much operates like an SEM except that ions are accelerated in a FIB for imaging and specimen modification. In fact the modern day FIBs are integrated with an SEM and the instrument is called a dual beam (SEM-FIB), Figure 2.9. While the electron beam allows conventional SEM imaging, the ion beam is used to modify the sample surface by milling. Common FIBs run on gallium (Ga) ion source as it is liquid close to room temperature and can be focused to a very fine probe. The typical operating voltages for FIB range between 5 – 30 kV. By controlling the strength of the electrostatic lenses and adjusting the aperture sizes, the probe current density can be altered from few tens of pA to nA corresponding to beam diameters of ~ 5 nm to 0.5 µm.[22-24]

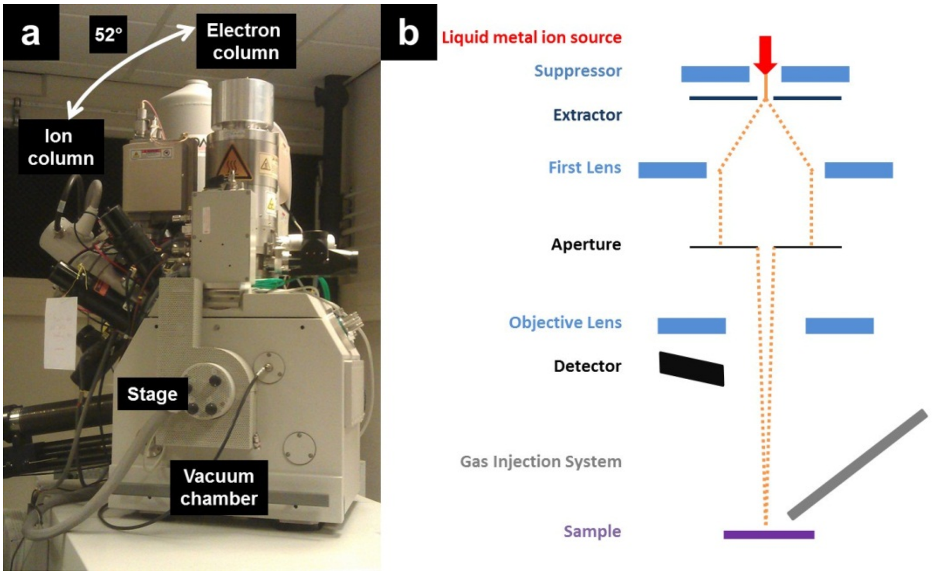

Figure 2.9: (a) Photograph showing a dual-beam (FIB-SEM) and (b) A simplified ray diagram of the FIB column showing the impingement of Ga ion beam (orange dotted line) on the specimen surface of a specimen

The principle involved in a FIB is that the heavy Ga ions accelerated towards the sample sputter the surface and cause a modification. Typically the penetration depth is ~ 25 nm for ~ 25 keV Ga ions. By using scripts to control the path of the ion beam, it is possible to precisely define the shapes and sizes of interest and modify the samples accordingly. Using this method, it is possible to produce TEM specimens of sizes ~ 15 µm × 5 µm × 100 nm. The primary advantage of this method is that specimens localised to very specific areas of interest, like cross-section samples across an interface, specimens from a special phase can be precisely prepared. Prior specimen preparation similar to that of SEM investigation, i.e. having a highly polished surface is necessary. There are a few drawbacks related to the implantation of Ga ions in the TEM specimen.[25] As long as the Ga ion implantation doesn't affect the TEM investigation, this is a very reliable method to prepare specimens. In principle, in the modern FIB instruments, by using *in situ* micromanipulator to lift out a TEM specimen and milling the surface at a grazing incidence at low accelerating voltages (1 kV), it is possible to produce very high quality specimens as thin as 10 – 20 nm with negligible surface damage.[22-26]

3. In-situ TEM experiments

TEM is well known as a powerful characterisation tool capable of carrying out structural and compositional analysis down to the atomic level. Over the years, these techniques have given valuable understanding of several materials and phenomenon. On one hand applying TEM techniques to solve structural and compositional problems for newer materials has been an interesting challenge, improving the resolution of a TEM has been driving the research and development in this area till last decade. With the invention of advanced image (C_S) correctors and probe correctors, the modern microscopes have overcome the barrier of 1 Å resolution. The best achievable resolution of a probe corrected microscope is as good as 50 pm. This is quite good to resolve the structure of almost all of the inorganic materials.

While developing and improving the resolution of low-voltage TEMs for soft materials (biological and beam sensitive mono/few-layered structures like graphene) is one of the areas where there is substantial research interest, dynamic experimentation in TEMs is an area where there is an ever increasing interest. To be able to visualise various physical phenomena *in situ* in a TEM, preferably at atomic resolution gives a much better understanding at the fundamental level. These could be induced either by heating, mechanical deformation, applying an electrical bias, or studying chemical reactions by creating a reactive environment inside the TEM.[27-34] Interest in *in situ* experiments has been considerable since the early 1960s and the earliest experiments have been heating specimens inside the TEM. The other areas like mechanical deformation and chemical reactions in the TEM picked up rather quickly.

The heating experiments traditionally have been carried out by incorporating a heating element (either metallic or ceramic) encircling the specimen area of a TEM holder. While this method has been successful in carrying out dynamic experiments in the TEM, the achievable resolution has been quite poor due to the poor drift stability of the holder while heating. This is partly due to the high power used for heating the coil as well as the thermal expansion and poor heat dissipation. There have also been attempts to integrate a laser beam into the column of the TEM to heat specimens.

The environmental TEM studies, i.e. the studies involving gas/liquid-specimen interaction in the TEM have been approached by two methods. One of the methods is to modify the specimen area of the TEM to introduce differential pumping apertures to allow reactive gases around the specimen while the other approach has been the utilisation of a windowed environmental cell. The earliest attempts to carry out chemical reactions in a windowed cell from the period of 1962 – 1977 have all been on top-entry high voltage TEMs with windows made of carbon/nitrocellulose/silicon monoxide/silicon carbide encapsulating a heating grid with a maximum achievable pressure of 1 bar. The aperture cells (using differential pumping aperture) also during the same period have been in top-entry microscopes and out of all these cases the maximum achievable pressure has been in the order of 50 mbar with a few exceptions of 1 bar where thick differential apertures of 200 µm above and 400 µm below the specimen have been used in a side-entry microscope.

In most of these cases the resolution has not been stated and the best reported resolution has been 2 nm at 1 bar pressure of air in a microscope operated at 1 MeV.[35] Gradually the high-voltage top-entry microscopes have phased out and the intermediate voltage microscopes became more popular. Most of the modern TEMs now operate at intermediate voltages of 200-300 kV, with improved lenses providing a larger pole-piece gap opening wider opportunities for *in situ* experiments. The commercial environmental TEMs are based on the differential pumping aperture approach and can achieve a maximum environmental pressure of ~ 10 mbar. This limitation on the pressure of the environment can be tackled by adapting the windowed cell approach.

With the advancements in microelectromechanical systems (MEMS) based technologies, the areas of *in situ* heating and environmental TEM have grown rapidly over the last decade. By using MEMS based heaters, it has been shown that the specimen drift during heating experiments can be minimised to ~0.1 nm/min, due to localised heating and low power dissipation. Likewise in case of the MEMS based environmental cells, made from a Si wafer with a silicon nitride (Si_XN_Y) membrane, pressures as high as 4.5 bar have been achieved and atomic resolution at 1 bar pressure has been possible.[36-41] All these advancements make the area of *in situ* transmission electron microscopy an exciting field of study.

4. Current approach

Our interest is to develop a methodology to investigate the microstructural evolution of metallic alloys the influence of these microstructural features on the corrosion properties of these alloys *in situ* in a TEM. For this, we have selected the well-known commercial alloy, AA2024-T3 and carried out *in situ* heating as well as corrosion experiments. We have used the MEMS based heating systems and environmental cells developed in-house to carry out these studies. From the *in situ* heating experiments, we are interested in gaining insights in to the morphological changes and microstructural evolution (chapter 3), as the mechanical properties as well as corrosion resistance of aluminium alloys depend significantly on their microstructure.

In case of the *in situ* corrosion studies, we are interested in the influence of the second phase intermetallic particles on the localised corrosion of aluminium alloys. The *in situ* corrosion experiments have been approached as follows: first we carried out *ex situ* (chapter 4) and quasi *in situ* corrosion studies (chapter 5) to decide the suitable experimental window to carry out *in situ* corrosion studies. After optimizing these parameters, *in situ* corrosion experiments have been carried out (chapter 6). Finally, as an attempt to understand the corrosion protection mechanism of cerium based inhibitor for aluminium alloys, we have carried out some preliminary quasi *in situ* inhibition studies (chapter 7). All the relevant experimental details pertaining to the holders used for the quasi *in situ* and *in situ* studies have been described at their respective chapters.

References

1 Williams, D. B. & Carter, C. B. *Transmission Electron Microscopy*. 2 edn, (Springer, 2009).

2 Williams, D. B. & Carter, C. B. in *Transmission Electron Microscopy* Vol. 1 Ch. 1, 3-22 (Springer, 2009).

3 Ruska, E. The development of the electron microscope and of electron microscopy. *Reviews of Modern Physics* **59**, 627-638, doi:10.1103/RevModPhys.59.627 (1987).

4 Kisielowski, C. *et al.* Detection of Single Atoms and Buried Defects in Three Dimensions by Aberration-Corrected Electron Microscope with 0.5-Å Information Limit. *Microscopy and Microanalysis* **14**, 469-477, doi:10.1017/s1431927608080902 (2008).

5 Williams, D. B. & Carter, C. B. in *Transmission Electron Microscopy* Vol. 1 Ch. 9, 141-172 (Springer, 2009).

6 Williams, D. B. & Carter, C. B. in *Transmission Electron Microscopy* Vol. 3 Ch. 22, 371-388 (Springer, 2009).

7 Williams, D. B. & Carter, C. B. in *Transmission Electron Microscopy* Vol. 3 Ch. 23, 389-406 (Springer, 2009).

8 Williams, D. B. & Carter, C. B. in *Transmission Electron Microscopy* Vol. 1 Ch. 4, 53-72 (Springer, 2009).

9 Williams, D. B. & Carter, C. B. in *Transmission Electron Microscopy* Vol. 4 Ch. 32, 581-604 (Springer, 2009).

10 Schlossmacher, P., Klenov, D. O., Freitag, B. & von Harrach, H. S. Enhanced Detection Sensitivity with a New Windowless XEDS System for AEM Based on Silicon Drift Detector Technology. *Microscopy Today* **18**, 14-20 (2010).

11 Lechner, P. *et al.* Silicon drift detectors for high resolution room temperature X-ray spectroscopy. *Nuclear Instruments and Methods in Physics Research Section A: Accelerators, Spectrometers, Detectors and Associated Equipment* **377**, 346-351, doi:10.1016/0168-9002(96)00210-0 (1996).

12 Williams, D. B. & Carter, C. B. in *Transmission Electron Microscopy* Vol. 4 Ch. 35, 639-662 (Springer, 2009).

13 Egerton, R. F. *Electron energy-loss spectroscopy in the electron microscope*. (2011).

14 Williams, D. B. & Carter, C. B. in *Transmission Electron Microscopy* Vol. 4 Ch. 37, 679-698 (Springer, 2009).

15 Keast, V. J., Scott, A. J., Brydson, R., Williams, D. B. & Bruley, J. Electron energy-loss near-edge structure – a tool for the investigation of electronic structure on the nanometre scale. *Journal of Microscopy* **203**, 135-175 (2001).

16 Foord, D., Freitag, B., Kübel, C. & Tang, D. in *Tecnai Advanced Materials Science* 7.1 - 7.21 (FEI Electron Optics B.V., 2002).

17 Krivanek, O. L., Lovejoy, T. C., Dellby, N. & Carpenter, R. W. Monochromated STEM with a 30 meV-wide, atom-sized electron probe. *Microscopy*, doi:10.1093/jmicro/dfs089 (2013).

18 Egerton, R. F., Crozier, P. A. & Rice, P. Electron energy-loss spectroscopy and chemical change. *Ultramicroscopy* **23**, 305-312, doi:10.1016/0304-3991(87)90240-3 (1987).

19 Egerton, R. F. Limits to the spatial, energy and momentum resolution of electron energy-loss spectroscopy. *Ultramicroscopy* **107**, 575-586, doi:10.1016/j.ultramic.2006.11.005 (2007).

20 Williams, D. B. & Carter, C. B. in *Transmission Electron Microscopy* Vol. 1 Ch. 10, 173-193 (Springer, 2009).

21 Egerton, R. F. in *Electron Energy-Loss Spectroscopy in the Electron Microscope* (Springer, 2011).

22 Phaneuf, M. W. Applications of focused ion beam microscopy to materials science specimens. *Micron* **30**, 277-288, doi:10.1016/s0968-4328(99)00012-8 (1999).

23 Giannuzzi, L. A. & Stevie, F. A. A review of focused ion beam milling techniques for TEM specimen preparation. *Micron* **30**, 197-204, doi:10.1016/s0968-4328(99)00005-0 (1999).

24 Li, J., Malis, T. & Dionne, S. Recent advances in FIB-TEM specimen preparation techniques. *Materials Characterization* **57**, 64-70, doi:10.1016/j.matchar.2005.12.007 (2006).

25 Lehrer, C. *et al.* in *Ion Implantation Technology, 2000. Conference on.* 695-698.

26 Ko, D.-S., Park, Y. M., Kim, S.-D. & Kim, Y.-W. Effective removal of Ga residue from focused ion beam using a plasma cleaner. *Ultramicroscopy* **107**, 368-373, doi:10.1016/j.ultramic.2006.09.004.

27 Cumings, J., Olsson, E., Petford-Long, A. K. & Zhu, Y. Electric and Magnetic Phenomena Studied by In Situ Transmission Electron Microscopy. *MRS Bulletin* **33**, 101-106 (2008).

28 Ferreira, P. J., Mitsuishi, K. & Stach, E. A. In Situ Transmission Electron Microscopy. *MRS Bulletin* **33**, 83-90 (2008).

29 Gai, P. L., Sharma, R. & Ross, F. M. Environmental (S)TEM Studies of Gas?Liquid?Solid Interactions under Reaction Conditions. *MRS Bulletin* **33**, 107-114 (2008).

30 Howe, J. M., Mori, H. & Wang, Z. L. In Situ High-Resolution Transmission Electron Microscopy in the Study of Nanomaterials and Properties. *MRS Bulletin* **33**, 115-121 (2008).

31 Robertson, I. M., Ferreira, P. J., Dehm, G., Hull, R. & Stach, E. A. Visualizing the Behavior of Dislocations?Seeing is Believing. *MRS Bulletin* **33**, 122-131 (2008).

32 Saka, H., Kamino, T., Ara, S. & Sasaki, K. In Situ Heating Transmission Electron Microscopy. *MRS Bulletin* **33**, 93-100 (2008).

33 Gai, P. L., Sharma, R. & Ross, F. M. Environmental (S)TEM Studies of Gas–Liquid–Solid Interactions under Reaction Conditions. *MRS Bulletin* **33**, 107-114, doi:10.1557/mrs2008.23 (2008).

34 Butler, E. P. & Hale, K. F. in *Practical Methods in Electron Microscopy - Dynamic Experiments in the Electron Microscope* Vol. 9 (ed M. Glauert) Ch. 1, 1-34 (Elsevier Science Ltd 1981).

35 Butler, E. P. & Hale, K. F. in *Practical Methods in Electron Microscopy - Dynamic Experiments in the Electron Microscope* (ed M. Glauert) Ch. 5, 239-308 (Elsevier Science Ltd 1981).

36 Creemer, J. F. *et al.* in *IEEE 22nd International Conference on Micro Electro Mechanical Systems, 2009. MEMS 2009.* 76-79.

37 Creemer, J. F. *et al.* Atomic-scale electron microscopy at ambient pressure. *Ultramicroscopy* **108**, 993-998 (2008).

38 Creemer, J. F. *et al.* A MEMS Reactor for Atomic-Scale Microscopy of Nanomaterials Under Industrially Relevant Conditions. *Journal of Microelectromechanical Systems* **19**, 254-264, doi:10.1109/jmems.2010.2041190 (2010).

39 Yokosawa, T., Alan, T., Pandraud, G., Dam, B. & Zandbergen, H. In-situ TEM on (de)hydrogenation of Pd at 0.5–4.5 bar hydrogen pressure and 20–400°C. *Ultramicroscopy* **112**, 47-52 (2012).

40 de Jonge, N., Bigelow, W. C. & Veith, G. M. Atmospheric Pressure Scanning Transmission Electron Microscopy. *Nano Letters* **10**, 1028-1031, doi:10.1021/nl904254g (2010).

41 Jonge, N. d., Peckys, D. B., Kremers, G. J. & Piston, D. W. Electron microscopy of whole cells in liquid with nanometer resolution. *Proceedings of the National Academy of Sciences* **106**, 2159-2164, doi:10.1073/pnas.0809567106 (2009).

Chapter 3 IN-SITU HEAT-TREATMENT[*]

We present a new approach to study the three-dimensional compositional and structural evolution of metal alloys during heat treatments such as commonly used for improving overall material properties. It relies on in situ heating in a high-resolution scanning transmission electron microscope (STEM). The approach is demonstrated using a commercial aluminium (Al) alloy AA2024 at 100–240°C, showing in unparalleled detail where and how precipitates nucleate, grow or dissolve. The observed size evolution of individual precipitates enables a separation between nucleation and growth phenomena, necessary for the development of refined growth models. We conclude that the in situ heating STEM approach opens a route to a much faster determination of the interplay between local compositions, heat-treatments, microstructure and mechanical properties of new alloys.

---

[*] Published as: Malladi SK, Xu Q, van Huis MA, Tichelaar FD, Batenburg KJ, Yücelen E, Dubiel B, Czyrska-Filemonowicz A, Zandbergen H. Real-Time Atomic Scale Imaging of Nanostructural Evolution in Aluminium Alloys. Nano Letters 2013. DOI: 10.1021/nl404565j

1. Background

Most commercial engineering alloys undergo heat treatments to change their intrinsic microstructural properties, such as elemental distribution and precipitate density, to enhance their extrinsic physical properties such as mechanical strength.[1-3] Despite the key importance of these treatments, studies of the compositional and structural evolution of alloys undergoing heat treatments are fragmented and time consuming as they have been carried out on a set of different samples taken at intermediate stages, which are in fact post-mortem data that do not show the evolution of the same area.[1-14]

Here, we present a novel *in situ* method to investigate the (atomic) structural and compositional evolution of alloys with time and temperature. At the core of this method is a (scanning) transmission electron microscope ((S)TEM) fitted with a specimen holder that allows *in situ* heating at minimal specimen drift, three-dimensional precipitate structure retrieval (tomography) and elemental mapping at the nanometre scale. We expect this *in situ* approach to become important to study new compositions, such as those suggested by computational methods.

As proof-of-principle of our approach, we studied the well-known commercial Al alloy AA2024. In short, from previous research it is established that subsequent heating stages induce the formation of precipitates inside the Al alloy, resulting in improved alloy strength through the well-known mechanism of “precipitation hardening”.[1-3] Specifically, it is reported that during aging at 100–240°C of a supersaturated solid solution obtained after quenching a heated Al alloy, clusters of 3–20 atoms are nucleated,[9] that either dissolve or grow into ~6-nm-long particles called Guinier–Preston–Bagaryatsky (GPB) zones.[3] By a complex compositional and structural evolution at the atomic level,[5-8] these GPB zones grow into intermediate precipitates or GP-II zones with a thickness of 1–4 nm and a length of 10–100 nm.[4,10] Upon further aging, the precipitates grow into laths a few hundred nanometres long and up to 10 nm wide. The existing knowledge on the nanostructural hierarchy[7] of precipitates in Al alloys is from a combination of high resolution microscopic techniques like atom probe tomography and high resolution (S)TEM on various specimens prepared from bulk samples that have undergone different heat-treatments. However, information of all stages of the evolution of an individual precipitate is missing. Here, we show the evolution of precipitates in a TEM specimen through *in situ* heating.

Over the past 50 years, various *in situ* TEM studies have been performed on precipitation in Al alloys with limited success.[15-19] Factors that have prohibited successful *in situ* TEM studies are specimen drift, limitations with elemental analysis techniques and electron beam damage. In recent years, new (e.g. MEMS-based) specimen holders[20] have succeeded in minimising drift to 0.1 nm per 10–100 s,[21] whereas very fast X-ray spectroscopy coupled with aberration-corrected (S)TEMs with a probe size of 0.1 nm using a low dwell time per pixel basically solves the latter two problems. TEM operation in scanning mode (STEM) has the advantage that it allows larger Al specimen thicknesses (150 nm) during high-resolution imaging in comparison to the TEM mode (50 nm). When combined, these instrumental innovations allow a powerful and fast approach to study the effects of heat treatment on alloys, of which we provide a first example.

2. Materials and Methods

2.1. Specimen preparation and transfer:

The material used for present study is wrought AA2024 with a chemical composition of Al-4.4Cu-1.5Mg-0.6Mn (wt. %). The routine heat treatment of the 2024 alloy consists on the solution annealing followed by aging. The as-received specimens of AA2024-T3 are in the form of strips, which are cut and mechanically polished using a series of silicon carbide (SiC) papers. The final polishing is done with a suspension of 0.05 µm colloidal alumina. The specimens for TEM investigation are prepared using a FEI Quanta DB-235 dual-beam SEM/FIB. Specimens measuring 10 µm × 5 µm × 150 nm are prepared for the present study and transferred to a MEMS-based resistive heating chip with an electron transparent region developed in-house.[21] An optical micrograph of a heating chip (Figure 3.1a) shows TEM specimens on electron-transparent membranes of the chip.

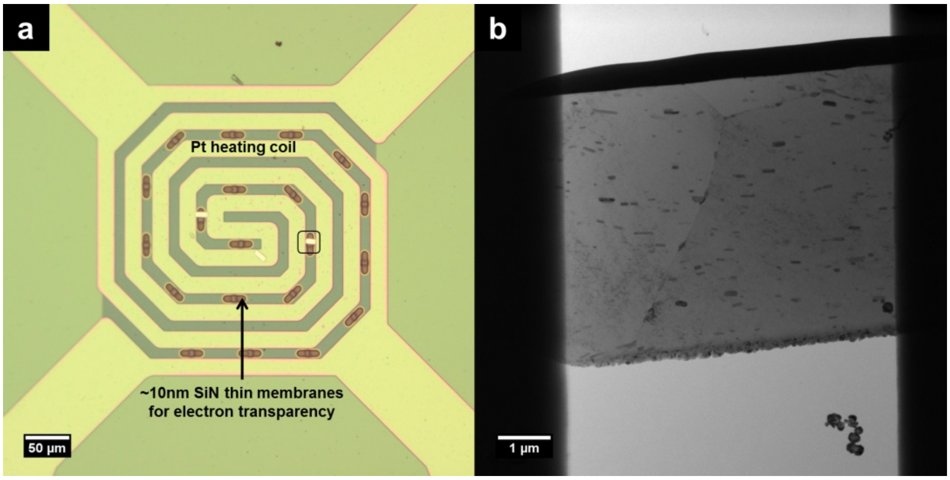

Figure 3.1: (a) Optical micrograph showing FIB lamellae on thin membranes of a MEMS based heating chip; (b) Bright-field TEM image of FIB lamellae indicated by the square in (a).

2.2. In-situ (S)TEM investigations:

The computer-controlled heating chip is introduced into the TEM using a low-drift heating holder from DENSsolutions (SH-70). The holder has a narrow tip allowing a large tilt of up to ±70°, making it possible to perform tomography. For HR-STEM experiments, a double-tilt, low-drift heating holder from DENSsolutions is used. The TEM investigations are performed in a FEI TITAN^3 and a probe-corrected FEI TITAN^3 60-300 equipped with ChemiSTEM™ technology (X-FEG, and Super-X detection system) [22] and operated at 300 kV in STEM mode. The combination of these tools makes it possible to acquire elemental maps of a region at 512 × 512 pixel resolution, with pixel size in the range of 50–0.01 nm (in principle), in a relatively short time (5 minutes in our case).

3. Results and Discussion

On a ~150-nm-thick AA2024 specimen heated *in situ* to 250°C for 2 minutes, annular dark-field STEM (ADF-STEM) imaging reveals the growth of lath-like nanoprecipitates (Figure 1a). We have performed six heat-treatment experiments on different specimens from room temperature to 500°C and a reproducible trend of elemental redistribution and precipitation is observed. From 180°C upwards, a change in the morphology of some grain-boundary precipitates is observed whereas the formation of elongated nanoprecipitates is observed within the temperature range of 200–300°C.

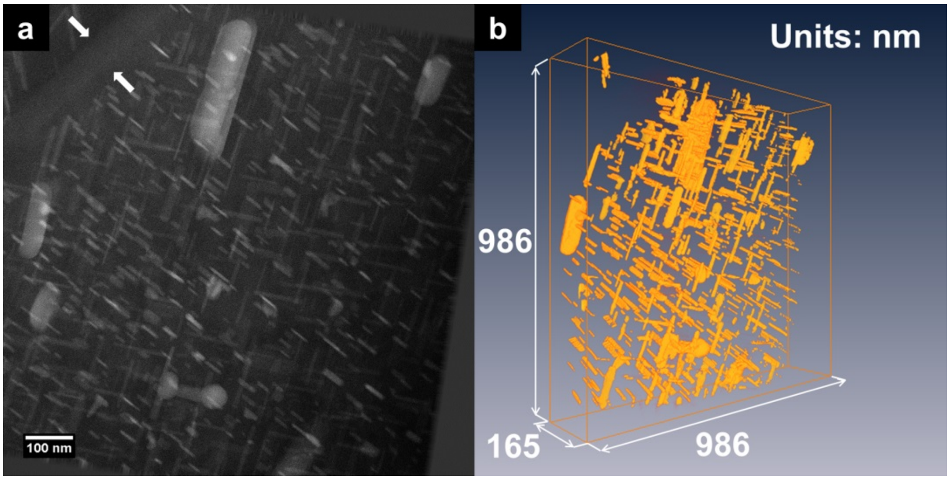

Figure 3.2: (a) ADF-STEM image obtained on heating an AA2024 specimen at 250°C for ~ 2 min, showing lath-like nanoprecipitates. From 91 such projections with tilt angles between −45° to +45°, the 3D distribution of the lath-like precipitates has been extracted as shown in (b).

ADF-STEM also allows a full 3D tomography (Supplementary Movie S1) of the precipitates.[23,24] The reconstructed precipitate distribution (Figure 3.2b, Supplementary Movie S2) reveals the presence of three families of precipitates, oriented along the $\langle 100\rangle_{Al}$ directions. It is evident that one of the three $\langle 100\rangle_{Al}$ families of the lath-like nanoprecipitates is present throughout the thickness of the specimen. Such precipitates are also reported for bulk precipitation.[13] Moreover, a precipitate-free zone at the grain boundary is observed (Figure 3.2a), which is noticed commonly in bulk specimens.[25] Analysis of two other STEM movies recorded at 250°C show similar behaviour. Although ~150 nm thick, the specimen clearly shows many features of relevance to bulk material. Surface effects are not fully absent, but their influence is suppressed due to the supersaturated condition of the Al matrix. The effective diffusion lengths of elements in the specimen much shorter than suggested by diffusion coefficients from literature (see Supplementary Table S1), which are only valid for the very dilute limit. In our case, the distance to the nearest trapping site is much shorter than the distance to the surface, so that the surface effects are limited to a region very close to the surface.

Having witnessed the temperature range of precipitation (for more details on heat-treatment, see Appendix D), to follow growth kinetics at an optimum rate, heat treatment is carried out at 225°C. The STEM movie (Supplementary Movie S3) recorded with an acquisition rate of one frame per 3 seconds shows the formation of individual precipitates after about 100 seconds. The snapshots (Figure 3.3a-c) from the movie show the intermediate stages. After 840 seconds, when no further changes are observed, the heating is stopped and a tilt-series of ADF-STEM images is acquired for tomographic reconstruction.

From the tilt-series (Supplementary Movie S4), it is observed that there are three families of precipitates, along the cube directions $\langle 100 \rangle$ of the Al matrix. We have designated the precipitates oriented at 29° to the specimen surface (seen perpendicular to the specimen surface Figure 3.3d) as [001] type, two of which are numbered 1 and 2, whereas the precipitates 3, 4 and 5, 6 are along the [100] and [010] directions respectively. Precipitates 1 and 2 are connected to dislocation loops. The length evolution of these six individual precipitates (Figure 3.3e) is deduced from Supplementary Movie S3. The precipitates 1 and 2 nucleate earlier in time but show the same growth characteristics as precipitates that are formed in the matrix. Thus the average width and length of the precipitates is plotted as a function of $t^{1/2}$ after synchronising the nucleation moments to t=0 (Figure 3.3f).

The width remains nearly constant, showing that growth in the lateral dimensions is interface limited. The average length increases approximately linearly with the square root of time, corresponding to classical volume diffusion controlled growth. The half-length is commonly expressed as:[26]

$$½L(t) = 2(\beta D)^{1/2} t^{1/2} \qquad (1)$$

where β is the dimensionless growth parameter, and D is the diffusivity of the slowest diffusing element in the precipitate, copper (Cu) ($D_{Cu} = 4.0 \times \cdot 10^{-19}$ m^{2}s^{-1} at 225 °C). The growth parameter is derived from the slope of the fitted linearity as β = 3.04.

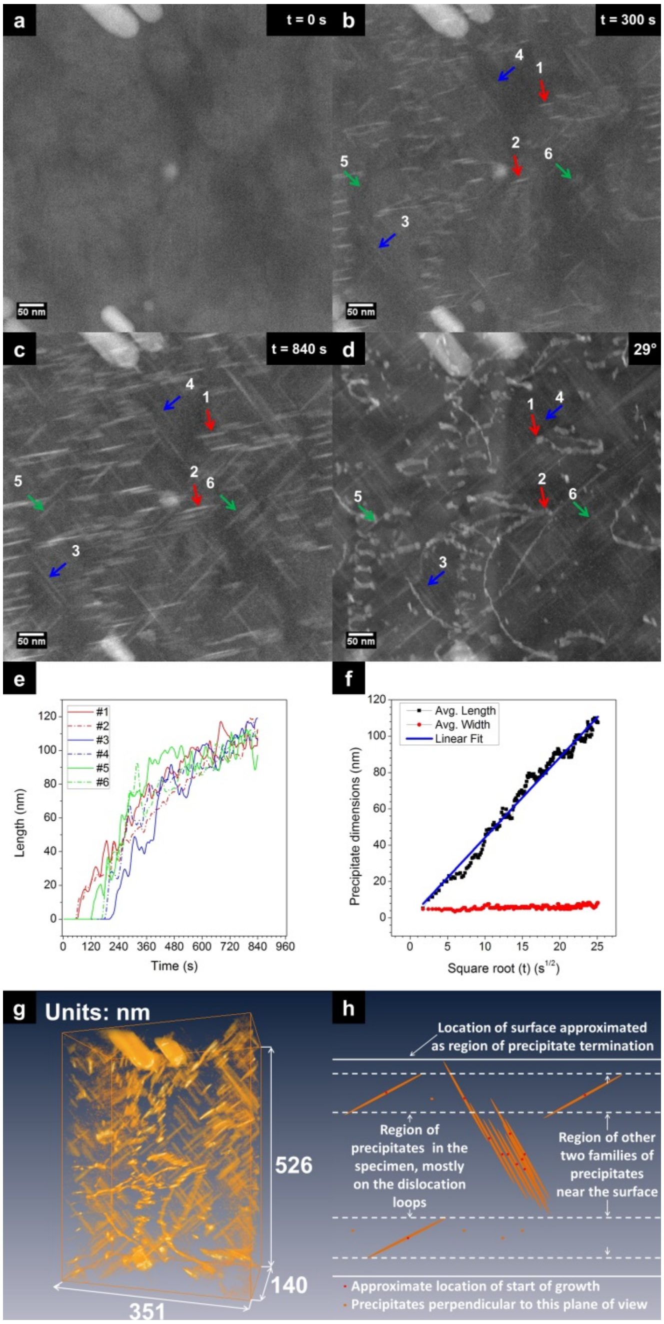

Figure 3.3: (a–c) Snapshots from an in situ ADF-STEM movie showing the growth of lath-like precipitates in AA2024 specimen aged at 225°C. (d) ADF-STEM image at 29° tilt showing that precipitates 1 and 2 are located on dislocation loops. (e) Plot of the length evolutions of the precipitates marked 1–6 with time. (f) Average length and average width of 6 precipitates monitored from the moment of nucleation, as a function of $t^{1/2}$*. (g) Slice from a 3D reconstruction obtained from a tilt series of 91 ADF-STEM images. (h) Conceptual sketch illustrating the distribution of precipitates in this specimen across the thickness. The surface (position determined within an accuracy of 5 nm) is not exactly parallel to the viewing direction.*

The 3-D reconstruction of the precipitates (Supplementary Movie S5, Figure 3.3g) show that the [001] type precipitates connected to dislocation loops are embedded within the specimen. The observation of precipitates nucleating at dislocations corresponds well with literature on bulk material.[13,15]

The two precipitate families along [100] and [010] directions are predominantly present ~ 20–40 nm under the foil surface, as schematically summarised from the 3D analysis (Figure 3.3h). Possible explanations for this kind of a region include surface stresses due to lattice relaxations, thermal expansion differences between the alloy and a surface oxide layer, specimen preparation effects, and a lower concentration of vacancies near the surface, leading to anisotropic vacancy-assisted solute diffusion.

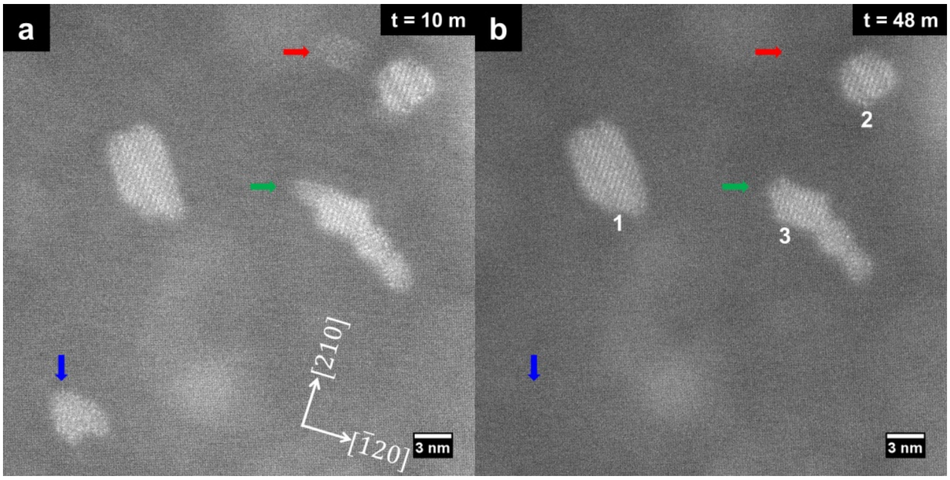

Figure 3.4: Snapshots from HR-STEM movie obtained after heating an AA2024 specimen to 200°C for (a) 10 min and (b) 48 min, showing S-phase type precipitates oriented parallel to the electron beam. The atomic clusters indicated by the arrows in (a) have disappeared in (b). At the same time, the precipitate close to the green arrow has become wider.

At a slightly lower heat treatment temperature (200°C) to allow the recording of high-resolution (HR) STEM movie (Supplementary Movie S6), evolution of the precipitates on the atomic scale is observed. Two snapshots from the movie zoom in on the evolution of S-phase-type precipitates (Figure 3.4). Clusters of solute atoms are observed in the matrix (blue and red arrows) and near a precipitate (green arrow). Over time, the atom clusters marked by the red and blue arrows disappear and consequently must either dissolve into the matrix or diffuse elsewhere, whereas the atom cluster indicated by the green arrow contributes to the growth of the crystalline part of the precipitate (Figure 3.4b). The common characteristic of these precipitates are the rows of bright dots along the $[210]_{Al}$ direction with a dot–dot distance of 4.5 Å, typical for the S phase (see for example [4]). The distance between these rows of dots is 6.3 Å, indicating a Cu, magnesium (Mg) rich ($CuMgAl_5$) composition (see Appendix D).

From the STEM movies (Figure 3.3 & Figure 3.4), time-resolved information is obtained from individual precipitates, which allows for separating nucleation and growth, in contrast to earlier TEM studies where average dimensions are considered of precipitates that nucleate at different moments in time. The detailed experimental information obtained using the current methodology will be required for developing and validating more advanced models, taking into account not only nucleation and growth of precipitates, but also the coalescence with precursor, GP zones.

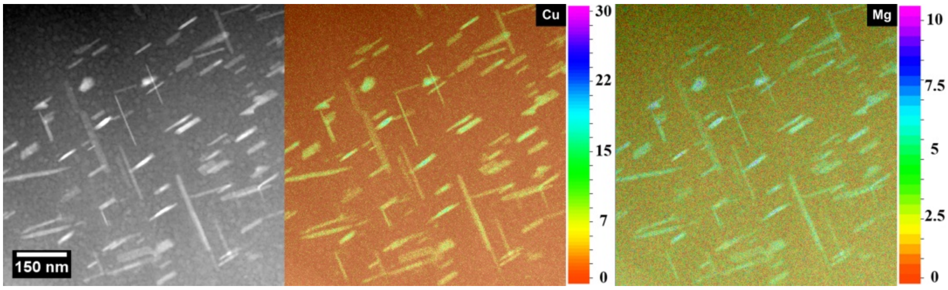

Figure 3.5: ADF-STEM image and corresponding EDX maps of Cu and Mg obtained at 250°C showing the presence of lath-like hardening precipitates, identified as S-type . The vertical scales indicate atomic %.

As a final application of our *in situ* analysis approach, we combine STEM imaging with element-compositional analysis of the observed phase transformations through energy-dispersive X-ray spectroscopy (EDX) maps. STEM image and EDX maps of Cu and Mg taken at 250°C of an area containing lath-like precipitates (Figure 3.5) show that all precipitates contain both Cu and Mg. The maps show that on an average the precipitates have a Cu/Mg ratio of 0.9 (±0.2), close to intermediate S-type precipitate compositions as reported in literature.[4,12,13] As the specimen is heated further to 300°C, the lath-like precipitates start dissolving and are completely dissolved beyond 330°C (see Appendix D).

4. Conclusions

Our experiments establish the analytical power of *in situ* heating combined with HR-STEM and compositional analysis. It succeeds in following the various stages of precipitation in Al alloys: formation of clusters of solute atoms, nucleation of precipitates on dislocations, growth of lath-like intermediate precipitates and the distribution of these precipitates in three dimensions and with nanoscale precision. The excellent correspondence of our *in situ* measurements on a submicron specimen with literature *ex situ* experiments on bulk highlights the validity of our approach for future studies of novel supersaturated composites. Even where the influence of the surfaces is felt (in a zone about 20–40 nm from both surfaces), the shape and evolution of the precipitates are nonetheless very similar to those in the bulk-like middle of the sample.

In addition to the increased speed of the dynamic structural analysis, we introduce the possibility of *in situ* observation of the evolution of *individual* precipitates. The concept of nanostructural hierarchy of nucleation and growth of precipitates is not just limited to solid solutions like aluminium alloys but has also been observed during the nucleation and growth of calcium phosphate[27,28] and magnetite[29] from liquid solutions. We expect that by in-situ TEM with liquid cells the evolution of a single particle in liquid solution can be followed, revealing much clearer the hierarchy. With the technology to achieve HR-STEM combined with *in situ* specimen heating and EDX now readily available, this analysis approach will accelerate and enrich the research on metallic alloys.

References

1 Guinier, A. Structure of Age-Hardened Aluminium-Copper Alloys. *Nature* **149**, 569-570 (1938).

2 Preston, G. D. The Diffraction of X-Rays by Age-Hardening Aluminium Copper Alloys. *Proceedings of the Royal Society of London. Series A. Mathematical and Physical Sciences* **167**, 526-538, doi:10.1098/rspa.1938.0152 (1938).

3 Silcock, J. M. *Journal of Institute of Metals* **89** (1960).

4 Wang, S. B. *et al.* Double-atomic-wall-based dynamic precipitates of the early-stage S-phase in AlCuMg alloys. *Acta Materialia* **60**, 6573-6580, doi:10.1016/j.actamat.2012.08.023 (2012).

5 Chen, J. H., Costan, E., van Huis, M. A., Xu, Q. & Zandbergen, H. W. Atomic Pillar-Based Nanoprecipitates Strengthen AlMgSi Alloys. *Science* **312**, 416-419, doi:10.1126/science.1124199 (2006).

6 Zandbergen, H. W., Andersen, S. J. & Jansen, J. Structure Determination of Mg5Si6 Particles in Al by Dynamic Electron Diffraction Studies. *Science* **277**, 1221-1225, doi:10.1126/science.277.5330.1221 (1997).

7 Liddicoat, P. V. *et al.* Nanostructural hierarchy increases the strength of aluminium alloys. *Nat Commun* **1**, doi:10.1038/ncomms1062 (2010).

8 Clouet, E. *et al.* Complex precipitation pathways in multicomponent alloys. *Nat Mater* **5**, 482-488, doi:10.1038/nmat1652 (2006).

9 Ringer, S. P., Hono, K., Sakurai, T. & Polmear, I. J. Cluster hardening in an aged Al-Cu-Mg alloy. *Scripta Materialia* **36**, 517-521, doi:10.1016/s1359-6462(96)00415-0 (1997).

10 Sha, G., Marceau, R. K. W., Gao, X., Muddle, B. C. & Ringer, S. P. Nanostructure of aluminium alloy 2024: Segregation, clustering and precipitation processes. *Acta Materialia* **59**, 1659-1670, doi:10.1016/j.actamat.2010.11.033 (2011).

11 Marth, P. E., Aaronson, H. I., Lorimer, G. W., Bartel, T. L. & Russell, K. C. Application of heterogeneous nucleation theory to precipitate nucleation at GP zones. *Metallurgical Transactions A* **7**, 1519-1528 (1976).

12 Khan, I. N., Starink, M. J. & Yan, J. L. A model for precipitation kinetics and strengthening in Al–Cu–Mg alloys. *Materials Science and Engineering: A* **472**, 66-74, doi:10.1016/j.msea.2007.03.033 (2008).

13 Shih, H.-C., Ho, N.-J. & Huang, J. Precipitation behaviors in Al-Cu-Mg and 2024 aluminum alloys. *Metallurgical and Materials Transactions A* **27**, 2479-2494 (1996).

14 Ringer, S. P. & Hono, K. Microstructural Evolution and Age Hardening in Aluminium Alloys: Atom Probe Field-Ion Microscopy and Transmission Electron Microscopy Studies. *Materials Characterization* **44**, 101-131, doi:10.1016/s1044-5803(99)00051-0 (2000).

15 Thomas, G. & Whelan, M. J. Observations of precipitation in thin foils of aluminium +4% copper alloy. *Philosophical Magazine* **6**, 1103-1114 (1961).

16 Butler, E. P. & Hale, K. F. in *Practical Methods in Electron Microscopy* Vol. 9 (ed M. Glauert) Ch. 1, 1-34 (Elsevier Science Ltd 1981).

17 Howe, J. M., Dahmen, U. & Gronsky, R. Atomic mechanisms of precipitate plate growth. *Philosophical Magazine A* **56**, 31-61 (1987).

18 Garg, A. & Howe, J. M. Nucleation and Growth of Omega Phase in Al-4.0 Cu-0.5 Mg-0.5 Ag Alloy. *Acta Metallurgica Et Materialia* **39**, 1925-1937 (1991).

19 Howe, J. M. & Benson, W. E. Determination of the Atomic Structure, Mechanisms and Kinetics of Precipitate Growth in Solids by *in situ* Hot-Stage High-Resolution Transmission Electron Microscopy. *Interface Science* **2**, 347-363 (1995).

20 Allard, L. F. *et al.* A new MEMS-based system for ultra-high-resolution imaging at elevated temperatures. *Microscopy Research and Technique* **72**, 208-215, doi:10.1002/jemt.20673 (2009).

21 van Huis, M. A. *et al.* Atomic Imaging of Phase Transitions and Morphology Transformations in Nanocrystals. *Advanced Materials* **21**, 4992-4995, doi:10.1002/adma.200902561 (2009).

22 Schlossmacher, P., Klenov, D. O., Freitag, B. & von Harrach, H. S. Enhanced Detection Sensitivity with a New Windowless XEDS System for AEM Based on Silicon Drift Detector Technology. *Microscopy Today* **18**, 14-20 (2010).

23 Batenburg, K. J. *et al.* 3D imaging of nanomaterials by discrete tomography. *Ultramicroscopy* **109**, 730-740, doi:http://dx.doi.org/10.1016/j.ultramic.2009.01.009 (2009).

24 Van Aert, S., Batenburg, K. J., Rossell, M. D., Erni, R. & Van Tendeloo, G. Three-dimensional atomic imaging of crystalline nanoparticles. *Nature* **470**, 374-377, doi:10.1038/nature09741 (2011).

25 Unwin, P. N. T., Lorimer, G. W. & Nicholson, R. B. The origin of the grain boundary precipitate free zone. *Acta Metallurgica* **17**, 1363-1377 (1969).

26 Ferrante, M. & Doherty, R. D. Influence of interfacial properties on the kinetics of precipitation and precipitate coarsening in aluminium-silver alloys. *Acta Metallurgica* **27**, 1603-1614, doi:10.1016/0001-6160(79)90043-9 (1979).

27 Dey, A. *et al.* The role of prenucleation clusters in surface-induced calcium phosphate crystallization. *Nat Mater* **9**, 1010-1014, doi:10.1038/nmat2900 (2010).

28 Habraken, W. J. E. M. *et al.* Ion-association complexes unite classical and non-classical theories for the biomimetic nucleation of calcium phosphate. *Nat Commun* **4**, doi:10.1038/ncomms2490 (2013).

29 Baumgartner, J. *et al.* Nucleation and growth of magnetite from solution. *Nat Mater* **12**, 310-314, doi:10.1038/nmat3558 (2013).

Appendix D

1. More details on heat-treatment experiments on AA2024

The initial heat-treatment experiments are performed by heating the specimen from room temperature upwards in steps of 20°C per minute and recording the images in bright-field (BF) TEM mode. The microstructure at room temperature consists of precipitates measuring 50(±20) nm × 50(±20) nm × 200 (±20) nm in the matrix and randomly shaped precipitates with sizes ranging from 0.3 to1.5 µm. Most of these matrix precipitates have been enriched with Manganese (Mn), identified from EDX as $Al_{20}Mn_2Cu_3$ type, whereas the grain-boundary precipitates are θ-type (Al_2Cu) or, in a few cases, S-phase type (Al_2CuMg) precipitates. On heating from room temperature to ~180°C, the microstructure remains the same. From 180°C onwards, significant changes in the size of grain-boundary precipitates are observed. Heating between 220˚C and 280°C, results in the formation of lath-like nano-precipitates. These lath-like precipitates are more evident in ADF-STEM mode (Figure D.1). Therefore, we decided to conduct heat-treatment experiments while imaging in STEM mode.

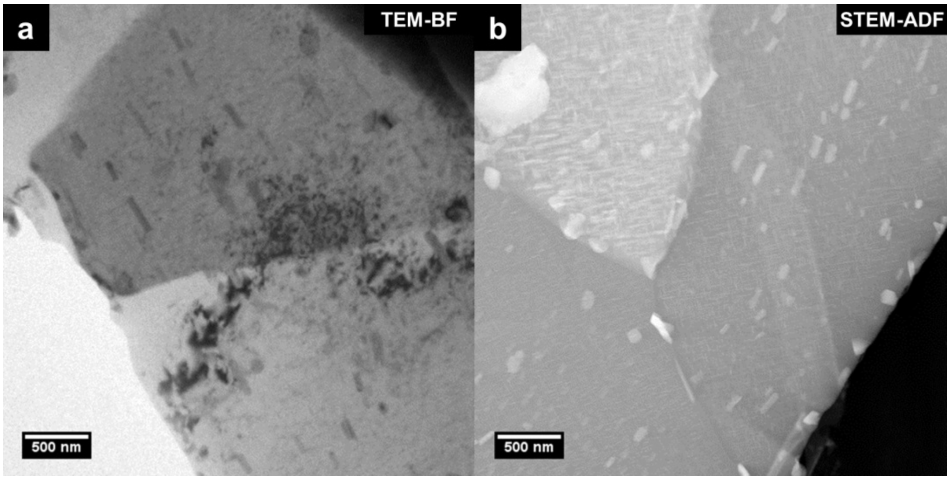

Figure D.1 Comparison of two images acquired from two different specimens in (a) BF-TEM and (b) STEM-ADF at 240°C. The lath-like S-phase type precipitates are better visible in STEM mode than in conventional BF-TEM mode.

Figure D.2 shows STEM-ADF images acquired at various stages while being heated from 120 to 360°C. The temperature is increased in steps of 30°C and at every stage the specimen is held at the set temperature first for ~1 min to observe any changes occurring at this temperature and then for ~5 min to obtain the EDX maps. The heating profile is shown at the bottom right corner in Figure D.2. The corresponding qualitative elemental maps are shown in Figure D.3.

From the heat-treatment and compositional analysis, it is observed that from room temperature to ~180°C, the microstructure of AA2024-T3 remains unchanged and is largely dominated by plate-type precipitates enriched in Cu and Mn as shown in the first row (100°C) of Figure D.3. Heating from 180°C upwards results in redistribution of Cu, indicated by a stronger Cu signal from the nodular features formed at the edge of the specimen. Moreover a change in the size of the grain-boundary precipitates enriched in Cu is also observed. From 220°C upwards, the formation of lath-like nanoprecipitates is observed. These precipitates are allowed to grow until 270°C and are mapped at a higher magnification at 270°C (peak-aged condition). The nanoprecipitates are identified as Cu and Mg containing S-phase type precipitates.

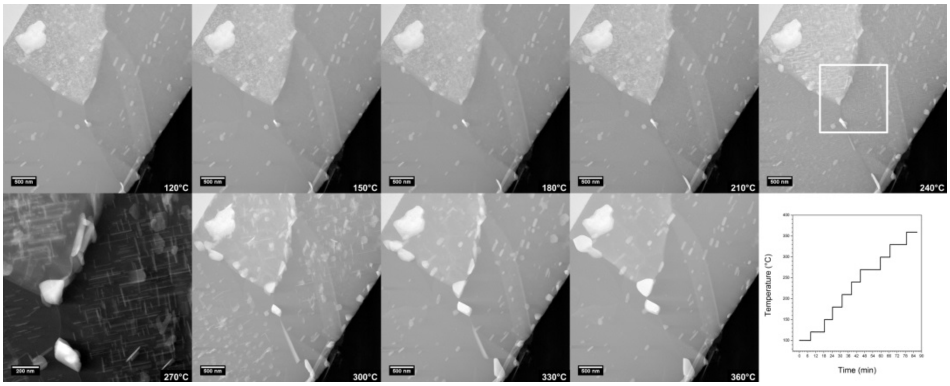

Figure D.2: STEM-ADF images acquired after heating the AA2024 FIB specimen at the mentioned temperatures using the heating profile shown on the bottom right corner. Notice the changes in the size of the grain-boundary precipitates. A higher magnification image of the area marked by the square in the image at 240°C is shown at 270°C to highlight the formation of lath-like nanoprecipitates in the matrix. Also, the presence of a precipitate-free zone close to the grain boundary is evident. The lath-like precipitates tend to dissolve back into the matrix beyond 300°C.

Heating beyond 300°C causes these precipitates to dissolve. At 330°C, the nanoprecipitates dissolve completely into the matrix, whereupon the Cu-rich grain-boundary precipitates start to shrink. Heating gradually from 330 to 410°C causes most of the Cu to dissolve from the precipitates to the matrix. Throughout the heating process, Mn-rich precipitates remain intact. The temperature range (250–300°C) as well as the time range (a few minutes) for the precipitation of nanoprecipitates is in agreement with the previously observed values by Thomas & Whelan[1] in model Al-Cu alloy, whereas studies on Al-Cu-Mg alloys have shown that the precipitation of large densities of S-phase-type precipitates is enhanced above 200°C. One such study using differential scanning calorimetry (DSC) shows the dominant exothermic heat effect between about 220°C and 280°C, which is associated with the formation of S-phase-type precipitates.[2] Figure D.4 shows the STEM-ADF images and the corresponding quantified elemental maps for Cu and Mg obtained at 200°C and 250°C from another specimen. In the region marked by the square in Figure D.4a, approximately ~3.4 at%

Cu and ~2 at% Mg is detected at 200°C, whereas after formation of the lath-like precipitates at 250°C, Figure D.4e, the matrix shows ~1.5 at% Cu and ~1.7% Mg. Most of the precipitates show ~10 at% Cu and ~9 at% Mg, and it is known that S-type precipitates have a Cu/Mg ratio close to 1. As the accuracy of determining the composition from EDX is within ± 1% and in this temperature range it is expected that S-type intermediate precipitates form in these alloys, they are identified as S-type precipitates. The most notable compositional change from this EDX study is the decrease in matrix Cu content from 3.4 at% to 1.5 at% before and after precipitation.

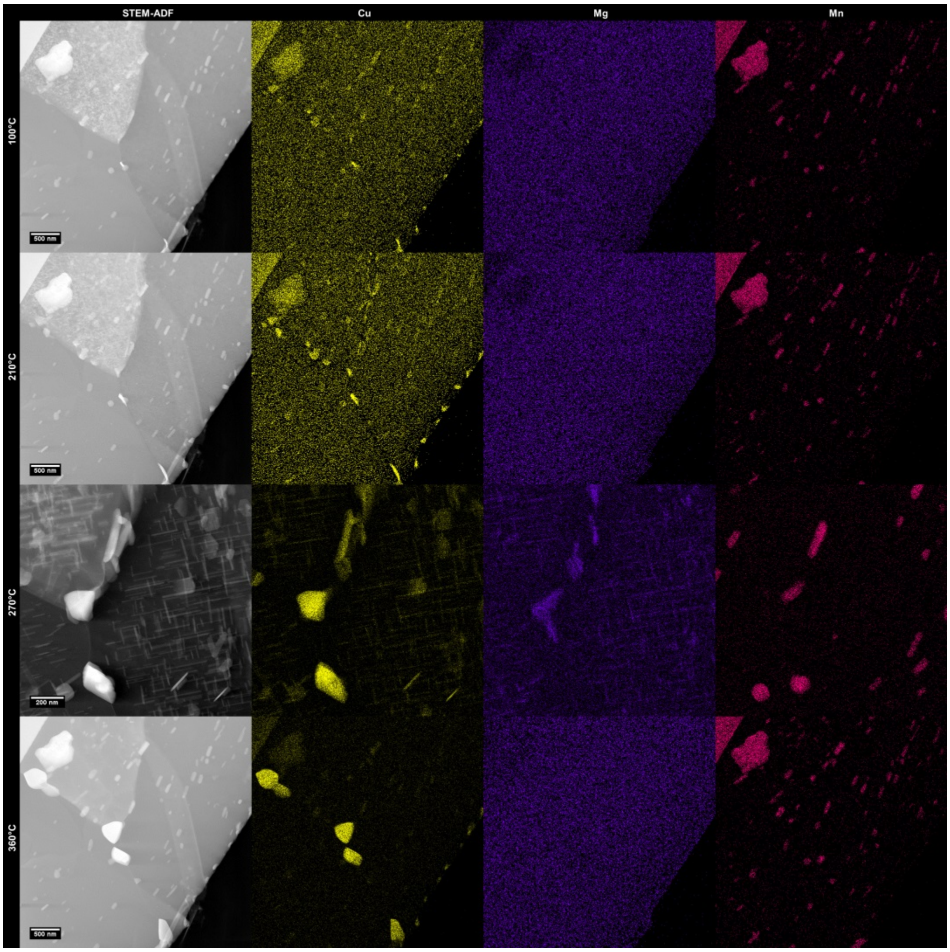

Figure D.3: Qualitative EDX maps obtained at each of the intermediate stages of heat-treatment shown in Figure D.2. These maps are obtained with a frame size of 512×512 pixels^2 and a frame time of 100 s, averaged over three frames. Notice the Cu redistribution associated with the precipitation at grain boundaries and precipitation in the matrix during the heat-treatment processes. The lath-like nanoprecipitates are enriched with Cu and Mg, suggesting S-phase-type compositions. Throughout the heat-treatment process, the Mn-rich precipitates remained as they are at room temperature.

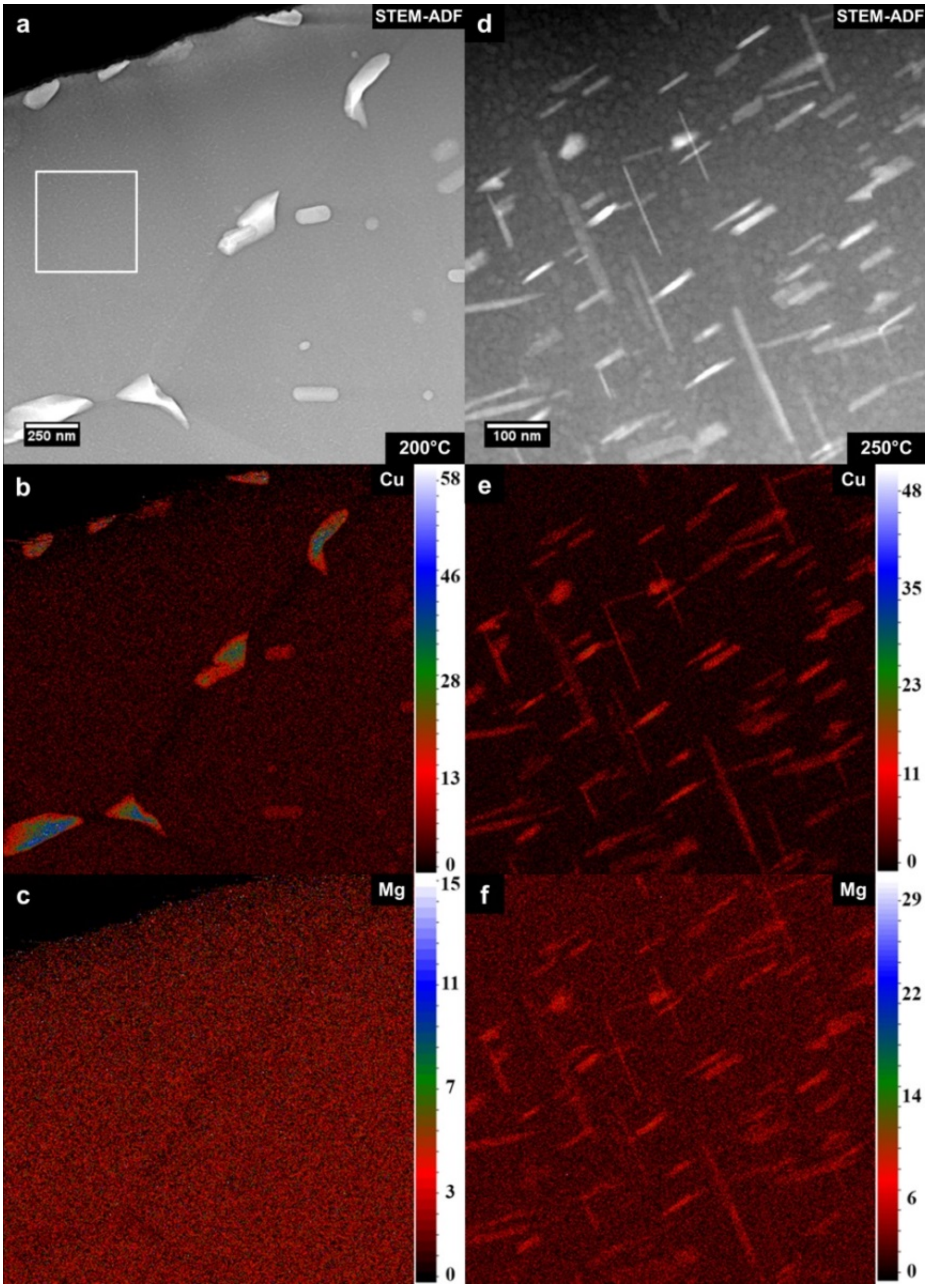

Figure D.4: STEM-ADF and corresponding quantitative EDX maps obtained at (a-c) 200°C and (d-f) 250°C. The maps at 250°C obtained from the region marked by the square in (a) show a decrease in matrix Cu content from ~4 at.% to ~1 at.%, whereas the lath-like precipitates are enriched with ~20 at.% Cu. A similar trend is observed in case of Mg: they show a decrease in matrix Mg content from ~3 at.% to 1 at.% while the precipitates are enriched with ~8 at.% Mg.

2. Details on discrete tomography

The images obtained in a TEM are essentially two-dimensional (2D) projections of the cross section on which the electron beam is incident. In order to obtain three-dimensional (3D) information from a TEM specimen, it is necessary to perform tomography where the specimen is tilted over a large angular range and projections are obtained at each of the intermediate steps. For conventional reconstruction methods such as back projection schemes and the simultaneous iterative reconstructive technique (SIRT), it is preferable to have more than 100 projections, tilting the sample in steps of 1–2° over a range of at least ±60°. However, in this study, we have employed the discrete algebraic reconstruction technique (DART)[3] from STEM-ADF images acquired in steps of 1° over a range of ±45°.

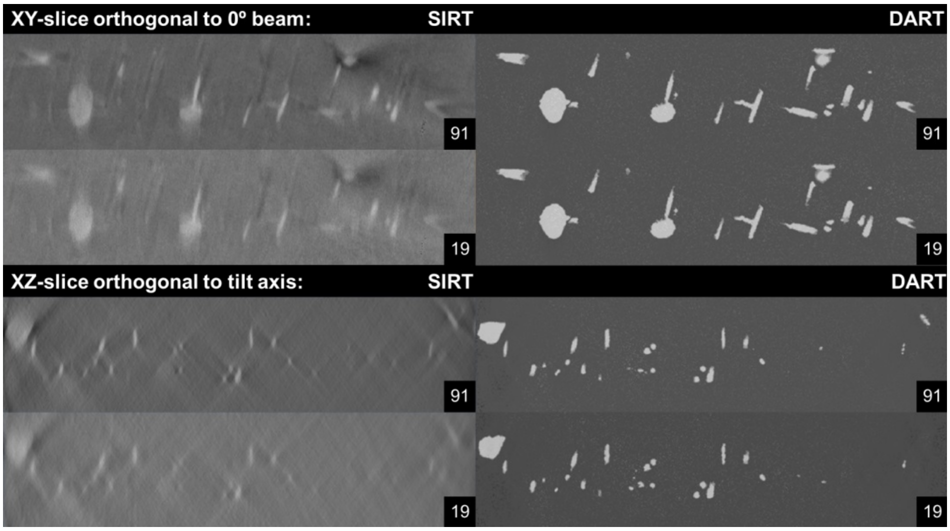

Figure D.5: Comparison between the reconstructions based on SIRT and DART algorithms using 91 (1° step) and 19 projections (5° step) from STEM-ADF images obtained within a tilt range of ±45°.

The DART method is based on the assumption that a 3D reconstruction of the specimen should contain only one grey level for each of the compositions in the specimen, which is very much valid for the precipitates of a particular morphology at a given temperature. Taking advantage of this property, the DART algorithm operates by applying a sequence of alternating reconstruction and segmentation steps. Each reconstruction step operates only on the boundary of the features (precipitates in this case), which is identified by thresholding the reconstruction from the previous step. Figure D.5 shows a comparison of slices from SIRT and DART reconstruction methods respectively. By using this method, either the quality of the reconstruction can be improved significantly, or the number of required projection images can be reduced.

Although the discrete tomography technique is capable of accurate reconstruction from a limited angular range, the relatively small range from −45 to +45 degrees used in these experiments can still introduce some elongation effects of the precipitates perpendicular to the viewing direction, (Figure 3.3g). For the reconstructions in this study, the surface of the sample is determined by selecting the termination points of the precipitates that extend the most to each side and the distance between these points corresponds to the specimen thickness. Owing to blurring effects at the boundaries of the precipitates, we estimate that these points are determined within an accuracy of 5 voxels, corresponding to a length of 5 nm for the first dataset (Figure 3.2 and Supplementary Movie S2) and 3 nm for the second data set (Figure 3.3 and Supplementary Movie S5). A more accurate determination of the surface could be done by using markers as is commonly done in life science TEM tomography.

3. Analysis of growth kinetics from experimental *in situ* precipitation data

Figure 3.3e and Supporting Supplementary Movie S3 allow extracting detailed, time-resolved information on the growth kinetics. The precipitates that are formed at dislocations nucleate earlier in time but show the same growth characteristics as precipitates that are formed free in the matrix. Figure D.6 shows the average width and length as a function of $t^{1/2}$ (after synchronising the nucleation moments to t=0). The width remains nearly constant, showing that growth in the lateral dimensions is interface limited. There is one-dimensional growth in the length direction.

From Figure D.6 it is clear that the average length increases linearly with the square root of time, corresponding to classical volume diffusion controlled growth. The half-length is commonly expressed:[4]

$$½L(t) = 2(\beta D)^{1/2} t^{1/2}$$

Where β is the dimensionless growth parameter, and D is the diffusivity of the slowest diffusing element (Cu, $D_{\mathrm{Cu}} = 4.0\cdot10^{-19}\ \mathrm{m^2s^{-1}}$ at a temperature of 225 °C). The growth parameter can be derived from the slope $dL/d(t^{1/2}) = 4(\beta D)^{1/2}$ of the linear fit for the average precipitate dimensions and is displayed in Figure D.6b. The growth rate is lower at longer annealing times, which may be caused by a lower level of supersaturation after precipitation, or by the limited thickness of the slab (140 nm). At shorter annealing times, the growth rate is also lower.

Figure 3.4 reveals unique additional information on the growth process which cannot be obtained with any other experimental method: the precipitation process consists of more than just atomic diffusion, as in the early stages atomic clusters coalesce with the S-type precipitates thereby contributing to their growth. Until now, in TEM studies, average dimensions of precipitates that have nucleated at different moments in time are considered. However with the current methodology, time-resolved information is obtained from individual precipitates, which allows separating nucleation and growth, so that much more reliable values for the growth parameter β are obtained. The present findings call for more advanced growth models, taking into account not only nucleation and growth of precipitates, but also the coalescence with precursor, GP zones. The detailed experimental information obtained using the current methodology will be required for developing and validating such advanced models.

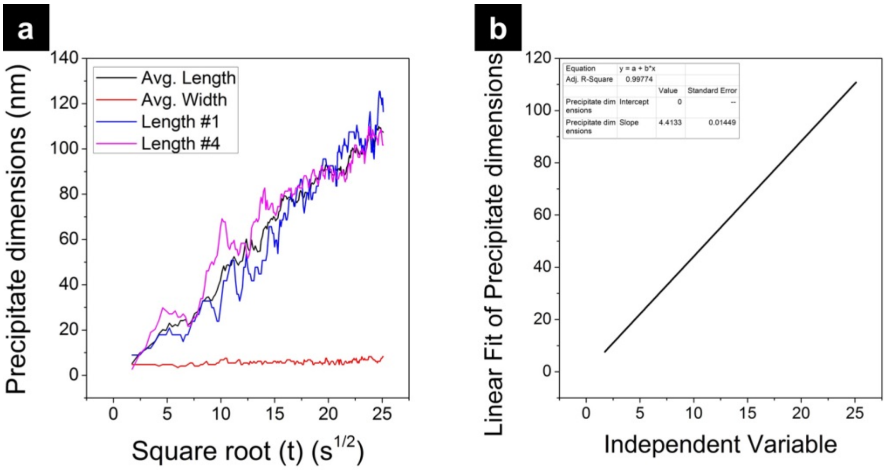

Equation	y = a + b*x		
Adj. R-Square	0.99774		
		Value	Standard Error
Precipitate dimensions	Intercept	0	--
Precipitate dimensions	Slope	4.4133	0.01449

Figure D.6: (a) Precipitate dimensions monitored from the moment of nucleation, as a function of $t^{1/2}$. (b) Growth parameter β = 3.04, derived from the slope of the linear fit from the average precipitate length in (a).

4. Analysis of the HR-STEM images of the precipitates

The STEM images in Figure 3.4 (from chapter 3) and Supplementary Movie S6 are rather fuzzy compared to STEM images reported in the literature,[5] because our specimen thickness (150 nm) is optimised to follow the evolution of the precipitates and not to achieve the best resolution, which requires a thickness of no more than 50 nm. Nevertheless, it is clear from our STEM images that there are strings of bright dots 4.5 Å apart along the [210] direction (see Figure 3.4), which fit well with the Al lattice. The fact that these dots are bright suggests that they are Cu or Cu-rich columns. The S-phase has this specific feature of the Cu $(210)_{Al}$ planes, where in the neighbouring (210) plane Al is replaced by Mg (Mg is larger than Al and Cu smaller than Al, compensating largely each other's volume change), thus forming a Cu-Mg slab. The distance between the slabs can vary according to the literature[5]. A sequence of slab–slab distances is shown in Figure D.7, leading to compositions of $CuMgAl_n$. The distance as well as the relative positions of the bright dots in the STEM image fit well with the model for $CuMgAl_5$. The precipitates are clearly not single crystalline; there are bands without a clear presence of the CuMg slabs. These are likely due to antiphase boundaries.

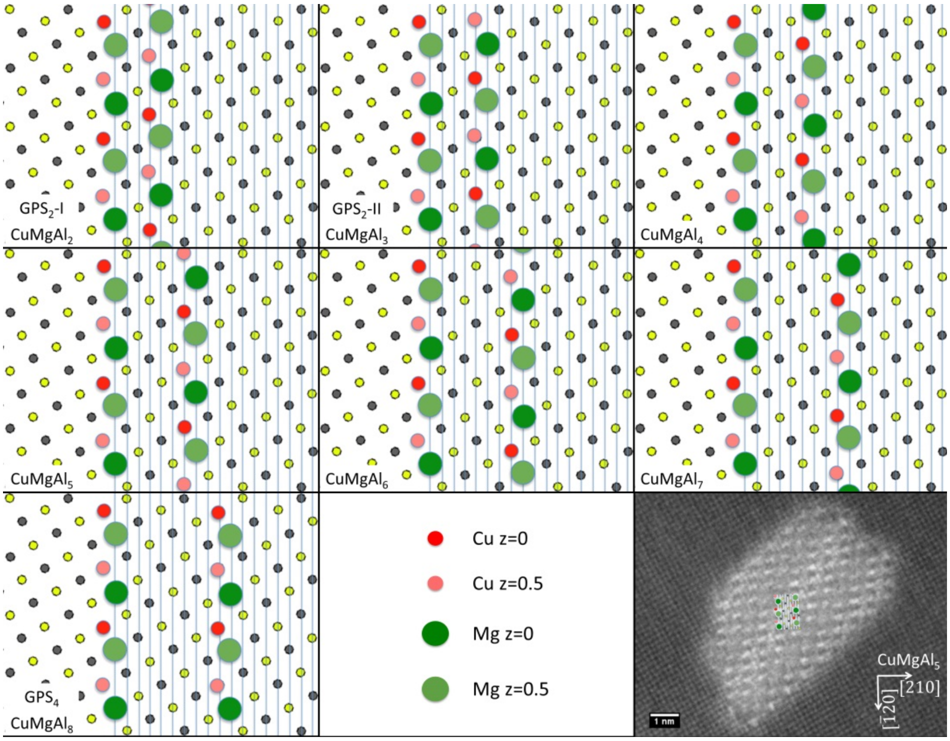

Figure D.7: Sequence of slab–slab distances leading to compositions CuMgAl$_n$ during the growth of S-type intermediate precipitates in AA2024. The compositions previously identified as GPS-type are also mentioned here. The heights of the Cu and Mg atoms refer to the positions in the Al lattice. For precipitate 1 in Figure 3.4, the distance as well as the relative positions of the bright dots in the STEM image fit well with the model for CuMgAl$_5$, as shown by the overlay in the image at the bottom right corner.

5. Experimental limitations

While carrying out the *in situ* TEM experiments, it is important to know the limitations and select a suitable window for experiments for proper interpretation of the results. This is because the TEM specimens have a large surface-to-volume ratio and thus some of the constraints of the surrounding material found in bulk specimens are absent. In this section, we describe the experimental constraints related to heating and beam damage encountered during our experiments.

5.1. Thermal grooving

When the Al alloy specimens are heated for longer than 30 min at temperatures higher than 400°C, we observed in STEM mode the formation of a dark zone close to the grain boundary (Figure D.8a). These are regions depleted of Al, as shown by the elemental map (Figure D.8b). This depletion, called grain boundary grooving, is caused by atoms moving away from the intersection of a grain boundary and the free surface, such that the contact angles between the free surfaces of the two grains and the grain boundary obtain an equilibrium value dictated by the respective surface energies. The atom movements are made possible by surface diffusion at higher temperature. Thermal grooving can be avoided by performing the solution heat treatment at 400°C for short durations (usually less than 10 min).

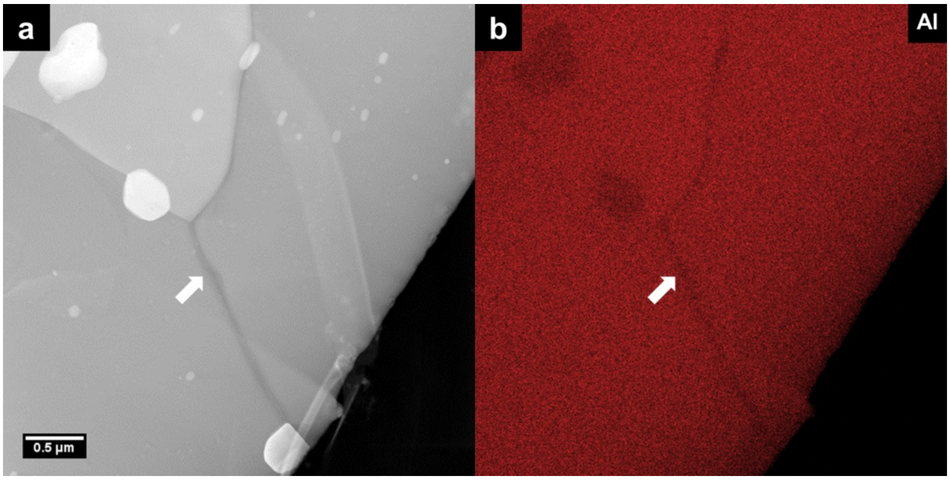

Figure D.8: (a) STEM-ADF and the corresponding elemental map (b) showing the thermal-grooving at the grain boundary after holding an AA2024 specimen at temperatures higher than 400°C for longer than 30 min.

5.2. Surface diffusion at specimen edges

Heating at temperatures higher than 450°C also results in surface diffusion from the edges of the specimen as shown in Figure D.9. The temperature at which this surface diffusion starts varies from specimen to specimen but it is usually observed to start from thinner regions of the specimen close to the edge. Once this takes place, the specimen becomes unusable for further quenching and aging experiments.

5.3. Electron beam damage

Electron beam-induced damage is a very well-known problem in TEM. To minimise the beam damage while enhancing contrast, all our experiments are performed in STEM mode, whereby the short dwell time of the beam minimises beam damage. However, while acquiring the EDX maps, we tried several combinations to maximise the signal for EDX mapping.

The EDX maps are obtained using a probe-corrected FEI TITAN^3 60-300 equipped with ChemiSTEM™ technology (X-FEG, and Super-X detection system). All the maps presented here have a frame size of 512×512 pixels^2 with a frame time of 100 s, averaged over three frames, and a probe current of ~0.3 nA, making the effective acquisition time 5 min. In order to accelerate the EDX acquisition, we tried increasing the probe current by a factor of 10 by changing the spot size. However, this resulted in severe beam damage.

Figure D.10 shows a comparison of an image obtained using probe currents of ~0.3 and ~3 nA respectively. Attempts to obtain EDX maps using a probe current of ~3 nA haven't been successful due to the beam damage (formation of holes in the specimen).

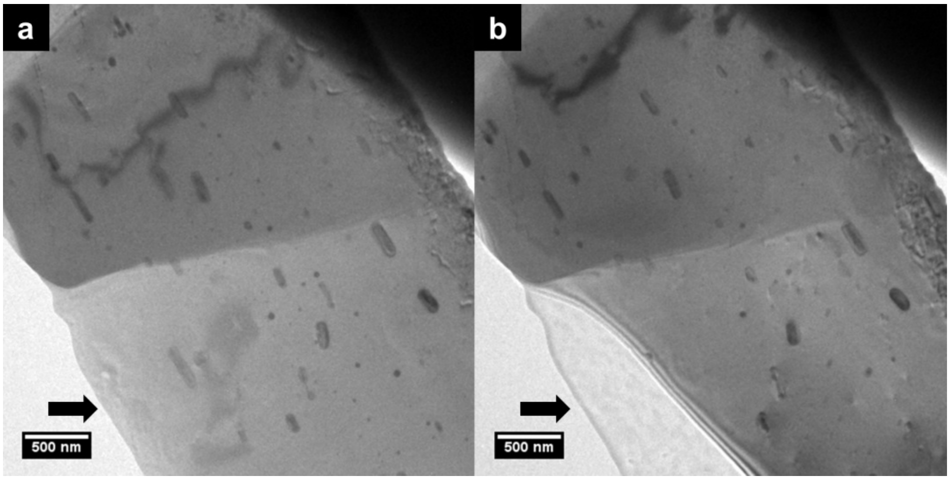

Figure D.9: Bright-field TEM images of an AA2024 specimen (a) just when the temperature is raised to 450°C and (b) 10 seconds after the temperature reaches 450°C, shows the large surface diffusion from the edge of the specimen as indicated by the arrow. Note that surface contamination/oxide remains behind.

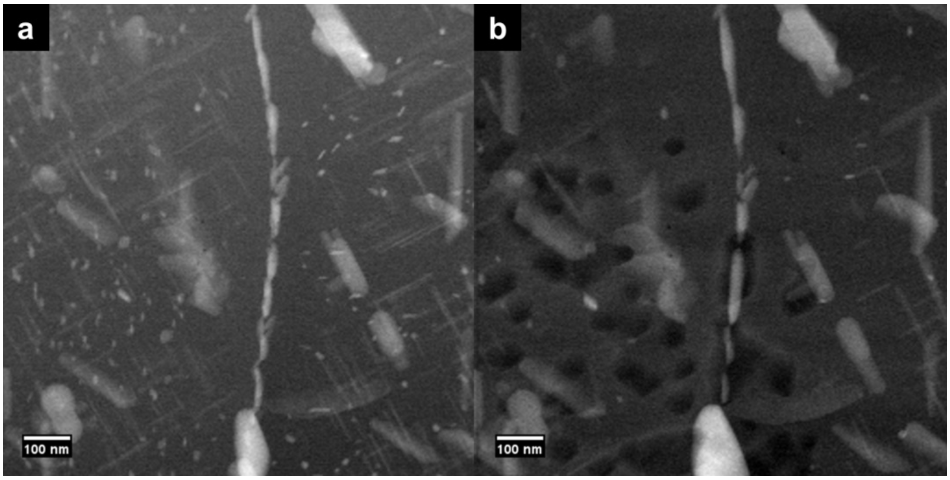

Figure D.10: STEM-ADF images using a probe current of ***(a)*** *~0.3 nA, the usual probe current for EDX maps in this study with a frame time of 100 s for an area of 512×512 pixels^2 and* ***(b)*** *~3 nA to improve the acquisition times. At higher probe currents, significant specimen damage, formation of holes that show up as dark areas in the square, is observed.*

6. STEM movie analysis using FIJI/ImageJ

Figure D.11a shows an STEM image acquired from the end of the Supplementary Movie S3. In this section, we describe the process used to acquire the length of one of the precipitates marked 1 in Figure D.11a. In order to enhance the contrast of the edges of the precipitate, the image stack is first duplicated and processed using a Gaussian blur (sigma radius 2.00). Then the original image stack is divided by the processed image stack to produce a stack of images with sharp precipitate edges. Next, the image stack is aligned to make the precipitate of interest vertical as shown in Figure D.11b, is a snapshot of the end of such an image stack. This is done because the rest of the procedure is conducted straightforwardly with the existing plug-ins. Subsequently, the precipitate of interest is isolated and the orthogonal views of this precipitate are generated. Figure D.11c is an YZ (length-time) projection of an image stack of precipitate 1 in Figure D.11a. The pixels along the horizontal axis of this image correspond to each frame from the image stack, which in turn represents the time. The pixels along the vertical direction correspond to the change in the length of the precipitate along the vertical axis from each of the frames of the image stack. To determine the length of the precipitate, first a bare outline map, Figure D.11d, is extracted from the 'Analyze Particles' plugin for ImageJ[6] after selecting the appropriate threshold level. All the pixels outside the outline are set to 0 and the pixels inside the outline are set to 1 to generate a bitmap image as shown in Figure D.11e. The length of the precipitates is then calculated by adding the pixels along the vertical axis and multiplying with the pixel size from the STEM images.

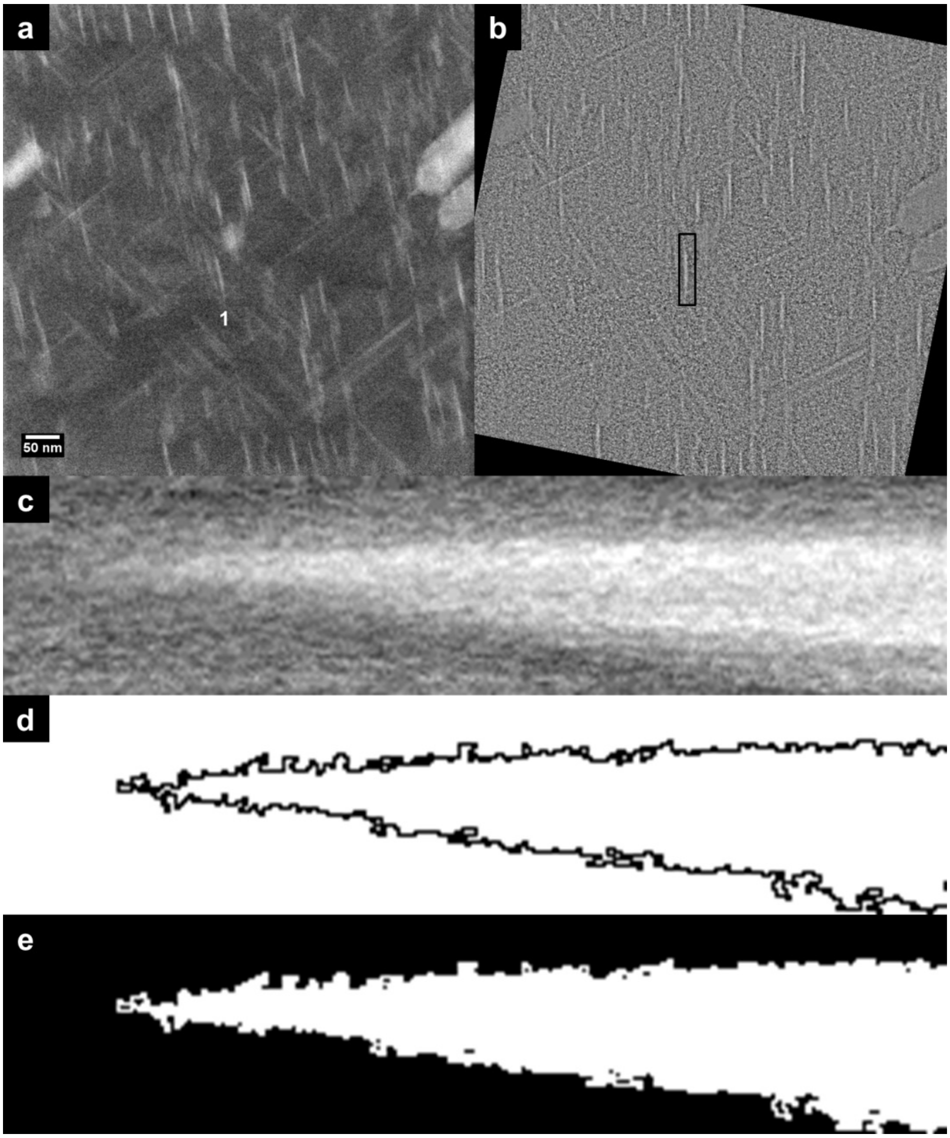

Figure D.11: (a) Snapshot obtained from the end of an STEM-ADF movie (Supplementary Movie S3). (b) Final frame of the same movie after applying a Gaussian blur and rotating the image to make one family of precipitates vertical. (c) Orthogonal view, YZ (length-time) projection shows the contrast variation from the image stack due to the increase in the precipitate length marked by a rectangle in (b). (d) Outline map of (c) generated by setting appropriate thresholds. (e) Bitmap image where all the pixels outside the outline are set to 0 and inside to 1. From (e), the summation of pixels along the y-axis now gives the change in length of precipitate with time.

7. List of movies and captions

Supplementary Movie S1: Aligned STEM-ADF movie showing tilt series of 91 STEM-ADF images acquired between −45° to +45° from a specimen heated at 250°C for approximately 2 minutes. The angle corresponding to the projection is shown at the top left corner of the movie. In this movie, the tilt axis is along the central vertical of the images.

Supplementary Movie S2: Reconstructed tomogram from STEM-ADF tilt-series shown in Supplementary Movie S1. In this movie, the tomogram is rotated by 360° about the vertical tilt axis at the centre of the reconstructed volume.

Supplementary Movie S3: STEM-ADF movie showing the growth of precipitates in a FIB specimen of AA2024 heated at 225°C. The time (in seconds) for which the specimen is held at this temperature from the moment it is set at 225°C is shown on the top left corner.

Supplementary Movie S4: Aligned STEM-ADF movie showing tilt series of 91 STEM-ADF images acquired between −45° to +45° from the specimen after heating at 225°C for 840 s (Supplementary Movie S3). The angle corresponding to the projection is shown at the top left corner of the movie. In this movie, the tilt axis is along the central vertical of the images.

Supplementary Movie S5: Reconstructed tomogram from STEM-ADF tilt-series shown in movie S4. In this movie, the tomogram is rotated by 360° about the vertical tilt axis at the centre of the reconstructed volume. At specific orientations, each of the three families of precipitates that have grown along the $\{100\}_{Al}$, i.e. precipitates along the dislocations at the middle of the foil, two families of precipitates relatively parallel to the surface are evident.

Supplementary Movie S6: HR-STEM movie of a FIB specimen of AA2024 heated at 200°C showing the growth of one of the precipitates as well as the dissolution of two of the atom clusters. The acquisition of the movie starts approximately 10 minutes after the temperature is set to 200°C at the rate of 2 minutes per frame. The initial 10 minutes are spent locating the appropriate region as well as making the necessary alignments for carrying out the HR-STEM studies.

Supplementary Movie S7: STEM-ADF movie showing the growth of precipitates in a FIB specimen of AA2024 heated at 250°C. The time for which the specimen is held at this temperature from the moment it is set at 250°C is shown next to the scale bar. After the acquisition of the movie stopped, EDX maps obtained from this region are shown in Figure 3.5.

References

1 Thomas, G. & Whelan, M. J. Observations of precipitation in thin foils of aluminium +4% copper alloy. *Philosophical Magazine* **6**, 1103-1114 (1961).

2 Khan, I. N., Starink, M. J. & Yan, J. L. A model for precipitation kinetics and strengthening in Al–Cu–Mg alloys. *Materials Science and Engineering: A* **472**, 66-74, doi:10.1016/j.msea.2007.03.033 (2008).

3 Batenburg, K. J. *et al.* 3D imaging of nanomaterials by discrete tomography. *Ultramicroscopy* **109**, 730-740, doi:http://dx.doi.org/10.1016/j.ultramic.2009.01.009 (2009).

4 Ferrante, M. & Doherty, R. D. Influence of interfacial properties on the kinetics of precipitation and precipitate coarsening in aluminium-silver alloys. *Acta Metallurgica* **27**, 1603-1614, doi:10.1016/0001-6160(79)90043-9 (1979).

5 Wang, S. B. *et al.* Double-atomic-wall-based dynamic precipitates of the early-stage S-phase in AlCuMg alloys. *Acta Materialia* **60**, 6573-6580, doi:10.1016/j.actamat.2012.08.023 (2012).

6 Schindelin, J. *et al.* Fiji: an open-source platform for biological-image analysis. *Nature Methods* **9**, 676-682, doi:10.1038/nmeth.2019 (2012).

Chapter 4 EX-SITU CORROSION STUDIES[*]

Localised corrosion in aluminium (Al) alloy AA2024-T3 specimen is investigated by ex situ TEM studies to determine an experimental window for real in situ TEM corrosion studies. In the as-prepared specimens, intermetallic phases leading to local galvanic couples are classified based on the size and composition. The corrosion behaviour of the TEM specimens is investigated in two kinds of corrosive environments, 1M sodium chloride (NaCl), and oxygen (O_2) bubbled through aqueous (aq.) hydrochloric acid (HCl) of pH=3. In the specimens exposed to a NaCl environment for duration of 30 min, remnant copper (Cu) rich particles as a result of de-alloying are observed and energy filtered TEM (EFTEM) elemental maps reveal the pitting of the oxide film at grain boundaries. In addition, severe deposition of NaCl crystals on the specimen surface is detected, making NaCl environment unsuitable for in situ TEM studies. Exposure to O_2 bubbled through aq. HCl for durations of 20, 40 and 60 min show different stages of localised corrosion in this alloy. EFTEM elemental maps confirm that the remnants formed during the de-alloying are Cu-rich while most of the corroded regions show O-rich corrosion products. The corrosion behaviour of the AA2024-T3 TEM samples is in agreement with corrosion of bulk material reported in the literature. Thus, O_2 bubbled through aq. HCl is considered a suitable environment for carrying out in situ corrosion experiments in the TEM.

---

[*] Published as: Malladi SRK, Xu Q, Tichelaar FD, Zandbergen HW, Hannour F, Mol JMC, Terryn H. Early stages during localised corrosion of AA2024 TEM specimens in chloride environment. Surface and Interface Analysis 2012. DOI: 10.1002/sia.5193

1. Background

Localised corrosion is a severe problem in most of the industrial Al alloys.[1] There are several intermetallic precipitates, dispersoids, and segregated regions like precipitate free zones etc., which exhibit distinctly different electrochemical characteristics compared to the surrounding microstructure and affect the corrosion behaviour of these alloys.[2] From a localised corrosion perspective, the dominant feature of alloy microstructures is the distribution of second-phase particles. For example, a network of second-phase particles at grain boundaries can lead to intergranular corrosion.[3] Extensive studies have been carried out to understand the initiation of localised corrosion at various precipitates in model Al alloys[4-8] as well as in commercial Al alloys,[9-18] using electrochemical methods and surface analysis techniques. From these studies, it has been well established that the precipitates can broadly be classified into two types: anodic, which are active with respect to the matrix; and cathodic, which are more noble with respect to the matrix. When the precipitates are cathodic than the matrix, a circumferential attack is observed in the matrix. On the other hand, when the precipitate is anodic with respect to the matrix, selective dissolution of the intermetallic particle itself occurs.

Localised corrosion in AA2024 has been thoroughly investigated and it is understood that the matrix as well as eight intermetallic phases contribute to the complicated nature of localised corrosion in this alloy.[3] The anodic precipitates containing magnesium (Mg) (Al_2CuMg, AlCuMg, $Al_5Mg_2Cu_6$ types) are the most significant ones at which a localised corrosive attack can initiate.[19] The initiation of corrosive attack is favoured in the presence of active species like chloride (Cl^-) ions. Recent studies[9,10] on the corrosion behaviour of AA2024 in Cl^- media show that the localised attack progresses in the following sequence: First, a progressive attack on the anodic type S-phase (Al_2CuMg) occurs, which undergoes de-alloying; this is followed by a circumferential attack around iron (Fe), manganese (Mn) rich cathodic type (Cu-Fe-Mn) phases, also called trenching. Most of the earlier studies give an indication of the behaviour of intermetallic particles, which are a few microns in size, analysed over a relatively large area. For the study of the corrosion behaviour on the nanoscale at precipitates and interfaces, TEM has proven to be an effective tool.[6,7] TEM has been used extensively to characterise the intermetallic precipitates, distribution of these precipitates, to identify and analyse the elemental depletion profiles across grain boundaries and precipitates before and after exposure to corrosive environments.[15,20-23]

The present work focuses on understanding the corrosion at grain boundaries and interfaces in AA2024-T3 by *ex situ* experiments as a preliminary step to *in situ* TEM corrosion studies using a MEMS based nanoreactor.[24,25] The nanoreactor consists of two facing dies made with thin-film technology on a silicon (Si) substrate. A platinum

(Pt) wire is embedded in the bottom die of the nanoreactor to allow localised resistive heating. When assembled together with the top die, it is possible to study the gas-material interactions from room temperature to 700 °C and pressures as high as 4.5 bar. The nanoreactor is introduced into the TEM using a specially designed specimen holder.[24,25] To determine a suitable experimental window for real *in situ* TEM corrosion studies, studies on compositional variation of Al alloys when exposed to chloride media for different time intervals are carried out. For this, analytical TEM techniques like local energy dispersive spectroscopy of X-rays (EDX), electron energy loss spectroscopy (EELS), and energy filtered TEM (EFTEM) for elemental mapping with 1 nm spatial resolution, by selectively imaging with electrons that have energies around specific ionisation edges have been used.[26]

2. Materials and Methods

2.1. Specimen Preparation

Commercial AA2024-T3 is used for the present study, which has a nominal composition (in weight %) of 3.8 – 4.9 Cu, 1.2 – 1.8 Mg, 0.3 – 0.9 Mn, 0.5 Si & Fe and minute quantities of chromium (Cr), zirconium (Zr) & titanium (Ti). The as-received samples are strips of thickness 0.8 mm that are mechanically polished to a foil of thickness 100 µm. Circular discs of 3 mm diameter, are punched from the foil and specimens for TEM investigation are prepared by electrochemical twinjet polishing using a Struers Tenupol 3 setup. The electrolyte used is a mixture of Nitric Acid (HNO_3, 69 %, Sigma Aldrich, ACS Grade) and Methanol (CH_3OH, ≥ 99.5 %, Sigma Aldrich, ACS Grade) in 1:3 ratio.

2.2. Corrosion experiments

The *ex-situ* corrosion experiments have been carried out by exposing the TEM specimens to two kinds of corrosive environments: 1 M NaCl solution (99.8%, VWR chemicals, diluted to 1 M concentration in de-ionised water); and a gas mixture (1:3 ratio) of O_2 and argon (Ar) bubbled through aq. HCl of pH=3. One specimen is immersed in a 1 M NaCl solution for a duration of 30 min, while three pairs of specimens are exposed to O_2 bubbled through aq. HCl of pH=3 for 20 min, 40 min and 60 min respectively.

2.3. TEM investigations

The TEM investigations have been carried out using a FEI Tecnai F20ST/STEM microscope (200 kV), equipped with a high resolution Gatan imaging filter (GIF) for EELS and EFTEM studies. Bright-field TEM (BF-TEM) and high angle annular dark-field (HAADF) STEM images are obtained at different stages of exposure to the reactive environment. A weak diffracting orientation of the sample is used to avoid strong dislocation contrast and to highlight the contrast of grain boundary precipitates (GB precipitates). Some areas of interest around grain boundaries and precipitates are identified and the corresponding EDX, EEL spectra and EFTEM elemental maps are obtained before and after exposing the specimen to the NaCl environment. In case of exposure to aq. HCl, TEM investigations are carried out on post-corroded specimens. The EFTEM elemental maps are obtained from a 20 eV slit around the O-K-edge (532 eV) for 20 s exposure and from a 30 eV slit around the Cu-$L_{2,3}$-edge (931 eV) for 40 s exposure. The background signal is subtracted for each map.

3. Results and Discussion

3.1. Unexposed specimens

Figure 4.1a shows a BF-TEM image obtained from a region containing a grain boundary triple-junction in an un-corroded AA2024-T3 specimen. The specimen has a large number of intermetallic precipitates, dark plate like features with a size ranging from 50-200 nm, inclined approximately 30° to the left with the vertical, and inclusions. Compositions of these precipitates are determined using EDX and classified based on size and composition into following three categories. (1) Large intermetallic inclusions with sizes typically in the range of 0.5 – 2 µm; some of which (~1-2 µm) are enriched with Fe, Mn and Si while other inclusions ~0.5 (±0.1) µm are identified as the θ-phase ($CuAl_2$) precipitates. The inclusion marked “b” in Figure 4.1a is identified as θ-phase, $CuAl_2$, identified by EDX, Figure 4.1b. These inclusions are usually found at the grain boundaries. (2) GB precipitates in the size range of 50 (±10) nm with nearly circular shape as indicated by the arrow in Figure 4.1a, are enriched with Cu and Mg, suggesting anodic S-phase type compositions. The compositions measured are (atom %) 90% Al, 6-7% Cu, 2% Mg and less than 1% Mn, Si, identified as $Al_{10}(Cu,Mg)$ type precipitates by Boag *et al.*[3] (3) Rod shaped precipitates in the matrix; with a width around 50 (±10) nm and length varying from 80 to 300 nm. These precipitates are enriched with Al, Cu and Mn while a some of them also contain Fe and Si, identified as $(Fe,Mn)_XSi(Al,Cu)_Y$ type precipitates.[23] Figure 4.1c shows the EDX spectrum obtained from a rod shaped matrix precipitate marked “c” in the Figure 4.1a, identified as $Al_{20}Cu_2Mn_3$ type precipitate.

3.2. Specimens exposed to 1 M NaCl for 30 min

Specimens are immersed in NaCl solution for 30 min and then rinsed in de-ionised water and methanol prior to TEM investigation. Figure 4.2a shows a region close to a hole, with deposits of a large number of dark nodular particles, indicated by arrows, ranging from a size of 10 to 125 (±10) nm. EDX confirms that these particles are Cu-rich remnant particles after de-alloying. Figure 4.2b shows BF-TEM image from another region of the same specimen containing a grain boundary, indicated by the top left arrow. In the high intensity areas of the matrix (in between the bending contours) some dark spots are observed, as indicated by the bottom arrow.

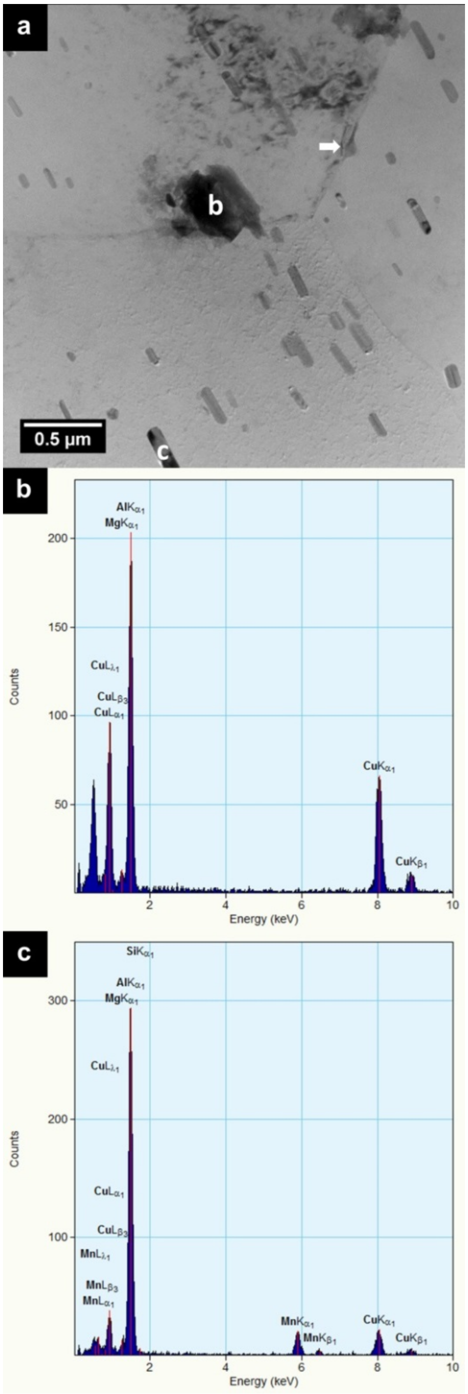

Figure 4.1: (a) BF-TEM image from a region containing a triple-junction and various kinds of intermetallic precipitates in an un-corroded AA2024-T3 specimen. EDX spot patterns obtained from: (b) θ-phase ($CuAl_2$) intermetallic marked "b" in Figure 4.1a; (c) $(Fe,Mn)_XSi(Al,Cu)_Y$ type precipitate, marked "c" in Figure 4.1a respectively.

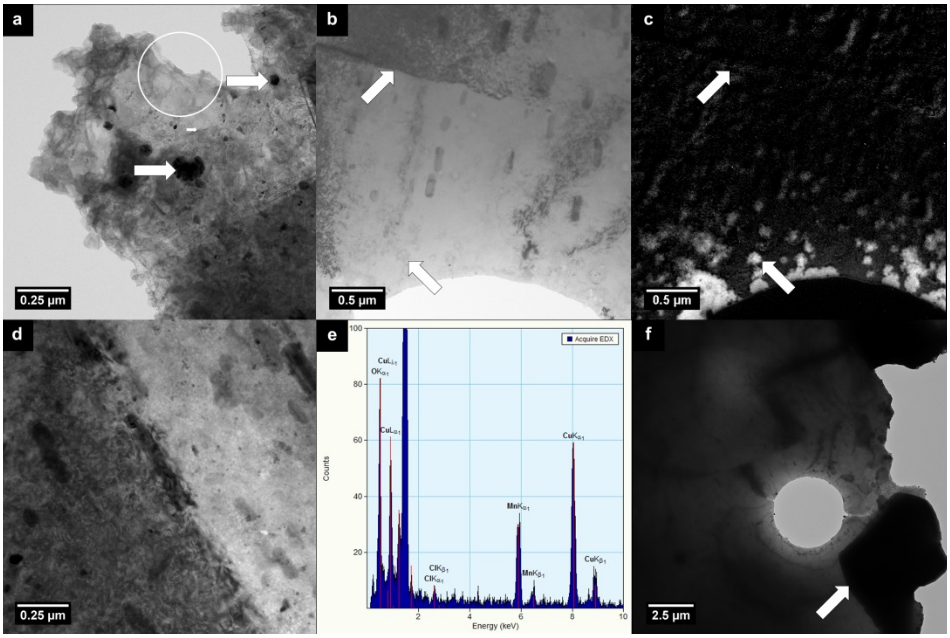

Figure 4.2: (a) BF-TEM image from a specimen immersed in 1 M NaCl for 30 min, the arrows indicate Cu-rich remnant particles after de-alloying. (b) BF-TEM image from another region of the same specimen, the arrow on the top indicates a grain boundary and the arrow close to the hole on the bottom shows surface attack. (c) Corresponding EFTEM map revealing the O-enrichment of the attacked areas and the arrow on the top shows O-depletion along the grain boundary. The rectangular region shows an area where the contrast is adjusted to make the oxide depletion more evident. (d) BF-TEM image and (e) corresponding EDX spectrum reveal the Cl^- attack at a grain boundary precipitate; the C peak is due to contamination during imaging or spectral acquisition. (f) An area covered with thick NaCl crystals, indicated by an arrow, make it difficult for TEM imaging.

EFTEM elemental map of the same region, Figure 4.2c, using O-K-edge reveals an O-enrichment on the sample surface, indicating the surface is attacked in NaCl environment. In addition, O-depletion is observed at the grain boundary, indicated by the top arrow in Figure 4.2c. This depletion is consistent with pitting due to Cl^- ions.[1] At this location, Cl is not detected by EDX but the precipitate in the centre of Figure 4.2d reveals a weak Cl peak as shown in Figure 4.2e. Figure 4.2f shows another region from the same specimen covered with NaCl crystal deposit, indicated by the arrow. Before exposing the specimen to NaCl environment, EDX and EEL-spectra are obtained from grain on the right, below the NaCl deposit. However, exposure to corrosive environment detaches the grain. Although localised corrosive attack is evident in NaCl environment, region under investigation in the specimen either dissolves or is covered with salt deposits, making it difficult to image in the TEM. Therefore these specimens are exposed to O_2 bubbled through aq. HCl of pH=3 to minimize such contamination.

3.3. Specimens exposed to aq. HCl for 20 min

Figure 4.3 shows BF-TEM and corresponding STEM-HAADF images from a specimen exposed to O_2 bubbled through aq. HCl for 20min. The locations marked by arrows in Figure 4.3a have a higher intensity than the neighbouring region in the BF-TEM image, suggesting that precipitates at these locations are removed in corrosive environment. This is confirmed by the STEM-HAADF image, Figure 4.3b, which shows less intensity at these locations compared to the matrix. This is interpreted as the formation of pits by the removal of GB precipitates during the exposure to the corrosive environment.

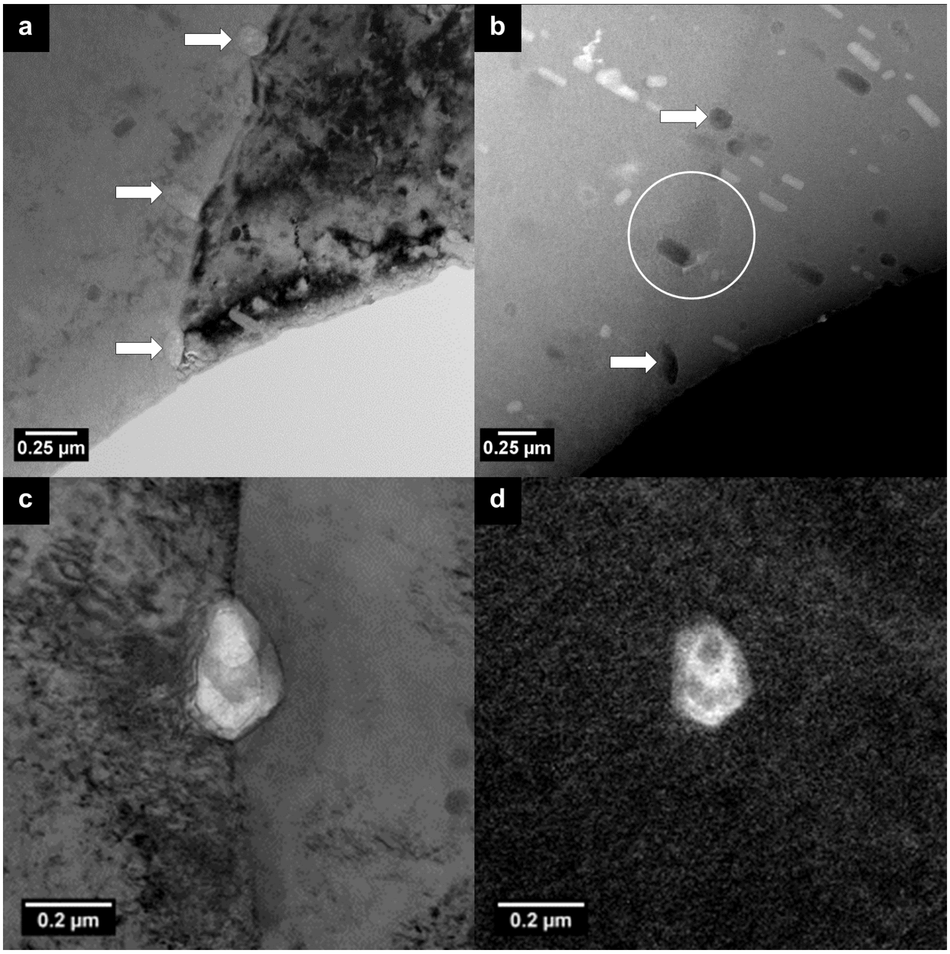

Figure 4.3: (a) BF-TEM image and the corresponding (b) DF- STEM images from a specimen exposed to O_2 bubbled through aq. HCl environment for duration of 20 min; the pits formed due to the removal of GB precipitates are indicated by the arrows and the encircled region shows the corrosion attack progressing in to the matrix close to the grain boundary. From another region in the same specimen: the BF-TEM image in (c) and the corresponding EFTEM O map in (d) show that the pit created by removal of a GB precipitate is enriched with O, suggesting the formation of O-rich corrosion product inside the pit.

The shape of the top and bottom pits is the same as the anodic $Cu_XAl_YMg_Z$ type precipitates observed in un-exposed specimens, Figure 4.1a. The pit in the encircled region in Figure 4.3b, adjacent to a ~400 nm dark spot is consistent with peripheral corrosion attack around a $(Fe,Mn)_XSi(Al,Cu)_Y$ or $Al_{20}Cu_2Mn_3$ type cathodic precipitate. Figure 4.3c shows another region from the same specimen, where a GB precipitate is removed. EFTEM elemental map from the O-K-edge, Figure 4.3d, shows O-enrichment inside the pit, interpreted as corrosion product in the pit. As there are no noticeable remnant clusters at this stage, it has not been possible to obtain EFTEM copper maps.

3.4. Specimens exposed to aq. HCl for 40 min

After exposing the specimens to corrosive environment for 40 min, two main features are observed: (1) severe corrosive attack at the former grain boundaries leads to the formation of a gap, and (2) deposits of dark nodular features, identified as Cu-rich remnants at several locations on the specimen surface. BF-TEM images and the corresponding EFTEM elemental maps from O-K-edge and $Cu\text{-}L_{2,3}$-edge obtained from two such regions are shown in Figure 4.4.

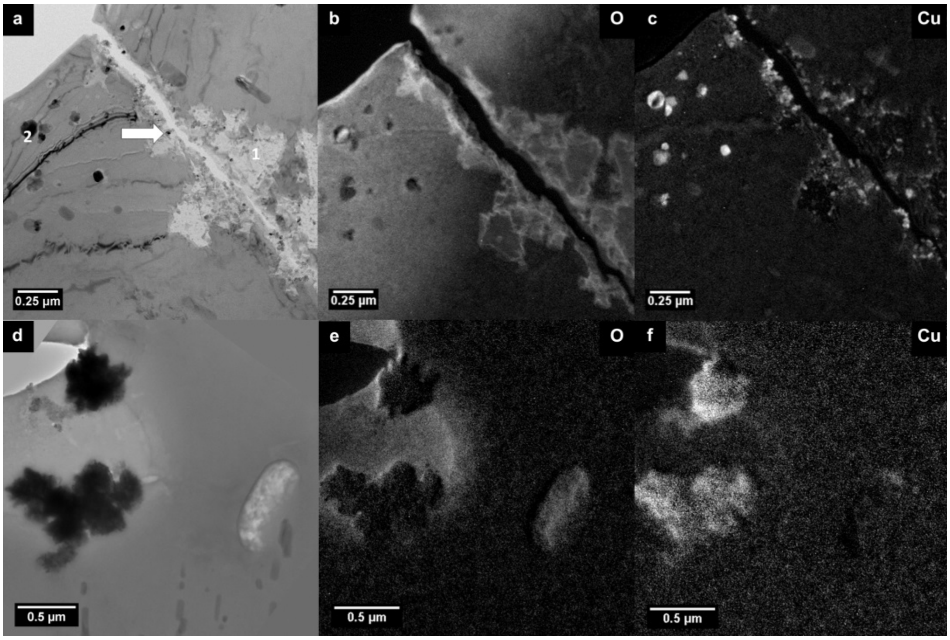

Figure 4.4: BF-TEM image and the corresponding EFTEM elemental maps using the O-K-edge and $Cu\text{-}L_{2,3}$*-edge from a specimen exposed to corrosive aq. HCl environment for duration of 40 min indicate: (a-c) intergranular attack and O-enrichment of the attacked regions while the dark nodular features deposited on the surface of the specimen are Cu-rich remnant particles as a result of de-alloying; (d-f) from another region of the same specimen, pit formed by the removal of ~1.5 µm sized intermetallic particle shows an O-enrichment in the pit while the dark deposits correspond to Cu-rich remnants as a result of de-alloying.*

Figure 4.4a shows the BF-TEM image from a region containing a gap formed due to the removal of material by corrosive attack. On tilting the specimen, the independent variations in contrast on the either side of the gap confirm that it is a former grain boundary. From the contrast variation in the BF-TEM image, location “1”, it appears that corrosive attack initiates at grain boundary and spreads into the neighbouring matrix regions. EFTEM maps, Figure 4.4b, reveal that the attacked regions shown by the higher intensity on both sides of the gap in Figure 4.4a are O-enriched. The dark nodular features, marked by the arrow in Figure 4.4a, ~20nm close to the gap, and the ones at location 2 (~80nm) are identified as copper-rich particles from EFTEM maps, Figure 4.4c. This is consistent with the formation of Cu-rich remnant particles due to de-alloying.

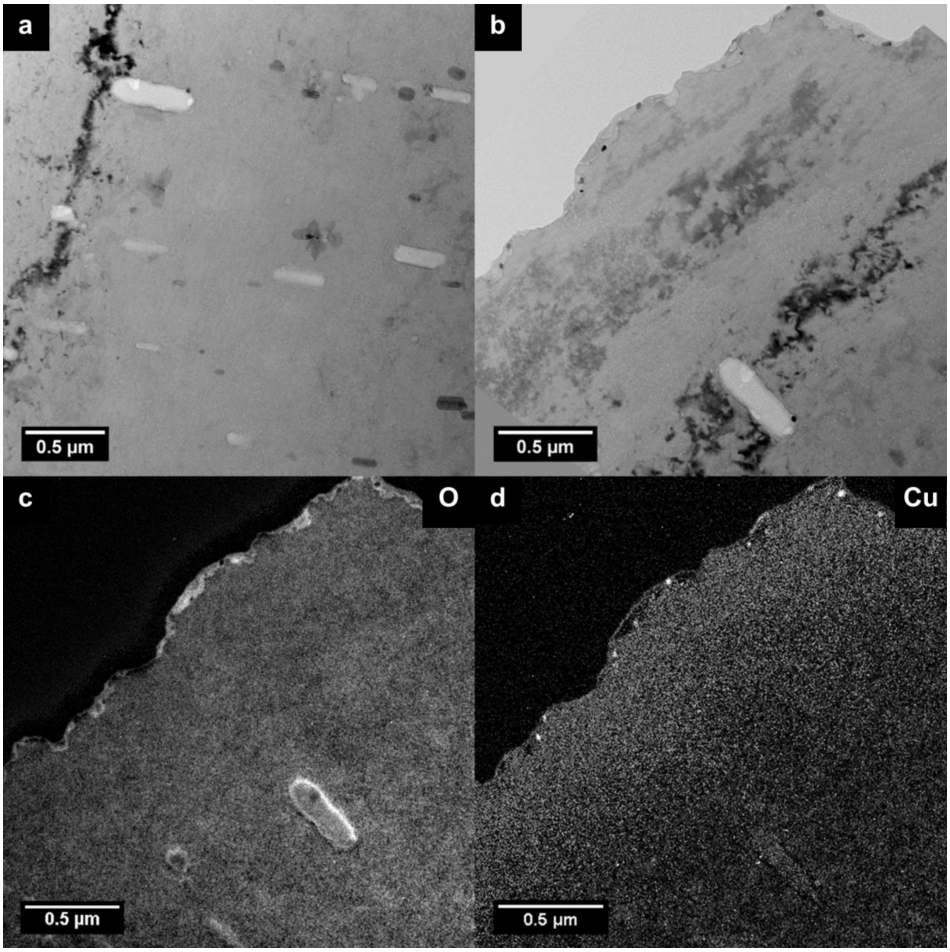

Figure 4.5: (a), (b) BF-TEM images from two specimen areas after prolonged exposures of 60 min to aq. HCl: note the local higher intensity due to the removal of matrix precipitates; (c-d) are the EFTEM elemental maps for oxygen and copper corresponding to the region shown in (b).

Another region from the same specimen, Figure 4.4d, shows a near circular pit with dark deposits at the edge, as a result of de-alloying of a former ~1.5 µm inclusion prior to corrosion. Also, pit formed by the removal of precipitate of length ~0.5 µm is observed at another location. EFTEM maps confirm that the pits are O-enriched, Figure 4.4e, while the deposits are Cu-rich remnants as a result of de-alloying.

3.5. Specimens exposed to aq. HCl for 60 min

For prolonged exposures (60 min) to the corrosive environment, it is observed that most matrix precipitates are removed, as indicated by the higher intensity BF-TEM images shown in Figure 4.5a and Figure 4.5b. The EFTEM elemental maps confirm that the pits are O-enriched and the tiny ~30 (±10) nm nodular features sticking to the edge of the specimen are Cu-rich remnant particles after de-alloying. However, the amount of copper clusters seems to be lower than that of 40 min exposure. This could be due to the reason that on prolonged exposure, corrosion attack is severe due to the Cu-redistribution[12-14] resulting in the detachment of the attacked grains as well as Cu-rich remnant particles.

3.6. Discussion

From the specimens exposed to the NaCl environment, it is evident that there is a formation of copper-rich remnant particles because of de-alloying, as well as an attack at the grain boundary by Cl^- ions. The O-depletion along the grain boundary from the EFTEM map, Figure 4.2c, and Cl signal from the EDX spectrum at a grain boundary precipitate, Figure 4.2e support this observation. However, considerable deposition of NaCl crystals on the region of interest makes it difficult to analyse the post-corroded specimens. To avoid the formation of NaCl crystals, the specimens have been exposed to oxygen bubbled through aq. HCl of pH=3, making it possible to follow the progress of localised corrosion.

After 20 min exposure, Figure 4.3, pits have formed at the location of former GB precipitates, while a few of the matrix precipitates are removed. Increased exposure to the corrosive environment, 40 min, results in intergranular corrosion, as observed from the BF-TEM image, Figure 4.4a, and the corrosion attack progresses to the neighbouring matrix, region 1 in Figure 4.4a. EFTEM maps show that the attacked regions are O-rich while the dark deposits throughout the specimen are Cu-rich remnants because of de-alloying. On prolonged exposure for 60 min to the reactive environment, most of the matrix precipitates are removed.

The localised corrosion attack mechanisms observed here on thin TEM samples are well in agreement with the recent observations from *ex situ* corrosion studies carried out using scanning electron microscopy (SEM) on AA2024-T3 in Cl^- media[9,10] and the existing models[13,19] in the literature that demonstrate the initiation of localised corrosion attack at intermetallic particles. Depending on whether the intermetallic particles are anodic or cathodic, the corrosion attack initiates by de-alloying of the anodic precipitate or by peripheral trenching around the cathodic type precipitates. Once the attack initiates, depending on the distribution of the precipitates, the attack propagates further by cooperative corrosion.[9,10] When there is a network of precipitates at the grain boundaries, the corrosion attack propagates further by an intergranular attack.

As these observations are made from different exposure times in different specimens, it is difficult to predict the exact moment of initiation of corrosive attack. Furthermore, when several morphological changes are observed at any given instance, like the removal of grain boundary precipitates, attack at the grain boundary as well as attack in the neighbouring matrix, it is difficult to predict the exact sequence in which the morphological changes have happened. In such cases, dynamic observation while the specimen is interacting with the corrosive environment is expected to yield new insights. Overall, these studies show that O_2 bubbled through aq. HCl serves as a good environment to visualize the important stages of localised corrosion on a nanoscale without interfering with the imaging process even for *in situ* TEM studies.

4. Conclusions

In the AA2024-T3 specimens used for the present study, three kinds of intermetallics have been identified and classified based on the size, composition and location.[18-20] On exposing these specimens to NaCl solution, de-alloying as well as attack at grain boundaries is observed. Deposition of NaCl crystals on the alloy surface makes it impossible to analyse the most corroded areas. Exposure to O_2 bubbled through aq. HCl of pH=3 for three different time durations reveals the following stages of localised corrosion:

1. After 20 min exposure, the pit formation at GB precipitates is observed.
2. After 40 min, the corrosion attack progresses along the grain boundaries (intergranular corrosion) in to the neighbouring matrix region along with the deposition of Cu-rich remnant particles.
3. After 60 min, most matrix precipitates are attacked.
4. EFTEM maps reveal that the remnant particles are enriched in Cu while the pits formed by removal of precipitates are enriched with oxygen.

These observations of corrosion of AA-2024T3 TEM samples are in agreement with those reported in the literature on bulk material of this alloy. Despite the fact that these observations are from different time intervals, it is difficult to predict the exact moment when the attack initiates at the nanoscale. *In situ* TEM experiments are expected to give insights into the initiation as well as the propagation of corrosion. The results presented demonstrate that O_2 bubbled through aq. HCl serves as a good electrolyte for *in situ* corrosion studies on TEM samples.

References

1 Foley, R. T. Localized corrosion of Aluminium Alloys - A Review. *Corrosion* **42**, 277-288 (1986).

2 Buchheit, R. G. A Compilation of Corrosion Potentials Reported for Intermetallic Phases in Aluminum Alloys. *Journal of The Electrochemical Society* **142**, 3994-3996 (1995).

3 Boag, A. *et al.* How complex is the microstructure of AA2024-T3? *Corrosion Science* **51**, 1565-1568 (2009).

4 Muller, I. L. & Galvele, J. R. Pitting potential of high purity binary aluminium alloys-I. Al-Cu alloys. Pitting and intergranular corrosion. *Corrosion Science* **17**, 179-193 (1977).

5 Muller, I. L. & Galvele, J. R. Pitting potential of high purity binary aluminium alloys-II. Al-Mg and Al-Zn alloys. *Corrosion Science* **17**, 995-1007 (1977).

6 Birbilis, N., Cavanaugh, M. K., Kovarik, L. & Buchheit, R. G. Nano-scale dissolution phenomena in Al–Cu–Mg alloys. *Electrochemistry Communications* **10**, 32-37 (2008).

7 Ralston, K. D. *et al.* Role of nanostructure in pitting of Al–Cu–Mg alloys. *Electrochimica Acta* **55**, 7834-7842 (2010).

8 Blanc, C., Freulon, A., Lafont, M.-C., Kihn, Y. & Mankowski, G. Modelling the corrosion behaviour of Al2CuMg coarse particles in copper-rich aluminium alloys. *Corrosion Science* **48**, 3838-3851 (2006).

9 Glenn, A. M. *et al.* Corrosion of AA2024-T3 Part III: Propagation. *Corrosion Science* **53**, 40-50 (2011).

10 Hughes, A. E. *et al.* Corrosion of AA2024-T3 Part II: Co-operative corrosion. *Corrosion Science* **53**, 27-39 (2011).

11 Boag, A., Hughes, A. E., Glenn, A. M., Muster, T. H. & McCulloch, D. Corrosion of AA2024-T3 Part I: Localised corrosion of isolated IM particles. *Corrosion Science* **53**, 17-26 (2011).

12 Lacroix, L., Ressier, L., Blanc, C. & Mankowski, G. Statistical Study of the Corrosion Behavior of Al2CuMg Intermetallics in AA2024-T351 by SKPFM. *Journal of The Electrochemical Society* **155**, C8-C15-C18-C15 (2008).

13 Lacroix, L., Ressier, L., Blanc, C. & Mankowski, G. Combination of AFM, SKPFM, and SIMS to Study the Corrosion Behavior of S-phase particles in AA2024-T351. *Journal of The Electrochemical Society* **155**, C131-C137-C131-C137 (2008).

14 Vukmirovic, M. B., Dimitrov, N. & Sieradzki, K. Dealloying and corrosion of Al alloy 2024-T3. *Journal of The Electrochemical Society* **149**, B428-B439, doi:Doi 10.1149/1.1498258 (2002).

15 Guillaumin, V. & Mankowski, G. Localized corrosion of 2024 T351 aluminium alloy in chloride media. *Corrosion Science* **41**, 421-438 (1999).

16 Schmutz, P. & Frankel, G. S. Corrosion Study of AA2024-T3 by Scanning Kelvin Probe Force Microscopy and *In situ* Atomic Force Microscopy Scratching. *Journal of The Electrochemical Society* **145**, 2295-2306 (1998).

17 Kowal, K., DeLuccia, J., Josefowicz, J. Y., Laird, C. & Farrington, G. C. *In situ* Atomic Force Microscopy Observations of the Corrosion Behavior of Aluminum-Copper Alloys. *Journal of The Electrochemical Society* **143**, 2471-2481 (1996).

18 Blanc, C., Lavelle, B. & Mankowski, G. The role of precipitates enriched with copper on the susceptibility to pitting corrosion of the 2024 aluminium alloy. *Corrosion Science* **39**, 495-510 (1997).

19 Buchheit, R. G., Grant, R. P., Hlava, P. F., McKenzie, B. & Zender, G. L. Local Dissolution Phenomena Associated with S Phase (Al_2CuMg) Particles in Aluminum Alloy 2024-T3. *Journal of The Electrochemical Society* **144**, 2621-2628 (1997).

20 Wei, R., Liao, C.-M. & Gao, M. A transmission electron microscopy study of constituent-particle-induced corrosion in 7075-T6 and 2024-T3 aluminum alloys. *Metallurgical and Materials Transactions A* **29**, 1153-1160 (1998).

21 Sun, D. M. *et al.* *Ex situ* TEM observation of localized attack on AA 6061. *Materials and Corrosion* **61**, 105-110 (2010).

22 Larsen, M. H., Walmsley, J. C., Lunder, O., Mathiesen, R. H. & Nisancioglu, K. Intergranular Corrosion of Copper-Containing AA6xxx AlMgSi Aluminum Alloys. *Journal of The Electrochemical Society* **155**, C550-C556-C550-C556 (2008).

23 Gao, M., Feng, C. & Wei, R. An analytical electron microscopy study of constituent particles in commercial 7075-T6 and 2024-T3 alloys. *Metallurgical and Materials Transactions A* **29**, 1145-1151 (1998).

24 Creemer, J. F. *et al.* Atomic-scale electron microscopy at ambient pressure. *Ultramicroscopy* **108**, 993-998 (2008).

25 Yokosawa, T., Alan, T., Pandraud, G., Dam, B. & Zandbergen, H. In-situ TEM on (de)hydrogenation of Pd at 0.5–4.5 bar hydrogen pressure and 20–400°C. *Ultramicroscopy* **112**, 47-52 (2012).

26 Keast, V. J., Scott, A. J., Brydson, R., Williams, D. B. & Bruley, J. Electron energy-loss near-edge structure – a tool for the investigation of electronic structure on the nanometre scale. *Journal of Microscopy* **203**, 135-175 (2001).

Chapter 5 QUASI IN-SITU CORROSION STUDIES[*]

A quasi in situ method using a specially developed holder is presented to follow electrochemically induced microstructural changes on a nanometre scale using analytical transmission electron microscopy (TEM). By following a specific specimen area after repeated exposure to oxygen (O_2) bubbled through aqueous (aq.) hydrochloric acid (HCl) of pH=3, de-alloying of a grain-boundary precipitate (GB precipitate) of ~200 nm is observed by monitoring the changes in the electron energy loss spectroscopy (EELS) copper (Cu) $L_{2,3}$-edge and energy filtered TEM (EFTEM) elemental maps. These results, supporting the existing models of de-alloying of Cu rich precipitates in aluminium (Al) alloys, demonstrate the effectiveness of the quasi in situ specimen holder for analytical TEM studies of corrosion.

---

[*] Published as: Malladi SRK, Tichelaar FD, Xu Q, Wu MY, Terryn H, Mol JMC, Hannour F, Zandbergen HW. Quasi *in situ* analytical TEM to investigate electrochemically induced microstructural changes in alloys: AA2024-T3 as an example. Corrosion Science 2012. DOI: 10.1016/j.corsci.2012.12.006

1. Background

Al alloys have a complex microstructure comprised of several intermetallic precipitates and dispersoids which not only contribute to their enhanced mechanical properties,[1,2] but also make these alloys susceptible to localised corrosion.[3] Extensive electrochemical studies combined with surface analytical techniques have revealed that the high concentrations of alloying and impurity elements present in the intermetallic particles make them exhibit different electrochemical characteristics compared to the matrix.[4-13] The initial changes consist of a preferential removal of anodic elements like Al and magnesium (Mg) from intermetallics, leaving behind Cu enriched particles. Due to the galvanic coupling between the Cu-enriched particles and the surrounding matrix, the initial anodic behaviour changes into cathodic behaviour and a circumferential attack is observed around these Cu-rich clusters.[6-8] This phenomenon has been well understood on the micron scale, and recent studies in Al-Cu-Mg model alloys[14,15] and in AA7010[16] also demonstrate this behaviour at nanoscale intermetallic particles.

For the identification of corrosion products, TEM with energy dispersive spectroscopy of X-rays (EDX) has proven to be a useful tool, as shown on specimens prepared by ultramicrotomy after corrosion or by comparing TEM samples before and after electrochemical changes.[14-27] Micron sized Cu-rich remnants at de-alloyed Al-Cu-Mg particles in AA2024-T3 have been identified as elemental Cu with EDX and diffraction[17] or EELS in TEM.[20] Our *ex situ* TEM corrosion studies[28] show different stages from the initiation of localised corrosion attack at GB precipitates to propagation of the attack to generate cracks at grain boundaries. Present understanding of the corrosion mechanisms using TEM has been developed from *ex situ* corrosion studies where post-corroded specimens are analysed or the specimen investigated has to be taken out of the TEM specimen holder before and after exposing to a corrosive environment. In such cases, finding back the same area in the specimen can be challenging or even impossible.

Here we present an effective technique to follow the initial stages of electrochemically induced changes of an Al alloy surface by viewing the same location before and after repeated exposure to a corrosive chloride (Cl^-) environment, using a specially designed TEM holder to monitor the changes quasi *in situ*. The method adapted here is called "quasi *in situ*", because a specific specimen area monitored by TEM is exposed repeatedly to the corrosive environment outside the microscope, as compared to real *in situ* studies where the specimen is continuously exposed to a corrosive environment inside the microscope. The de-alloying of a 200 nm sized Cu-rich GB precipitate in AA2024-T3 is studied using TEM imaging, EDX, and EELS. EELS is used to determine the type of bonding of Cu near the precipitate, and EFTEM is used to map O and Cu distribution in the area of interest.

2. Materials and methods

The material used for the present study is AA2024-T3, containing Cu, Mg and manganese (Mn) as the major alloying elements. As-received samples are mechanically polished to a foil of thickness ~100 µm. Circular discs of 3 mm diameter are punched from the foil and specimens for TEM investigation are prepared by twin-jet polishing using a Streurs Tenupol 3 setup. The electrolyte used is a mixture of nitric acid (HNO_3) and methanol (CH_3OH) in a ratio of 1:3, maintained at -30 °C while a potential of 20 V is applied for electro polishing.

A single specimen is repeatedly exposed to a gas mixture of O_2 bubbled through aq. HCl of pH=3, prepared from 37% HCl of Sigma-Aldrich, ACS grade, in deionised water. The cumulative exposure times for the specimen are 2, 6, 12, 20, 30, 42, 56 and 86 minutes, and at every intermediate stage, TEM investigations are carried out. The same specimen area is easily followed by using a double-tilt specimen holder developed in-house, in which a cartridge containing the TEM specimen is slid in, Figure 5.1a. While exposing the specimen to the corrosive environment, the specimen along with the cartridge is placed in a cartridge holder and slid into a glass tube with inlet and outlet, as shown in Figure 5.1b. For the present study, O_2 is bubbled through aq. HCl of pH=3 at a constant flow rate of 50 ml/min.

The TEM investigations are carried out using a FEI Tecnai F20ST/STEM microscope (200kV), equipped with a high resolution Gatan imaging filter (GIF) for EELS and EFTEM studies. EDX-spectra, EEL-spectra and EFTEM elemental maps are obtained from the same location before and after exposure to the corrosive environment. A 20-30 nm beam size is used for EDX and EELS collection causing some local carbon deposition, visible in Figure 5.2a above numbers "2" and "3". The EEL-spectra for the O-K-edge at 532 eV and Cu-$L_{2,3}$-edge at 931 eV are obtained after each exposure with an energy resolution of 0.6 eV and energy dispersion of 0.1 eV/pixel. The intensity scale is normalised for each spectrum whilst assuming the same background signal before and after corrosion, (i.e. the effective thickness is the same). The EELS data is refined using a low-pass smoothing filter over a window of 1 eV. The corresponding EFTEM elemental maps are obtained from a 20 eV slit around the O-K-edge for 20 s exposure and from a 30 eV slit around the Cu-$L_{2,3}$-edge for 40 s exposure. The background signal is subtracted for each map.

3. Results and Discussion

In the present study, we limit our discussion to the initiation of corrosion attack at a ~200 nm size Cu-rich intermetallic particle at a grain boundary, by monitoring the changes at several intermediate stages quasi *in situ*. Mainly three kinds of intermetallics have been identified in the specimen, classified based on size and composition.[28] In all matrix precipitates, an enrichment of Mn and Cu with respect to the matrix is detected with EDX, consistent with the rod shaped Al-Mn-Cu precipitates reported in the literature.[5] Some of the GB precipitates are enriched in Mg indicating S-phase type compositions.

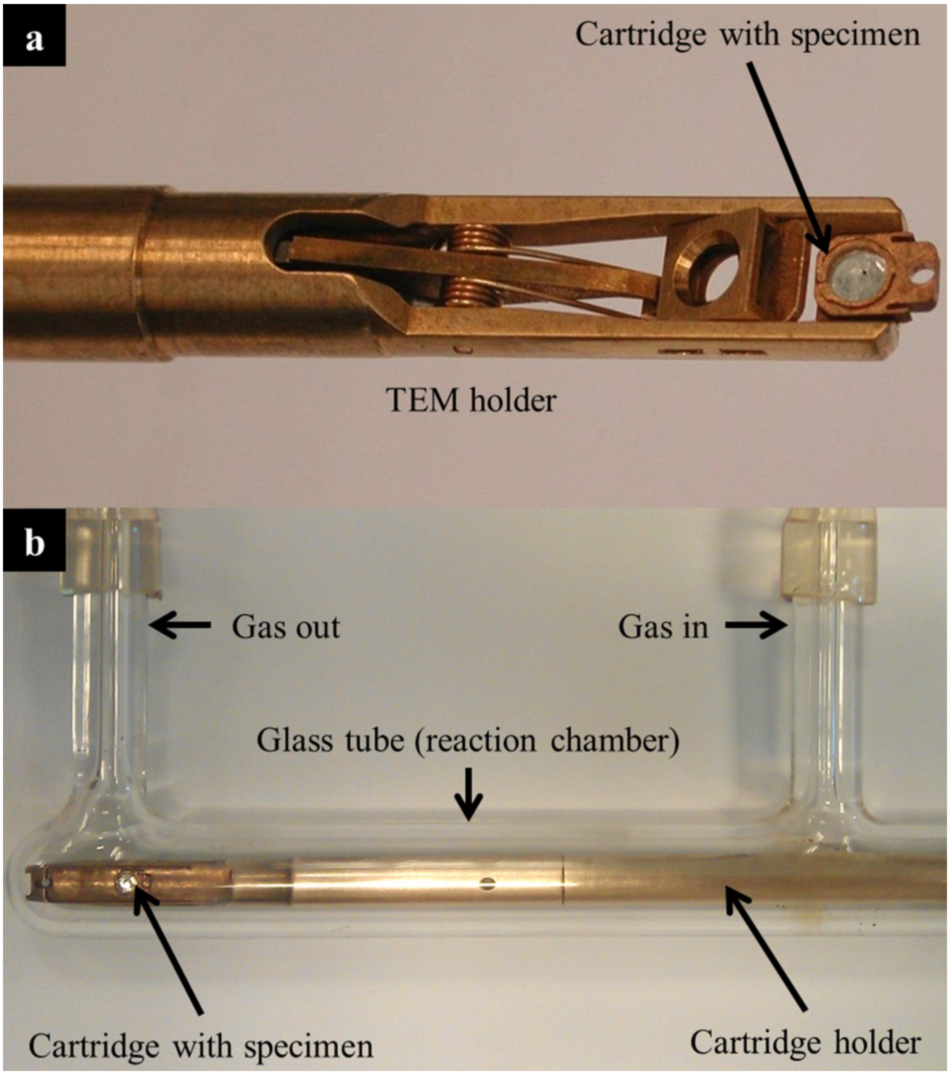

Figure 5.1: (a) Photograph showing the quasi in situ TEM specimen holder developed in-house; as the TEM specimen is fixed in the cartridge, it is possible to carry out quasi in situ studies and yet retain the same location as well as the orientation. (b) Photograph showing part of the experimental setup used for the exposure to corrosive environments; the cartridge with the specimen is positioned in the phosphor-bronze cartridge holder and is inserted into the glass tube consisting of an inlet and an outlet which allows the possibility to flow a reactive gas-vapour mixture.

One of the specimen areas containing a grain boundary and several precipitates, of which one is at the grain boundary, is monitored for changes during the quasi *in situ* study. At each of the intermediate stages using the *quasi in situ* holder, EFTEM maps, EELS and EDX spectra are obtained and the stages with significant changes are discussed here. At the intermediate stages of 2,6,12 and 20 min, the EEL-spectra and EFTEM elemental maps for O and Cu are quite similar to each other. Hence only the results obtained after 20 min and 30 min exposure are presented here. The bright-field TEM (BF-TEM) images and the corresponding EFTEM elemental maps for O and Cu are shown in Figure 5.2.

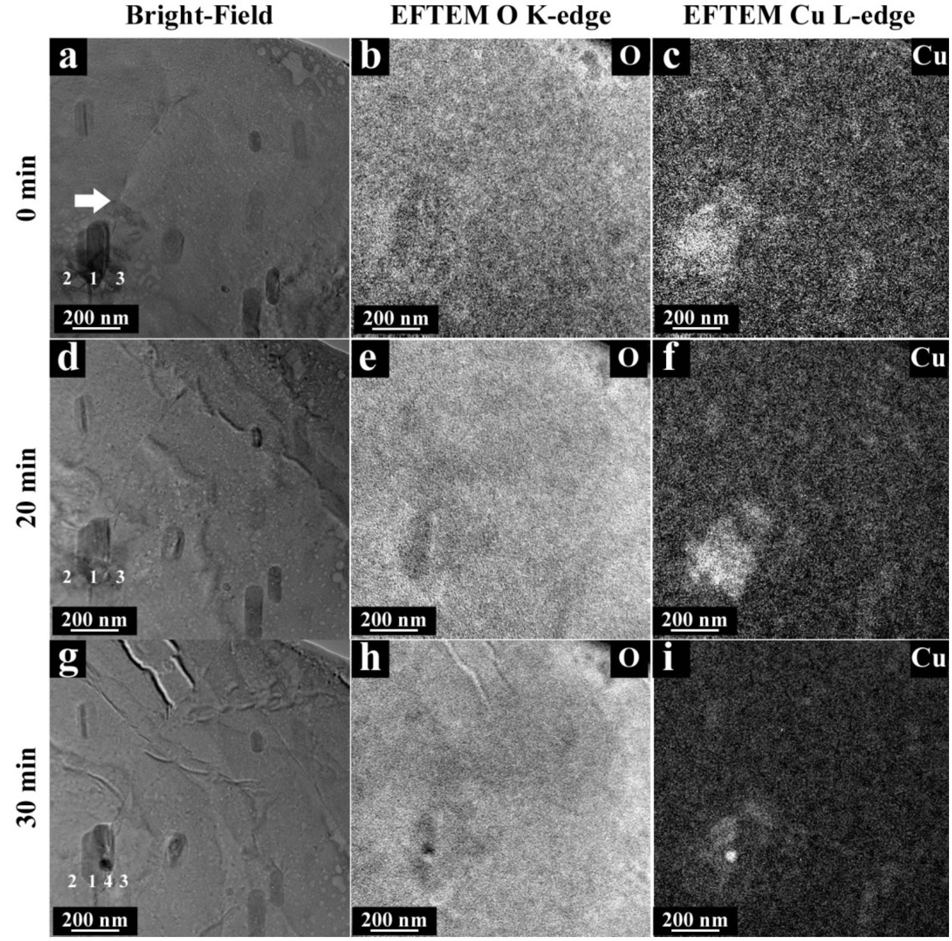

Figure 5.2: At each total time of exposure to the chloride and water rich gas, BF-TEM images, O and Cu EFTEM maps are shown from the area of interest. In (a) the grain boundary is indicated by the arrow, and the GB precipitate is numbered as 1. The numbers in the BF-TEM images refer to the positions for EELS and EDX measurements. On comparing the BF-TEM images (a, g, h) the only significant change is the formation of a nodular feature marked as 4 in (g). Over the location of the GB precipitate 1, the EFTEM O maps (b, e, h) show depletion with respect to the surrounding matrix while the overall intensity of the O maps has increased from un-exposed condition to 30 min exposure. The EFTEM Cu maps (c, f, i) show that the precipitates are generally enriched with Cu while (i) shows the nodular feature marked as 4 in (g) is enriched with Cu.

The grain boundary is marked with an arrow in Figure 5.2a. The GB precipitate under investigation is located below this arrow. EDX and EEL-spectra are obtained at different stages of exposure to the reactive environment using a 20-30 nm probe, positioned ~40 nm above the numbers in Figure 5.2a, Figure 5.2d and Figure 5.2g respectively. Before exposing the specimen to the corrosive environment, the EDX signal from the GB precipitate at location 1 in Figure 5.2a showed an approximate composition of Al 85%, Mn 5%, Cu 9% and Si 1%, suggesting an Al-Cu-Mn-Si type intermetallic particle.[2,18] The EFTEM O-map, Figure 5.2b, shows a lower intensity at the GB precipitate, indicating a depletion of the native protective oxide layer on the TEM foil surface at this precipitate, making it prone to de-alloying when exposed to the corrosive environment. The EFTEM Cu-map before exposure, Figure 5.2c, has a low signal-noise ratio, but shows enrichment of Cu at the location of the GB precipitate. In addition, some areas around the GB precipitate show some Cu-enrichment, probably caused by re-deposition in the electropolishing process during the specimen preparation.

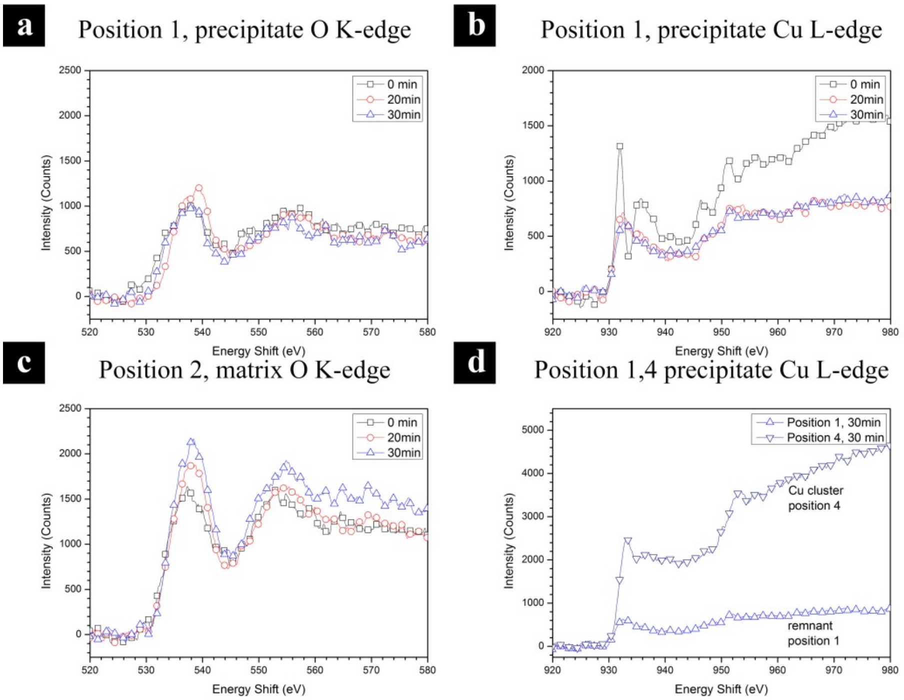

Figure 5.3: EELS O K-edges and Cu $L_{2,3}$-edges at different intermediate stages of exposure to the Cl^-/O_2 environment. The edges are obtained using a 20-30 nm probe, positioned ~40 nm above the numbers in Figure 5.2a, Figure 5.2d and Figure 5.2g. The symbols indicate the total exposure time. At position 1, not much change in the EELS O K-edge (a) from the precipitate is observed while the EELS Cu $L_{2,3}$-edge (b) shows a transformation from a sharp peak at 0-min, known as white line, to a broader peak with increasing exposure time to the corrosive environment. The EELS O K-edge at position 2 (c) shows O-enrichment in the matrix with increasing exposure time. The shape of the EELS Cu $L_{2,3}$-edge (d) from position 4, suggests the Cu-enrichment of the cluster.

After 20 min exposure to the corrosive environment the BF-TEM image, Figure 5.2d, and the EFTEM Cu-map, Figure 5.2f, have not changed much, but the EFTEM O-map, Figure 5.2e, shows a brighter intensity (except at the precipitate) as a result of an increased oxide layer thickness. After 30 min exposure to the corrosive environment, the most noticeable morphological change, a dark ~30 nm nodular feature at the GB precipitate at location 4 in Figure 5.2g, is observed. This is identified as a Cu-rich cluster from EDX spectra and the EFTEM elemental map, Figure 5.2i.

A number of EEL-spectra, Figure 5.3, from specific locations numbered 1-4 in Figure 5.2, reveal more aspects of the structural changes caused by the exposure to the corrosive environment. The EELS O K-edge, Figure 5.3a, obtained from location 1 on the GB precipitate does not change much with exposure. The Cu $L_{2,3}$-edge obtained from position 1 on the GB precipitate at 0 minutes, Figure 5.3b, shows a sharp peak, a so-called *white line*, indicating that Cu 3d states are empty due to alloying.[29] This shows that before exposing to the corrosive environment, Cu is bound to the other alloying elements in the precipitate. After 20 min and 30 min exposure, this EELS Cu $L_{2,3}$-edge appears to broaden and shift slightly to the right as compared to the initial condition indicating a transformation of Cu from a bound state in the GB precipitate to elemental Cu.[29,30] At position 2, in the matrix next to the GB precipitate, the EELS O K-edge shows a growth in the oxide layer with exposure time, Figure 5.3c. This increase is also observed at matrix position 3, and is consistent with the increasing intensity in EFTEM O-map in Figure 5.2. At position 4 on the GB precipitate, the broad appearance of the strong EELS Cu $L_{2,3}$-edge, Figure 5.3d, confirms that the cluster on the GB precipitate observed in Figure 5.2 at 30 min is elemental Cu.

The initiation of the electrochemical attack at the GB precipitate is consistent with the fact that it is located near the surface, as expected from the O-depletion over the precipitate surface from the EFTEM maps in Figure 5.2. The foil thickness near the GB precipitate, from the projected grain-boundary width in a BF-TEM tilt series is 72(±8) nm while the length and the width of the GB precipitate are 270(±1) nm and 125(±1) nm respectively. Stereo high angle annular dark field (HAADF) images in scanning transmission electron microscopy (STEM) mode taken under different tilts of the precipitate (Figure 5.4a for one tilt), and the dimensions of the precipitate compared to the foil thickness indicate that this precipitate is extends to both surfaces of the thin TEM foil. EDX spectra obtained from location 1 of the GB precipitate, before and after 30 min exposure to the corrosive environment indicate a decrease in Al from 85 at% to 73 at%, and an increase in Mn from 5 at% to 9 at% as well as Cu from 9 at% to 12 at%. The decrease in the Al content and the increase in the Cu and Mn content indicate the precipitate has undergone de-alloying on exposure to the corrosive environment.

After a prolonged 86 min total exposure to the corrosive environment, the STEM-HAADF image, Figure 5.4a, shows a peripheral attack around the GB precipitate as indicated by the arrows, consistent with a cathodic behaviour resulting in a peripheral attack. Furthermore, very fine bright clusters ~ 4 nm size can be seen at the edge of the trenches in the matrix as indicated by the arrows in Figure 5.4a. The bright contrast suggests the presence of Cu clusters.

Based on the observations from this study, a conceptual sketch illustrating the mechanism of de-alloying is presented in Figure 5.4. Figure 5.4b illustrates the geometry of the specimen with the electron transparent region in light grey. Figure 5.4c illustrates the cross-section of the sample at the GB precipitate before and after the corrosion attack has initiated. The native protective oxide layer of 4-10 nm is depleted at the precipitates, making it prone to de-alloying when exposed to the corrosive environment. Therefore, from the EDX, EELS and EFTEM analysis, it can be concluded that the active elements like Al from the precipitate partly undergo de-alloying and elemental Cu is left behind as a ~30 nm sised particle on the surface, in agreement with the existing models[6-9,21] on the de-alloying of Cu-rich precipitates in Al-Cu alloys.

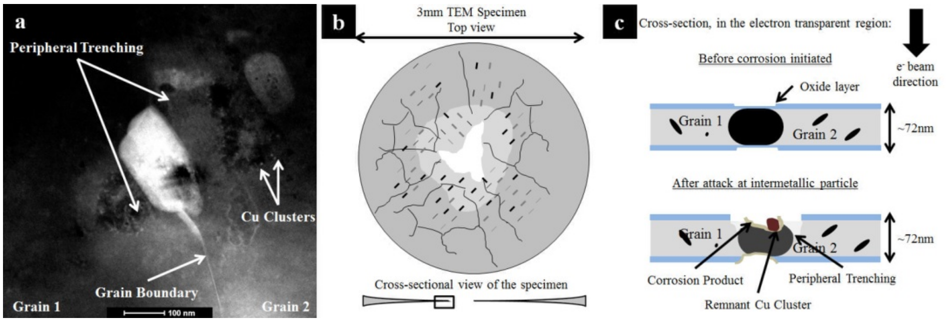

Figure 5.4: (a) STEM-HAADF image obtained after 86 min exposure to the corrosive environment from the region of localised corrosion attack. Notice the peripheral trenching around the GB precipitate and the remnant Cu clusters as a result of de-alloying as marked by the arrows. (b) Schematic illustrating top view as well as the cross-sectional view of the TEM specimen with intermetallic precipitates; the light grey areas close to the hole indicate the electron transparent region, also highlighted by the rectangle in the cross-sectional view. (c) Cross section through the GB precipitate in the electron transparent region similar to the configuration in Figure 5.2, before and after de-alloying in the corrosive environment

4. Conclusions

The initial electrochemically induced changes of Cu in a grain-boundary precipitate have been studied by monitoring the EELS Cu $L_{2,3}$-edge and EFTEM elemental maps in TEM after repeated exposure to a corrosive environment. This shows that Cu transforms from a bound state in the precipitate to elemental copper in a ~30 nm particle on the surface. The monitoring of this de-alloying process in small time-steps became possible by the use of a specially made quasi *in situ* TEM specimen holder that allows the study of the same TEM specimen area in the same orientation after repeated exposures to a corrosive environment outside the TEM.

References

1 Polmear, I. J. in *Light Alloys - From traditional alloys to nanocrystals* Ch. 2, 29-96 (Butterworth-Heinemann, 2006).

2 Boag, A. *et al.* How complex is the microstructure of AA2024-T3? *Corrosion Science* **51**, 1565-1568 (2009).

3 Foley, R. T. Localized corrosion of Aluminium Alloys - A Review. *Corrosion* **42**, 277-288 (1986).

4 Kowal, K., DeLuccia, J., Josefowicz, J. Y., Laird, C. & Farrington, G. C. In Situ Atomic Force Microscopy Observations of the Corrosion Behavior of Aluminum-Copper Alloys. *Journal of The Electrochemical Society* **143**, 2471-2481 (1996).

5 Guillaumin, V. & Mankowski, G. Localized corrosion of 2024 T351 aluminium alloy in chloride media. *Corrosion Science* **41**, 421-438 (1999).

6 Buchheit, R. G., Grant, R. P., Hlava, P. F., McKenzie, B. & Zender, G. L. Local Dissolution Phenomena Associated with S Phase (Al_2CuMg) Particles in Aluminum Alloy 2024-T3. *Journal of The Electrochemical Society* **144**, 2621-2628 (1997).

7 Vukmirovic, M. B., Dimitrov, N. & Sieradzki, K. Dealloying and corrosion of Al alloy 2024-T3. *Journal of The Electrochemical Society* **149**, B428-B439, doi:Doi 10.1149/1.1498258 (2002).

8 Lacroix, L., Ressier, L., Blanc, C. & Mankowski, G. Combination of AFM, SKPFM, and SIMS to Study the Corrosion Behavior of S-phase particles in AA2024-T351. *Journal of The Electrochemical Society* **155**, C131-C137 (2008).

9 Boag, A., Hughes, A. E., Glenn, A. M., Muster, T. H. & McCulloch, D. Corrosion of AA2024-T3 Part I: Localised corrosion of isolated IM particles. *Corrosion Science* **53**, 17-26 (2011).

10 Hughes, A. E. *et al.* Corrosion of AA2024-T3 Part II: Co-operative corrosion. *Corrosion Science* **53**, 27-39 (2011).

11 Glenn, A. M. *et al.* Corrosion of AA2024-T3 Part III: Propagation. *Corrosion Science* **53**, 40-50 (2011).

12 Boag, A. *et al.* Stable pit formation on AA2024-T3 in a NaCl environment. *Corrosion Science* **52**, 90-103 (2010).

13 Zhou, X., Luo, C., Hashimoto, T., Hughes, A. E. & Thompson, G. E. Study of localized corrosion in AA2024 aluminium alloy using electron tomography. *Corrosion Science* **58**, 299-306 (2012).

14 Birbilis, N., Cavanaugh, M. K., Kovarik, L. & Buchheit, R. G. Nano-scale dissolution phenomena in Al-Cu-Mg alloys. *Electrochemistry Communications* **10**, 32-37, doi:Doi 10.1016/J.Elecom.2007.10.032 (2008).

15 Ralston, K. D. *et al.* Role of nanostructure in pitting of Al-Cu-Mg alloys. *Electrochimica Acta* **55**, 7834-7842, doi:Doi 10.1016/J.Electacta.2010.02.001 (2010).

16 Wloka, J. & Virtanen, S. Detection of nanoscale eta-MgZn2 phase dissolution from an Al-Zn-Mg-Cu alloy by electrochemical microtransients. *Surface and Interface Analysis* **40**, 1219-1225, doi:Doi 10.1002/Sia.2868 (2008).

17 Wei, R., Liao, C.-M. & Gao, M. A transmission electron microscopy study of constituent-particle-induced corrosion in 7075-T6 and 2024-T3 aluminum alloys. *Metallurgical and Materials Transactions A* **29**, 1153-1160 (1998).

18 Gao, M., Feng, C. & Wei, R. An analytical electron microscopy study of constituent particles in commercial 7075-T6 and 2024-T3 alloys. *Metallurgical and Materials Transactions A* **29**, 1145-1151 (1998).

19 Boag, A. P. *et al.* Combined nuclear microprobe and TEM study of corrosion pit nucleation by intermetallics in aerospace aluminium alloys. *Nuclear Instruments and Methods in Physics Research Section B: Beam Interactions with Materials and Atoms* **231**, 457-462 (2005).

20 Blanc, C., Freulon, A., Lafont, M.-C., Kihn, Y. & Mankowski, G. Modelling the corrosion behaviour of Al2CuMg coarse particles in copper-rich aluminium alloys. *Corrosion Science* **48**, 3838-3851 (2006).

21 Svenningsen, G., Larsen, M. H., Walmsley, J. C., Nordlien, J. H. & Nisancioglu, K. Effect of artificial aging on intergranular corrosion of extruded AlMgSi alloy with small Cu content. *Corrosion Science* **48**, 1528-1543 (2006).

22 Zhao, Z. & Frankel, G. S. On the first breakdown in AA7075-T6. *Corrosion Science* **49**, 3064-3088 (2007).

23 Larsen, M. H., Walmsley, J. C., Lunder, O., Mathiesen, R. H. & Nisancioglu, K. Intergranular Corrosion of Copper-Containing AA6xxx AlMgSi Aluminum Alloys. *Journal of The Electrochemical Society* **155**, C550-C556-C550-C556 (2008).

24 Liu, Y. *et al.* Behaviour of copper during alkaline corrosion of Al-Cu alloys. *Corrosion Science* **50**, 1475-1480, doi:Doi 10.1016/J.Corsci.2008.01.021 (2008).

25 Curioni, M., de Miera, M. S., Skeldon, P., Thompson, G. E. & Ferguson, J. Macroscopic and local filming behavior of AA2024 T3 aluminum alloy during anodizing in sulfuric acid electrolyte. *Journal of The Electrochemical Society* **155**, C387-C395, doi:Doi 10.1149/1.2931522 (2008).

26 de Miera, M. S., Curioni, M., Skeldon, P. & Thompson, G. E. The behaviour of second phase particles during anodizing of aluminium alloys. *Corrosion Science* **52**, 2489-2497, doi:Doi 10.1016/J.Corsci.2010.03.029 (2010).

27 Sun, D. M. *et al.* Ex situ TEM observation of localized attack on AA 6061. *Materials and Corrosion* **61**, 105-110 (2010).

28 Malladi, S. R. K., Xu, Q., Tichelaar, F. D., Zandbergen, H. W., Hannour, F., Mol, J.M.C., Terryn, H. in *VI International Symposium on Aluminium Surface Science and Technology.*

29 Pearson, D. H., Ahn, C. C. & Fultz, B. Measurements of 3d occupancy from Cu $L_{\{2,3\}}$ electron-energy-loss spectra of rapidly quenched CuZr, CuTi, CuPd, CuPt, and CuAu. *Physical Review B* **50**, 12969-12972 (1994).

30 Leapman, R. D., Grunes, L. A. & Fejes, P. L. Study of the $L_{\{2,3\}}$ edges in the 3d transition metals and their oxides by electron-energy-loss spectroscopy with comparisons to theory. *Physical Review B* **26**, 614-614 (1982).

Chapter 6 IN-SITU CORROSION STUDIES[*]

An approach to carry out chemical reactions with aggressive gases in situ in a transmission electron microscope (TEM), at ambient pressures of 1.5 bar using a windowed environmental cell, called nanoreactor, is presented here. The nanoreactor coupled with a specially developed holder with platinum (Pt) tubing permits the usage of aggressive chemicals like hydrochloric acid (HCl).

---

[*] Published as: Malladi S, Shen C, Xu Q, de Kruijff T, Yücelen E, Tichelaar F, Zandbergen H. Localised corrosion in aluminium alloy 2024-T3 using *in situ* TEM. Chemical Communications 2013. DOI: 10.1039/C3CC46673F

1. Background

Environmental transmission electron microscopy (ETEM) is becoming an increasingly important field of study as the ability to create a controlled atmosphere around a specimen makes it possible to study several specimen-environment interactions on the nanoscale.[1] In a TEM, which is usually operated at ultra-high vacuum, the controlled environment is achieved by one of the following approaches:[2] the open type, using a differentially pumped vacuum system where the reactive gases are spread around the specimen area of the TEM; and the closed type, using a windowed environmental cell.[3] Over the years, the differentially pumped vacuum systems have proven to be very effective to achieve atomic resolution; however, the maximum achievable environmental pressures are in the order of 10 – 20 mbar. More recently, with the advancements in fabrication of microelectromechanical systems (MEMS) based devices; environmental cells based on silicon (Si) chips with thin membranes of Silicon Nitride (Si_XN_Y) have shown some intriguing possibilities for *in situ* experimentation.[3-7]

We have adopted the closed environmental cell based approach to facilitate the *in situ* ETEM studies. A functional MEMS device known as nanoreactor has been developed in-house for this. The nanoreactor consists of two facing chips fabricated with thin-film technology on a silicon substrate, as illustrated in Figure 6.1a. A Photograph showing both sides of the top and bottom chips as well as a glued nanoreactor is presented in Figure 6.1b. As seen in Figure 6.1b, the central area of the chip is etched to have a ~400 nm thin Si_XN_Y window which further consists of several ~20 nm thin Si_XN_Y membranes for electron transparency, as shown by the dark circles in the subsequent optical micrographs in Figure 6.1c-e. The top chip has ~200 nm spacers to prevent the stiction of the opposite membranes while the bottom chip consists of an embedded Pt wire to allow localised resistive heating to temperatures as high as 700 °C. After aligning and assembling the chips together, Figure 6.1e, it is possible to study a number of gas-material interactions by varying temperatures as well as pressures. Using this system, it is possible to study catalysis in a TEM as well as in scanning transmission X-ray microscopy (STXM)[5] and (de)hydrogenation of hydrogen storage materials[8] *in situ*.

The main advantage of the window cell approach over the differentially pumped vacuum system is that by confining to a small region around the specimen it is possible to achieve much higher environment pressures inside the microscope. It has been shown that it is possible to achieve atomic resolution[3,6] close to atmospheric pressure (0.18 nm at 500 °C and 1.2 bar hydrogen (H_2))[3] and even achieve pressures as high as 4.5 bar.[8] Furthermore, the added advantage of a windowed cell is the possibility to extend it to liquid systems.[9]

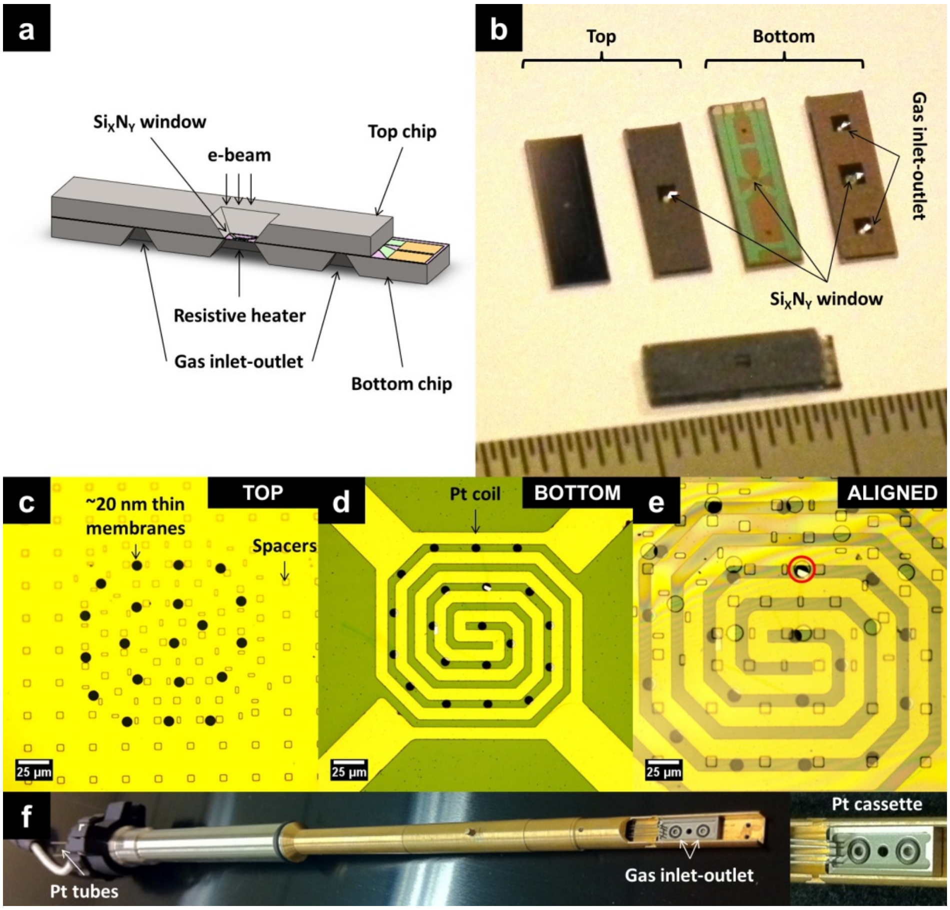

Figure 6.1: (a) Conceptual sketch of a nanoreactor; (b) Photographs of top and the bottom chip, with ~ 400 nm Si_XN_Y window in 800 X 800 µm^2 area; inlet and outlet for reactive gases in bottom chip. Optical micrographs of the 400 nm Si_XN_Y window showing (c) top and (d) bottom chips respectively with 10 µm circular holes over spanned with ~ 20 nm Si_XN_Y membranes for electron transparency. The bottom chip is embedded with a Pt spiral for heating. The red encircled region in (e) showing aligned assembly. A glued nanoreactor is introduced into the TEM with the holder made, shown in (f). The holder has Pt tubing and the tip consists of a Pt cassette.

2. Materials and Methods

The specimens used for this study have been prepared using an FEI Strata DB 235, dual-beam gallium (Ga) focused ion beam (FIB) - scanning electron microscope (SEM) operated at 30 kV. The as-received commercial aluminium (Al) alloy, AA2024-T3 samples are strips of dimensions 100 × 200 × 0.8 mm^3. The surface preparation before FIB milling is carried out by mechanically polishing smaller squares of 10 × 10 mm using P 320, 600, 1200, 2400, 4000 silicon carbide (SiC) papers in the order mentioned. The final polishing is carried out by using 0.05 µm colloidal alumina suspension.

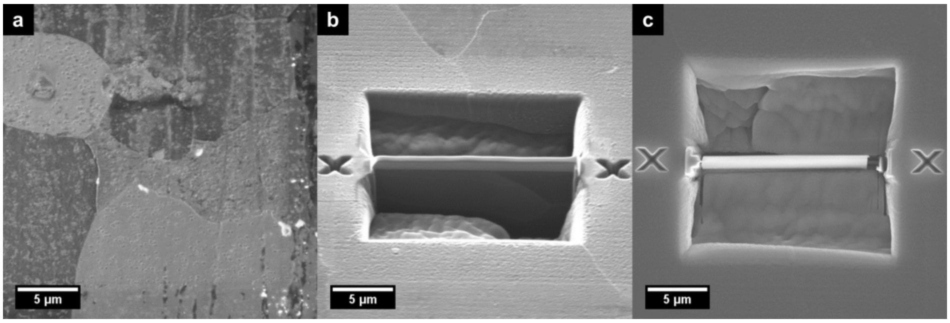

Figure 6.2: FIB secondary electron images of: (a) AA2024-T3 specimen revealing the grain boundaries after etching the surface layer by Ga ion milling; (b) an inclined image at 7° showing a cross-sectional FIB specimen, cut across a grain boundary, before final step of milling to thickness below 100 nm. (c) SEM image of the same FIB specimen after final thinning ≤ 100 nm thickness and releasing from the trench. This specimen is now ready for transfer.

The sample surface is then etched by focused Ga ion beam to reveal the grain boundaries, Figure 6.2a. The sample has an average grain size of 7 (±2) µm. As grain boundaries and precipitates are the locations where localised corrosion attack tends to initiate, cross-sectional specimens of dimensions 15 µm × 5 µm × 100 nm are cut across a grain boundary such that every TEM specimen has at least one grain boundary as shown in Figure 6.2b. After final thinning to thicknesses ≤ 100 nm, the specimen is cut at the edges and released from the trench, Figure 6.2c, and is ready for transfer. The specimen is transferred to the chip using an external micromanipulator with a glass capillary.

Figure 6.3a-c show the specimen lift-out and transfer onto the bottom chip of the nanoreactor. The TEM specimens stick to the glass capillary by electrostatic force and when transferred on to a chip, the contact force between the Si_XN_Y membrane and the specimen releases it from the needle and adheres to the surface. Metallic specimens can be transferred within ~ 2 µm accuracy at reasonably high success rates (at least three out of five specimens can be transferred successfully). The bottom half of the nanoreactor alone can be used for *in situ* heat-treatment experiments.[10,11] EDX mapping has been carried out on one such specimen in an FEI TITAN TEM equipped with ChemiSTEM™ technology (X-FEG, and Super-X detection system)[12] operated at 200 kV in scanning transmission electron microscopy (STEM) mode before assembling the nanoreactor. After a successful specimen transfer, the bottom chip is placed in an alignment tool with top chip above it. The alignment tool is constructed in such a way that the top chip can be moved within 3-5 µm accuracy. Once the thin membrane(s) on the bottom and the top chip coincide, the top chip is clamped down applying a gentle force such that the chips remain aligned before gluing. Water glass (sodium silicate) which has set-time of around 45 min to 1 hour is used to glue the chips together in order to avoid any hydrocarbon contamination from glues. Once glued, the nanoreactor is ready for *in situ* TEM studies.

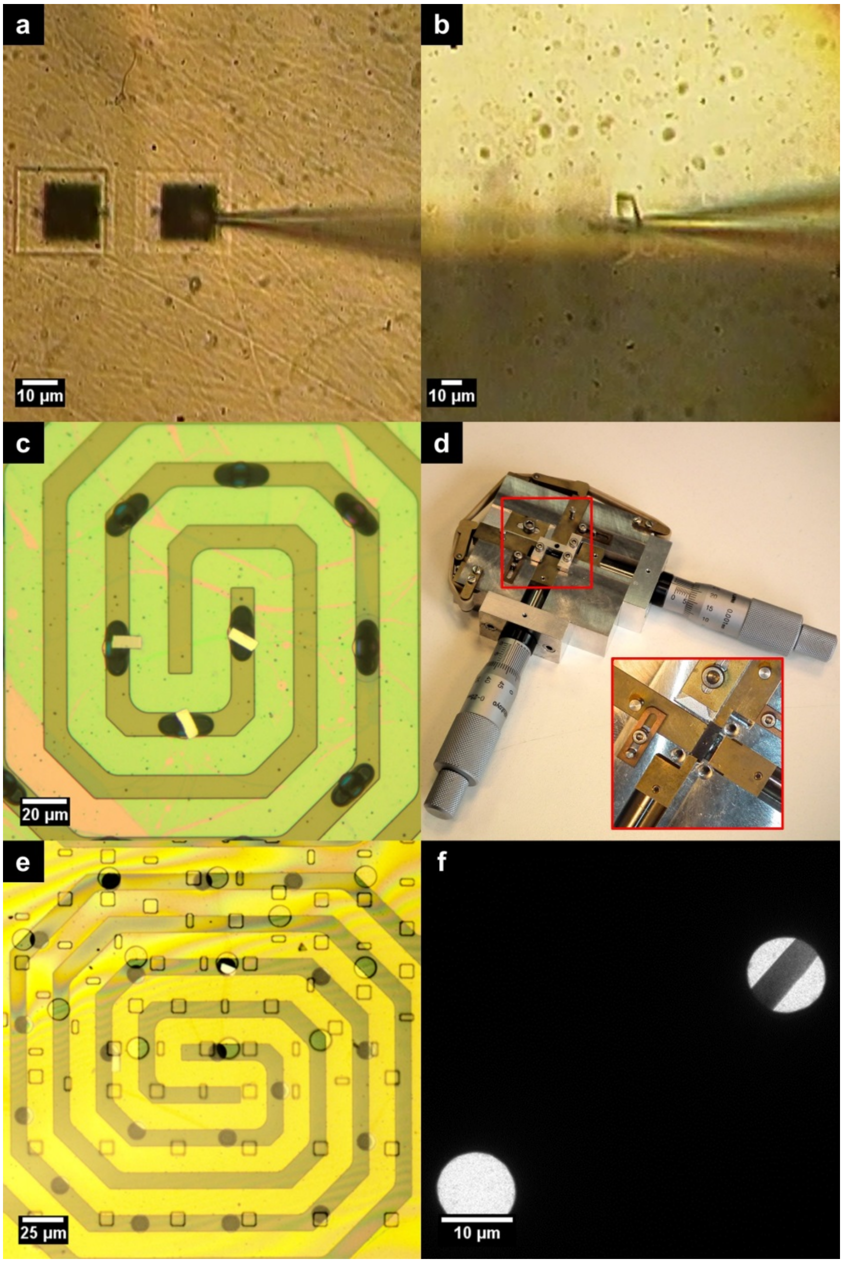

Figure 6.3: (a) Optical micrograph showing two FIB specimens in a trenches, about to be transferred using an external micromanipulator with a glass capillary. The specimen in the right cavity is being lifted out of the cavity with the sharp glass needle (visible at the middle of the image from the right side). (b) Specimen removed from the trench and attached to the glass needle. (c) Specimens on thin membranes of the bottom chip of a nanoreactor, after successful transfer. (d) Alignment tool for aligning the top and the bottom chips under an optical microscope. The inset shows a blow up of the central area, showing the sharp edges of phosphor-bronze plates attached to a calibrated screw allowing micrometre displacements. (e) Optical micrograph showing aligned thin membranes containing a specimen. (f) Low-magnification TEM image showing the specimen in an aligned nanoreactor.

The gas injection system for the *in situ* TEM studies is based on a simple gas cylinder bubbling through a reservoir containing the electrolyte, aqueous (aq.) HCl of pH = 3, with a flow meter regulating the pressure and volume of the gas. Photographs of the gas injection system are shown in Figure 6.4. Throughout the experiment a flow rate of 50 ml/min has been maintained. The *in situ* TEM experiments have been carried out on a Philips CM 30 T microscope operated at 200 kV.

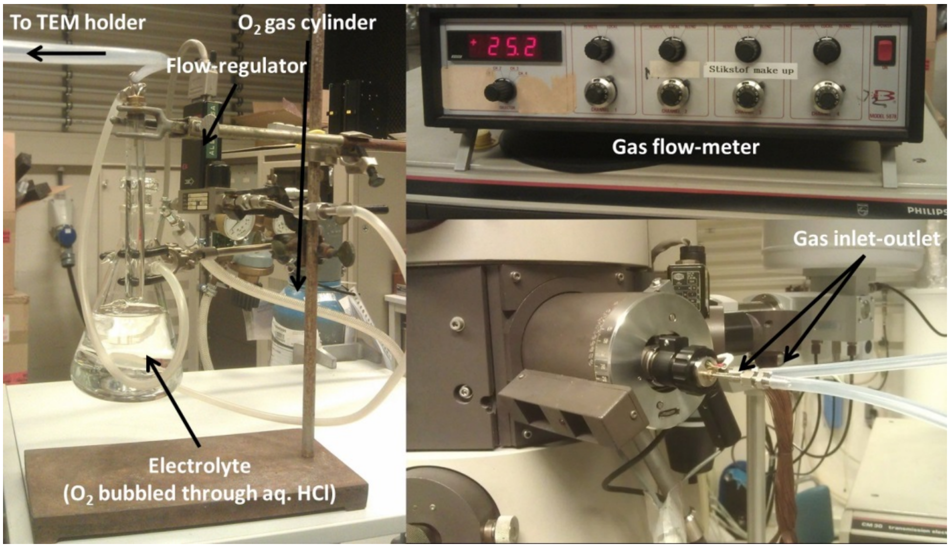

Figure 6.4: Photographs showing the experimental setup. The image on the left shows oxygen (O_2)-Argon (Ar) gas mixture (1:3 ratio) being bubbled through a flask containing aq. HCl of pH = 3. The gas coming out from the flask goes through another test-tube bubbler as a safety measure to prevent excess HCl entering the holder after topping up the flask. The volume of the gas flowing is regulated by a digital flow meter, connected in between the cylinder and the flask. For this experiment, a constant flow of 50 ml/min is maintained at a pressure of 1.5 bar. The image on the bottom right side shows the gas tubes connected to the holder inside the microscope.

3. Results and Discussion

The present study focuses on the application of nanoreactor to investigate localised corrosion in a well-studied Al alloy, AA2024-T3 in a liquid-gas environment of O_2 bubbled through aq. HCl of pH = 3 at ~ 1.5 bar pressure and room temperature. Compared with the earlier studies, here we have used a holder equipped with a Pt cassette and Pt exchangeable gas tubing, Figure 6.1(f), to allow aggressive gas mixtures. Prior to the *in situ* corrosion experiments, to understand the alloy microstructure and to optimise the experimental parameters pertaining to specimen preparation and the reaction environment, *ex situ*[13] as well as *quasi in situ*[14] corrosion experiments have been carried out. A common feature observed in Al alloys is the presence of numerous intermetallic precipitates and dispersoids and segregated regions like precipitate free zones close to the grain boundaries, which exhibit distinctly different electrochemical characteristics compared to the surrounding microstructure.[15] As a result, there are many localised nano-galvanic couples, which make these alloys susceptible to a spontaneous electrochemical attack.[16] Due to the localisation of a corrosive attack close to grain boundaries and precipitates, we have opted to carry out the *in situ* corrosion studies on specimens prepared by FIB as it is possible to selectively prepare cross-sectional specimens in the vicinity of grain boundaries. The ability to produce specimens in the same thickness range as well as the reliability to position the specimens accurately on the thin membranes of the nanoreactor is another reason for choosing this method. From the *ex situ* corrosion studies, depending on the morphology, location and compositional analysis from energy-dispersive X-ray spectroscopy (EDX), the intermetallic precipitates have been classified into three categories: (1) large intermetallics with sizes typically in the range of 0.5 – 2 µm, enriched with iron (Fe), manganese (Mn) and silicon (Si) as well as intermetallics of the order of 0.5 (±0.1) µm, identified as the θ-phase ($CuAl_2$) precipitates; (2) Grain boundary precipitates enriched with copper (Cu) and magnesium (Mg), suggesting a mixture of θ-phase and S-phase ($CuAl_2Mg$); (3) Plate type matrix precipitates with a width of 50 (±10) nm and length varying from 80 to 300 nm, mostly enriched with Cu and Mn, identified as $Al_{20}Mn_3Cu_2$ type precipitates, commonly observed at this heat treatment condition[17] in this alloy. Figure 6.5 shows a STEM - annular dark field (STEM-ADF) image obtained from an AA2024-T3 FIB specimen, revealing the plate type matrix precipitates.

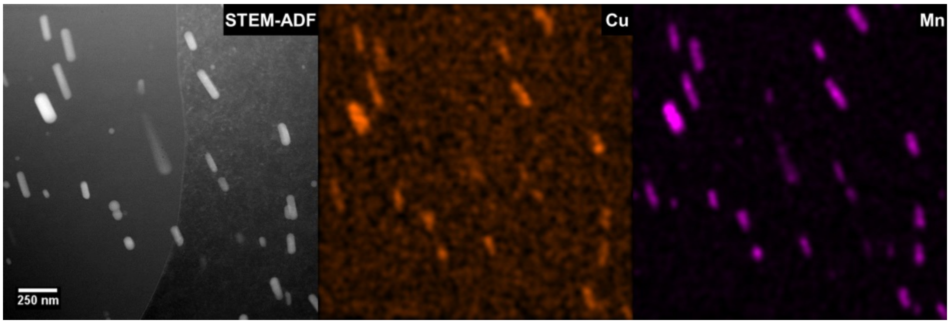

Figure 6.5: STEM-ADF image and the corresponding EDX elemental maps from a FIB specimen of AA2024-T3 reveal plate-like precipitates in the Al matrix enriched with Cu and Mn. These plate type precipitates have been identified as $Al_{20}Mn_3Cu_2$ type, which behave cathodic with respect to the matrix.

Although these precipitates are largely present in the matrix, occasionally they can be found at the grain boundaries too. Depending on the alloying elements present, the precipitates can broadly be categorised into one of these two types:[15-17] *anodic*, which are active compared to the matrix; and *cathodic*, which are more noble compared to the matrix. When the precipitates are cathodic, a circumferential attack is observed in the matrix.

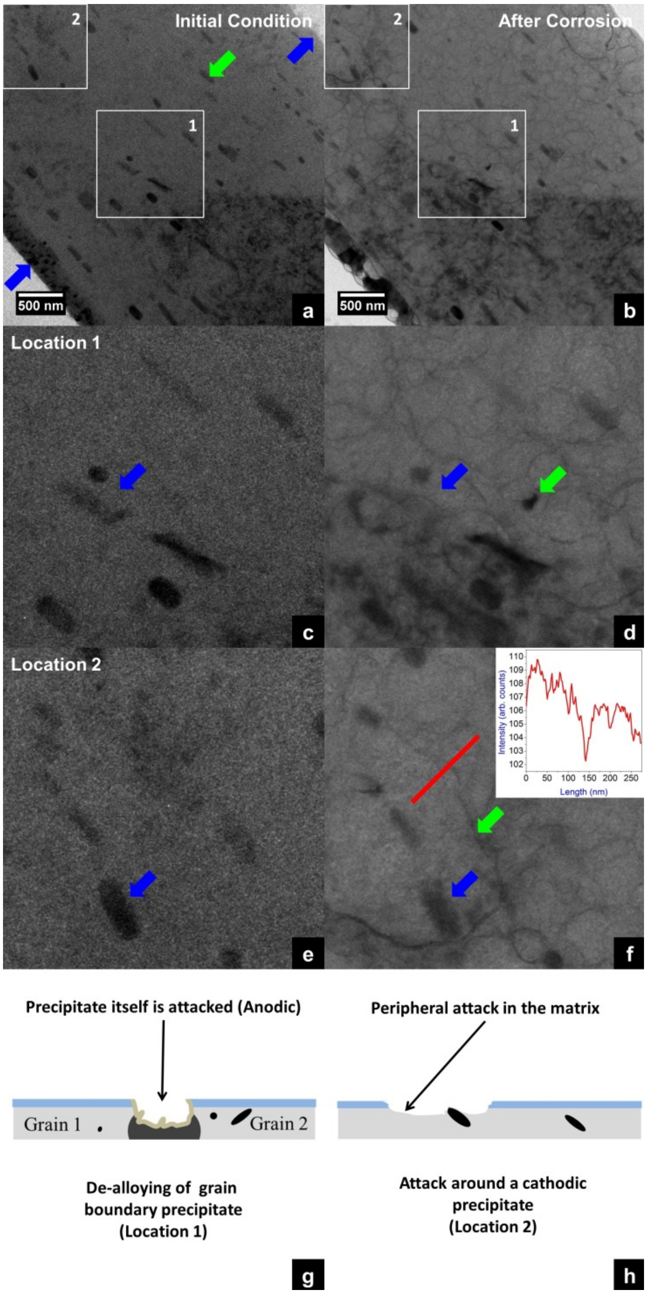

Figure 6.6: (a, b) BF-TEM images obtained from AA2024-T3 FIB specimen before and after in situ corrosion at room temperature and 1.5 bar pressure. The artefacts during specimen preparation are indicated by blue arrows. (c, d) At location 1 a grain-boundary precipitate (shown by blue arrow) is removed by de-alloying. Also the appearance of a dark feature (green arrow) close to the grain boundary precipitate is observed. (e, f) At location 2, the matrix surface around one of the precipitates (blue arrow) is attacked. An intensity profile along a 275 nm line (red) across the attacked region shows a higher intensity close to the precipitate as compared to that of the matrix beyond the dark contour (shown by green arrow). (g, h) schematics illustrating the corrosive attack.

On the other hand, when the precipitate is anodic, selective dissolution of the intermetallic particle itself occurs, as observed from the *quasi in situ* corrosion studies.[14] From the *ex situ* and *quasi in situ* corrosion studies, it has been decided to carry out *in situ* corrosion experiments at room temperature in an environment of O_2 bubbled through aq. HCl of pH = 3 at ~ 1.5 bar pressure.

Figure 6.6 shows the results from *in situ* corrosion studies just before and after exposing AA2024-T3 FIB specimen to the electrolyte of oxygen bubbled through aq. HCl for duration of approximately 5 hours. During the experiment, movies have been recorded using a CCD camera in bright-field (BF-TEM) mode. Figure 6.6a shows the entire cross-section of a diagonally positioned FIB lamella before injecting the reactive gas mixture into the nanoreactor. The dark plate like features along the diagonal direction (indicated by green arrow), ranging from 70 - 400 nm in length and 30 - 100 nm in width are the intermetallic precipitates. The dark band (indicated by blue arrow) ~ 300 nm in width at the bottom left corner of the image is an artefact, re-deposited material at the bottom of the trench during specimen preparation, which can in principle be minimised by low-voltage ion milling for future studies. The Supplementary Movie S6.1 shows the progression of the *in situ* study from the moment reactive gas mixture is introduced into the nanoreactor.

At the very beginning, several circular features (droplets of aq. HCl) are observed all over the specimen surface (images in the supplementary information). Until ~ 1 hour, changes at edges of the specimen, corresponding to the blue and green arrows in Figure 6.6a and migration of the HCl droplets are observed. For the next 2 hours, some diffraction contrast change due to an orientation change of ~ 0.1° is observed close to the grain boundary precipitate (location 1); however no significant morphological changes are observed. After 3 hours, the HCl reservoir is refilled and the HCl droplets re-appear (images in supplementary information). It is from this point that significant microstructural changes are observed. From here on, the dark contrast of the grain boundary precipitate at location 1 appears to diminish. This change is evident at the end of 5 hours exposure in Figure 6.6b, magnified images of location 1 in Figure 6.6c&d. This has been interpreted as de-alloying of the precipitate, indicating an anodic behaviour. The presence of anodic precipitates at grain boundaries in other specimens of the same alloy has been reported in our *ex situ* corrosion studies also.[13]

In the region surrounding plate-like precipitates in the matrix (identified as $Al_{20}Mn_3Cu_2$ type in other specimens from the same alloy), after nearly 4 hours of exposure, the growth of a region with brighter contrast bounded by a dark boundary is observed, Figure 6.6(f). This is interpreted as a result of a surface corrosive attack of the Al matrix. Furthermore, significant etching of the Al matrix is observed all over the specimen surface.

An important aspect to be considered here is the influence of the electron beam. The electron beam could induce a negative charge on the Al specimen surface, an effect similar to cathodic polarisation, which can cause a resistance to corrosive attack, on the other hand, it could also dissociate HCl to its respective ions, resulting in making Al susceptible to corrosion by Cl^- which is well documented.[17] These two counterbalancing effects under the electron beam cannot be distinguished in this particular study but calls for more experiments in this direction. Nonetheless, the corrosion attack observed here is consistent with localised corrosion studies in Al alloys[16,17] and based on these, conceptual sketches illustrating the corrosive attack around an anodic and a cathodic precipitate are presented in Figure 6.6g&h.

4. Conclusion

In this study, we have demonstrated an *in situ* approach to investigate corrosion reactions on a sub-micron scale. Although the exact 3D location of the precipitates across the cross-section is unclear from the BF-TEM images, as corrosion is a surface reaction, it is interpreted that the precipitates that have been attacked at locations 1 and 2 are closer to the surface. In future experiments, this geometrical question can be answered by performing tomography before and after the *in situ* study. The silicon nitride membranes (~ 20 nm thick) of the nanoreactor withstand the pressures of ~ 1.5 bar throughout the experiment for 5 hours of constant electron beam illumination and flow of highly reactive gas mixtures (combination of HCl, H_2O and O_2), without any noticeable reaction or damage. Despite this stability, it is better to speed up the corrosion process to make a more efficient use of the TEM, which can be obtained by carrying out corrosion tests at higher temperatures using the heater. Also, it is possible to combine the morphological changes during heat treatment to the corrosion behaviour of Al alloys. In short, this approach opens up possibilities to investigate morphological changes during chemical reactions in various gas-liquid-material systems on nanoscale.

References

1 Gai, P. L., Sharma, R. & Ross, F. M. Environmental (S)TEM Studies of Gas–Liquid–Solid Interactions under Reaction Conditions. *MRS Bulletin* **33**, 107-114, doi:10.1557/mrs2008.23 (2008).

2 Butler, E. P. & Hale, K. F. in *Practical Methods in Electron Microscopy* Vol. 9 (ed M. Glauert) Ch. 5, 239-308 (Elsevier Science Ltd 1981).

3 Creemer, J. F. *et al.* Atomic-scale electron microscopy at ambient pressure. *Ultramicroscopy* **108**, 993-998 (2008).

4 Creemer, J. F. *et al.* A MEMS Reactor for Atomic-Scale Microscopy of Nanomaterials Under Industrially Relevant Conditions. *Journal of Microelectromechanical Systems* **19**, 254-264, doi:10.1109/jmems.2010.2041190 (2010).

5 de Smit, E. *et al.* Nanoscale chemical imaging of a working catalyst by scanning transmission X-ray microscopy. *Nature* **456**, 222-225 (2008).

6 de Jonge, N., Bigelow, W. C. & Veith, G. M. Atmospheric Pressure Scanning Transmission Electron Microscopy. *Nano Lett.* **10**, 1028-1031, doi:10.1021/nl904254g (2010).

7 Allard, L., Bigelow, W., Overbury, S., Nackashi, D. & Damiano, J. Development of a Novel Environmental Cell for In-Situ Gas Reaction Experiments via Aberration-Corrected STEM Imaging. *Microscopy and Microanalysis* **16**, 296-297, doi:10.1017/s1431927610062495 (2010).

8 Yokosawa, T., Alan, T., Pandraud, G., Dam, B. & Zandbergen, H. In-situ TEM on (de)hydrogenation of Pd at 0.5–4.5 bar hydrogen pressure and 20–400°C. *Ultramicroscopy* **112**, 47-52, doi:10.1016/j.ultramic.2011.10.010 (2012).

9 Jonge, N. d., Peckys, D. B., Kremers, G. J. & Piston, D. W. Electron microscopy of whole cells in liquid with nanometer resolution. *Proceedings of the National Academy of Sciences* **106**, 2159-2164, doi:10.1073/pnas.0809567106 (2009).

10 van Huis, M. A. *et al.* Atomic Imaging of Phase Transitions and Morphology Transformations in Nanocrystals. *Advanced Materials* **21**, 4992-4995, doi:10.1002/adma.200902561 (2009).

11 Malladi, S. K. *et al.* Real-Time Atomic Scale Imaging of Nanostructural Evolution in Aluminum Alloys. *Nano Lett.*, doi:10.1021/nl404565j (2013).

12 Schlossmacher, P., Klenov, D. O., Freitag, B. & von Harrach, H. S. Enhanced Detection Sensitivity with a New Windowless XEDS System for AEM Based on Silicon Drift Detector Technology. *Microscopy Today* **18**, 14-20 (2010).

13 Malladi, S. R. K. *et al.* Early stages during localized corrosion of AA2024 TEM specimens in chloride environment. *Surface and Interface Analysis*, n/a-n/a, doi:10.1002/sia.5193 (2012).

14 Malladi, S. R. K. *et al.* Quasi *in situ* analytical TEM to investigate electrochemically induced microstructural changes in alloys: AA2024-T3 as an example. *Corrosion Science* **69**, 221-225, doi:10.1016/j.corsci.2012.12.006 (2013).

15 Boag, A. *et al.* How complex is the microstructure of AA2024-T3? *Corrosion Science* **51**, 1565-1568 (2009).

16 Boag, A., Hughes, A. E., Glenn, A. M., Muster, T. H. & McCulloch, D. Corrosion of AA2024-T3 Part I: Localised corrosion of isolated IM particles. *Corrosion Science* **53**, 17-26 (2011).

17 Guillaumin, V. & Mankowski, G. Localized corrosion of 2024 T351 aluminium alloy in chloride media. *Corrosion Science* **41**, 421-438 (1999).

Appendix E

1. More details from in-situ TEM movie

Only the most important features revealing localised corrosive attack at an anodic and cathodic precipitate have been emphasised in the main text. Here, more snapshots from the supplementary movie showing the other morphological changes are described. Figure E.1 shows a comparison between the frame at the very beginning after injecting the reactive gas mixture into the nanoreactor and a frame after the gradual removal of the HCl droplets from the specimen surface. In this time frame, some changes are observed at the edges of the specimen. As the specimens used in this study are FIB specimens, artefacts such as the re-deposited material from milling at the bottom of the trench and the beam damaged area on the top side are observed. The beam damage on the top can be minimised by depositing a platinum protective layer but this has been avoided to prevent a galvanic couple between the Pt layer and the Al specimen. As these do not interfere with our primary areas of interest in the specimen (grain boundaries and precipitate-matrix interfaces), the changes occurring at the specimen edges have been ignored in this study.

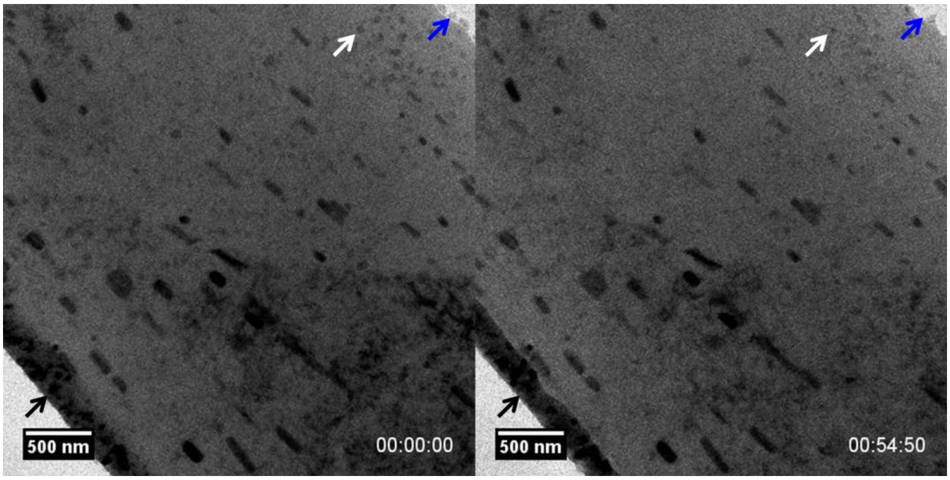

Figure E.1: Snapshots from the supplementary movie, the changes at the edges of the specimen are evident here, indicated by blue and black arrows. The diminished size of the aq. HCl droplets is quite evident.

A gradual decrease in the contrast of one of the grain boundary precipitate has been observed throughout the movie. This decrease in contrast is difficult to follow over the whole movie because there are also contrast changes in the Al matrix due to diffraction contrast variations (orientation changes as small as 0.1° can cause this) and hence the exact moment when the attack on this precipitate has initiated cannot be determined accurately. This can possibly be avoided in future experiments by carrying out experiments in STEM-HAADF mode. Figure E.2 shows that after nearly 3 hours of exposure to the corrosive environment, some matrix etching has also initiated.

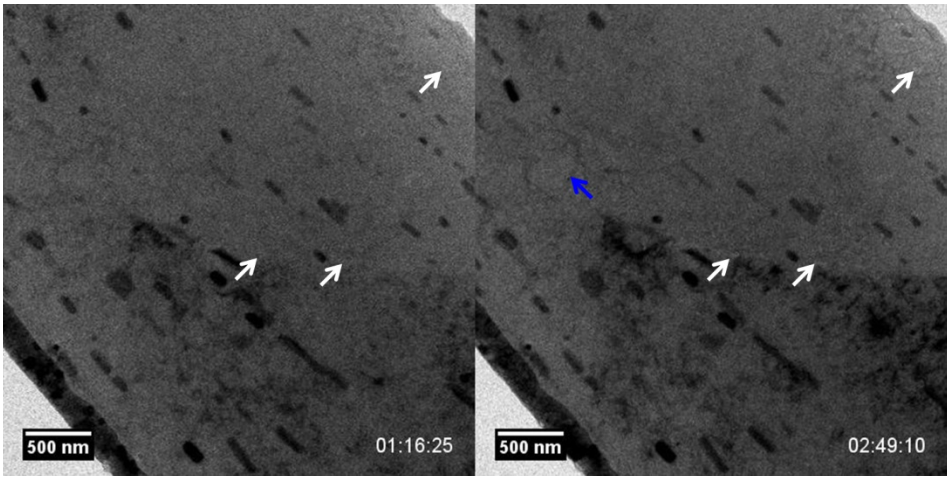

Figure E.2: In comparison with the image on the left, the image on the right shows the initiation of corrosion attack, signified by the bright spots next to the white arrows is evident. Also surface etching of the Al matrix is visible next to the blue arrow.

One of the challenges with *in situ* experiments is the unpredictability of events. From the quasi *in situ* experiments, we expected the initiation of corrosion attack within an hour, however, the experiment lasted longer and hence the HCl reservoir had to be refilled after 3 hours.

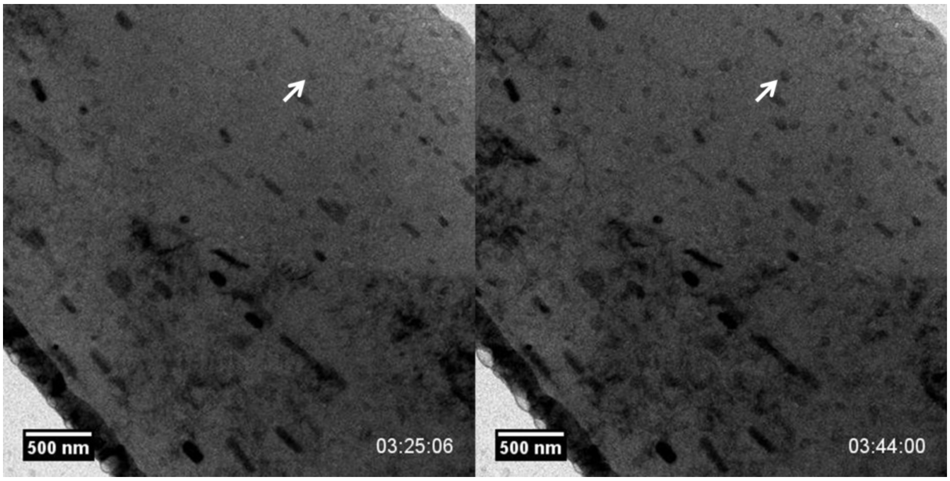

Figure E.3: Here the development of HCl droplets after refilling the HCl reservoir is shown.

Figure E.3 shows the reappearance of HCl droplets similar to the ones observed at the very beginning of the video. Further to these changes, significant morphological changes have been observed in the specimen. This can possibly be due to difference in the saturation levels of reactive gas mixture during the *quasi in situ* and *in situ* experiments, differences in the size of the flow channel and most importantly the constant illumination of the electron beam. Furthermore, the electron beam could induce a negative charge on the Al specimen surface, an effect similar to cathodic polarisation, which can cause a resistance to corrosive attack. On the other hand, the electron beam could also dissociate HCl to its respective ions, resulting in making Al susceptible to corrosion by Cl^- which is well documented.[1,2] Therefore, there are two counterbalancing effects under the electron beam. There is a good possibility that an enhanced corrosion attack is witnessed after the HCl has been refilled due to the aforementioned reason. This calls for more studies on optimising a controllable gas-liquid environment and as well as understanding the electron beam effects.

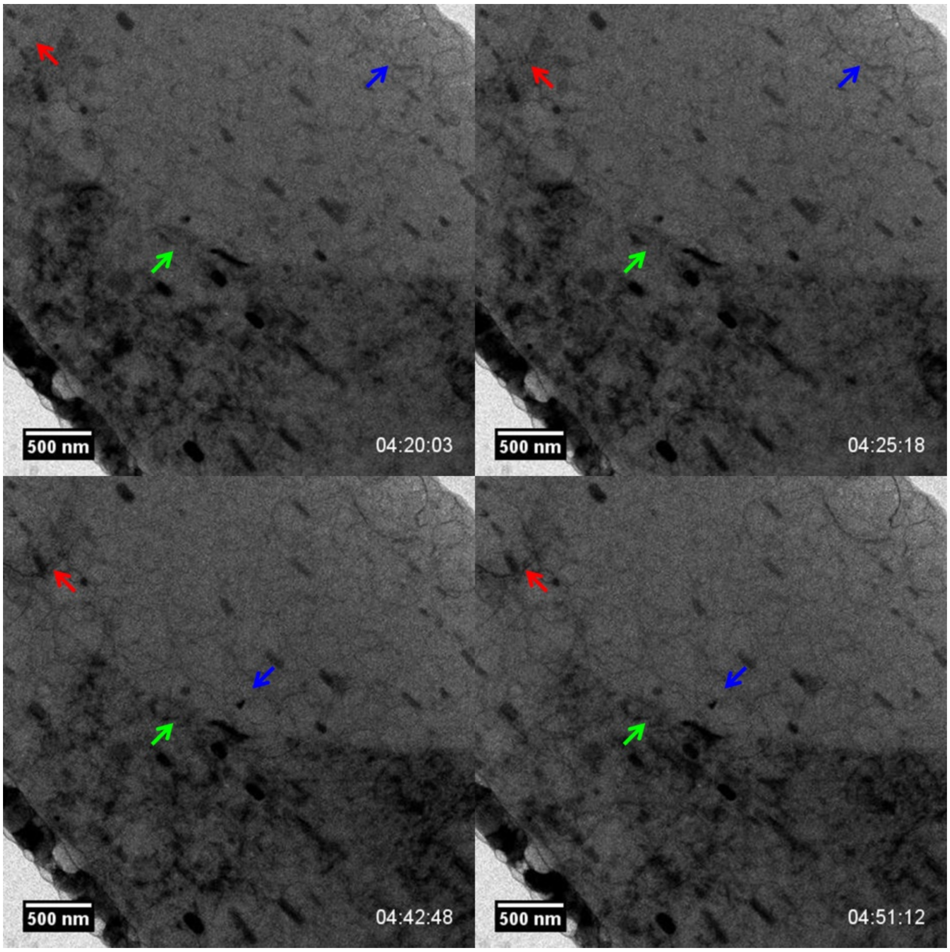

Figure E.4: Progression of corrosion attack at a grain boundary precipitate, as well as in the matrix.

In Figure E.4, the image on the top left shows the grain boundary precipitate next to the green arrow has a significantly diminished intensity compared with the previous images, while attack in the matrix is also observable next to the red and the blue arrows. In the next image on the top right, the matrix attack next to the intermetallic precipitates has progressed further as indicated by the red arrow while the matrix etching next to the blue arrow is more evident. In the image on the bottom left, the matrix attack next to the red arrow has progressed further but the most noticeable feature is the formation of the dark particle next to the blue arrow. In the image on the bottom right, obtained at the very end of the movie, the matrix etching is significant. On comparing the top two images with the bottom two images, the intensity of the grain boundary precipitate shown by the green arrow seems to have diminished significantly along with the formation of the dark particle next to the blue arrows.

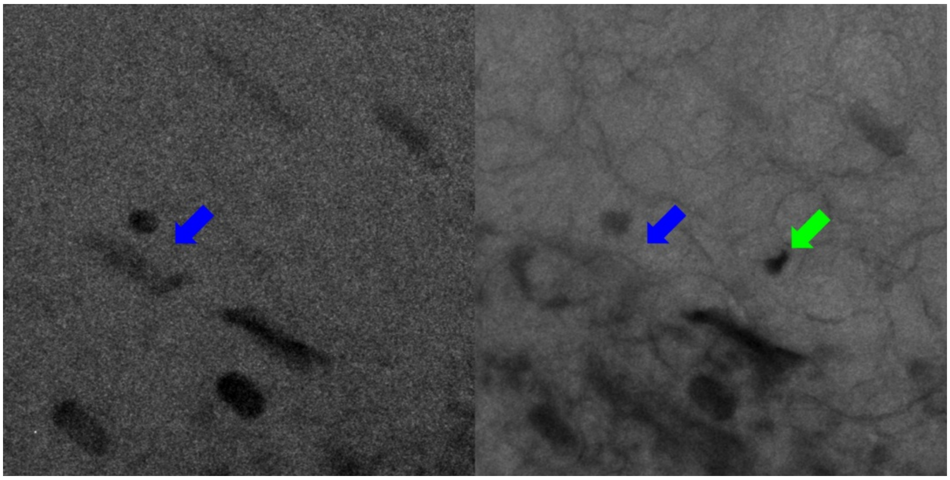

Figure E.5: Bright field images obtained before and after the corrosion experiments reveal the removal of grain boundary precipitate next to the blue arrow and the formation of a dark feature next to the green arrow (also shown as Figures 6.6c&d).

The dark contours, as visible in the Figure E.5 around the precipitate could be corrosion products from the precipitate while the dark particle shown by the green arrow could be the remnant material from de-alloyed matrix. These questions can be answered by combining the experiments with *in situ* elemental mapping.

2. Movie Caption

Supplementary Movie S6.1: An accelerated Bright-Field (BF) TEM movie showing the localised corrosion of a FIB specimen of AA2024-T3 at room temperature, exposed to O_2 bubbled through aqueous HCl of pH = 3 at a pressure of ~ 1.5 bar.

References

1 Guillaumin, V. & Mankowski, G. Localized corrosion of 2024 T351 aluminium alloy in chloride media. *Corrosion Science* **41**, 421-438 (1999).

2 Foley, R. T. Localized corrosion of Aluminium Alloys - A Review. *Corrosion* **42**, 277-288 (1986).

Chapter 7 CORROSION INHIBITION STUDIES[*]

This study has been carried out to understand the mechanism of cerium (Ce) based cathodic corrosion inhibition of aluminium (Al) alloy, AA2024-T3 on a sub-micron scale. The effects of exposure of an AA2024-T3 specimen to a 10 mM–1 mM sodium chloride-cerium chloride (NaCl–$CeCl_3$) electrolyte have been studied in a quasi in situ manner using analytical transmission electron microscopy (TEM), hereby focusing on the chemical composition of the specimen surface in an attempt to verify that corrosion is inhibited through the formation of a protective cerium oxide film over precipitates cathodic to the Al matrix. Preliminary observations on exposing the specimens of AA2024-T3 to the electrolyte for subsequent durations of 5, 10 and 45 minutes through elemental analysis using energy dispersive spectroscopy of X-rays (EDX), electron energy loss spectroscopy (EELS) and energy filtered TEM (EFTEM) show the signature of Ce at one of the cathodic, grain boundary precipitates. However, it has not yet been possible to determine the exact composition of the Ce-rich compound causing passivation. Because of the problems associated with the stability of the volatile Ce-rich compound under the electron beam, as well as the contamination from the experimental setup, it has not been possible to exactly determine the composition of the compounds causing the inhibition.

---

[*] These studies have been carried out with Jelle Stap as a part of his bachelor's thesis.

1. Background

Al alloys, extensively used in many fields of industry, consist of numerous second-phase precipitates[1,2] which enhance the corrosion susceptibility. This is due to the differences in the chemical potentials of precipitates and the Al matrix,[3] especially in effective and profuse electrolytes such as saltwater solutions[3] and in marine environments.[4] One way to minimise this problem is by using corrosion inhibitors,[5] retarding corrosive activity at alloy–electrolyte interfaces.

Conventional Al alloy corrosion protection techniques involve the use of organic paints that serve as an adhesive barrier between the alloy surface and the environment.[5] These coatings are nonetheless insufficient in keeping the surface completely free from moisture and oxygen (O_2). So for high protective qualities, it is common to use chromate conversion coatings (CCCs) mainly providing in *anodic* corrosion inhibition by impeding the electrochemical half-reactions at anode–electrolyte interfaces.[6] Environmental concerns have however discredited the use of chromate coatings, and new techniques using rare earth salts of Ce and lanthanum (La) have been developed.[7,8] It is believed that these rare-earth compounds act as *cathodic* inhibitors through precipitation of rare-earth species onto cathode–electrolyte interfaces and the formation of a protective rare-earth oxide film, retarding electrochemical activity at these interfaces and reducing corrosion.[9] Electrochemical studies have shown that exposure of specific Al alloys—including AA2024-T3—to rare-earth compound solutions such as a $CeCl_3$ solution significantly impedes their corrosion rates, so that $CeCl_3$ acts as a corrosion inhibitor for these alloys.[5,10,11] It is believed that when an AA2024-T3 specimen is immersed in a $CeCl_3$ solution, Ce^{3+} anions in the electrolyte adsorb onto precipitates cathodic to the Al matrix. It has been proposed that Ce species subsequently react with ions in the electrolyte to form passive cerium oxide films through the following reactions:

Initiation (oxygen reduction)

$$Ce^{3+} + 3OH^- \rightarrow Ce(OH)_3 \downarrow \qquad (1)$$

$$Ce^{3+} + 3OH^- \rightarrow Ce(OH)_2^{2+} \qquad (2)$$

Propagation

$$Ce(OH)_3 \rightarrow CeO_2 \downarrow + H_2O + H^+ + e^- \qquad (3)$$

$$Ce(OH)_2^{2+} + 2OH^- \rightarrow CeO_2 \downarrow + 2H_2O \qquad (4)$$

$$Ce(OH)_2^{2+} + 2OH^- + e^- \rightarrow Ce(OH)_3 \downarrow \qquad (5)$$

accordingly inhibiting corrosion through the precipitation of cerium oxide (CeO_2) and cerium hydroxide ($Ce(OH)_3$).[5,12,13]

The objectives of this quasi *in situ* analytical TEM study are to investigate the mechanisms of Ce-based corrosion inhibition on surfaces of the common commercial Al alloy AA2024-T3 in a 10 mM–1 mM NaCl–$CeCl_3$ solution on a sub-micron scale, and to validate the suggestion that Ce species in the electrolyte lead to cathodic corrosion inhibition of AA2024-T3. Therefore, in validating the above mechanism, it is expedient to look for deposition of Ce and O species onto the specimen, specifically near cathodic precipitates.

2. Materials and methods

2.1. Specimen preparation

Four 0.8 mm-thick bulk AA2024-T3 specimen sheets are polished using P1200, P2500 and P4000 SiC polishing papers to achieve smooth surfaces for conducting electrochemical bulk sample studies. Furthermore, a similar AA2024-T3 specimen sheet is made sufficiently thin for TEM studies using P320 and P1200 SiC polishing papers until a thickness of ~10 µm is established, after which a 3 mm-diameter circular disc is punched for containment in a phosphor–bronze TEM cartridge allowing for accurate positioning and TEM analysis. It is thinned down to ≤ 100 nm through a Gatan Precision Ion Polishing System (PIPS) for electron-transparency.

2.2. Electrochemical studies

Common electrolytes used for electrochemical corrosion studies on AA2024-T3 are aqueous solutions of 3.5%-weight or 1 M NaCl concentrations.[14] For the small thicknesses concerned with TEM specimens, however, it has been observed that use of such concentrated NaCl electrolytes results in problems concerning deposition of NaCl crystals or complete dissolution of the electron-transparent area into the electrolyte.[14,15]

To determine whether smaller concentrations are suitable for imposing corrosion, electrochemical studies on AA2024-T3 bulk specimens are done. Bulk samples of AA2024-T3 are exposed in pairs of two to 10 mM NaCl and 10 mM–1 mM NaCl–$CeCl_3$ solution using a cylindrical cell with 1-inch-diameter opening. Open-circuit potential (OCP) measurements with respect to a silver-silver chloride reference electrode (Ag–AgCl) are carried out, followed by potentiodynamic polarisation (PDP) measurements. These experiments should allow us to determine the electrochemical activity of AA2024-T3 in the electrolytes and whether exposure of an AA2024-T3 sample to a 10 mM–1 mM NaCl–$CeCl_3$ solution initiates both Cl^--imposed corrosion and Ce-imposed passivation, necessary for the studies. The effects of electrolyte exposure over larger areas are compared by visual inspection from optical micrographs and photographs.

2.3. Quasi in-situ TEM studies

Suitable regions on the AA2024-T3 specimen in the phosphor–bronze cartridge containing grain boundaries and plenty of precipitates are located using a 200 kV FEI Tecnai F20ST/STEM microscope, and digitally marked using Gatan DigitalMicrograph software for relocation. Compositional analysis of the region is executed using the same microscope, which is equipped with a high-resolution Gatan imaging filter (GIF) for EFTEM, EELS as well as EDX. Electrolyte exposure effects on the AA2024-T3 specimen are studied in a quasi *in situ* manner.[16] The specimen is immersed in the electrolyte thrice for increasing time intervals of 5, 10 and 45 minutes, respectively, adding up to a total electrolyte exposure of 60 minutes. After each immersion, the marked locations are analysed for morphological changes using TEM, and chemical composition variations using EDX, EFTEM and EELS, hereby focusing on Ce deposition and O build-up at cathodic precipitates as a signature of inhibition by cerium oxide species.

3. Results and discussion

3.1. Electrochemical studies

3.1.1. Open-circuit potential (OCP)

OCP measurements on two bulk-samples of AA2024-T3 exposed to a 10 mM NaCl and a 10 mM–1 mM NaCl–$CeCl_3$ solution, respectively, are shown in Figure 7.1. The sample immersed in the NaCl solution shows OCP values of approximately −530 mV (±10 mV), until a potential of −521 mV is obtained after one hour of electrolyte exposure.

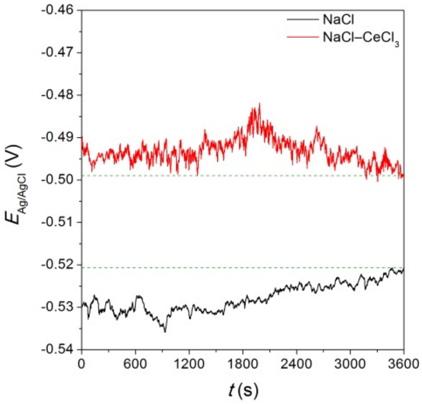

Figure 7.1: OCP measurements on two bulk AA2024-T3 specimens on exposure to 10 mM NaCl and 10 mM-1 mM NaCl-$CeCl_3$ solution (measured with respect to an Ag–AgCl reference electrode) versus time.

The sample immersed in the NaCl–$CeCl_3$ solution shows OCP values of approximately −490 mV (±10 mV), until a potential of −499 mV is obtained after one hour of exposure. The OCP curves indicate a lower electrochemical activity for the AA2024-T3 specimen exposed to the NaCl–$CeCl_3$ electrolyte in comparison to the NaCl solution.

3.1.2. Potentiodynamic polarisation (PDP)

PDP curves of two bulk AA2024-T3 specimens exposed to a 10 mM NaCl and a 10 mM–1 mM NaCl–$CeCl_3$ solution, respectively, with potentials running from 0.5 V below to 1 V above OCP, are shown in Figure 7.2.

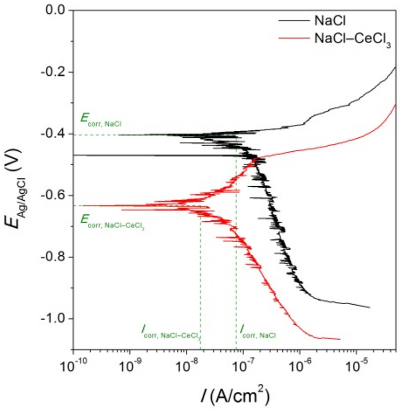

Figure 7.2: PDP curves of two bulk AA2024-T3 specimens on exposure to a 10 mM NaCl and a 10 mM–1 mM NaCl–CeCl3 solution, running from −0.5 V to 1 V above OCP (range shown is approximately −0.5 V to 0.5 V above OCP). The green dotted lines indicate the free corrosion potentials (E_{corr}) and the corrosion currents (I_{corr}).

Each curve shows two branches, i.e. a cathodic and an anodic branch for lower and higher potentials than the OCP, respectively, reflecting all reduction and oxidation reactions in the system. The observed corrosion currents I_{corr} for the NaCl and NaCl-$CeCl_3$ solutions are approximately 8 × 10^{-8} A/cm^2 and 2 × 10^{-8} A/cm^2, respectively, indicating a lower corrosive activity for the sample exposed to the NaCl–$CeCl_3$ solution.

The observed lower current densities and corrosive activity of the cathodic branch associated with NaCl–$CeCl_3$ exposure suggest that corrosion is retarded by i.e. the reduction of Ce^{3+} ions in the solution, related to the formation of a cerium oxide film (Equations 1–2). The kink in the anodic branch of the curve up until approximately −0.5 V also indicates passivation, possibly through enhanced oxidation of $Ce(OH)_3$ (Equation 3).

3.1.3. Optical micrographs

Photographs and optical micrographs of the two bulk AA2024-T3 samples after one hour of exposure to a 10 mM NaCl and a 10 mM–1 mM NaCl–$CeCl_3$ solution, respectively, are given in Figure 7.3. The areas of the inner circles in the photographs, Figure 7.3(a, b), are exposed to the electrolytes in the cylindrical cell. The O-rings used to seal the electrolytes form the impression of the annular rings.

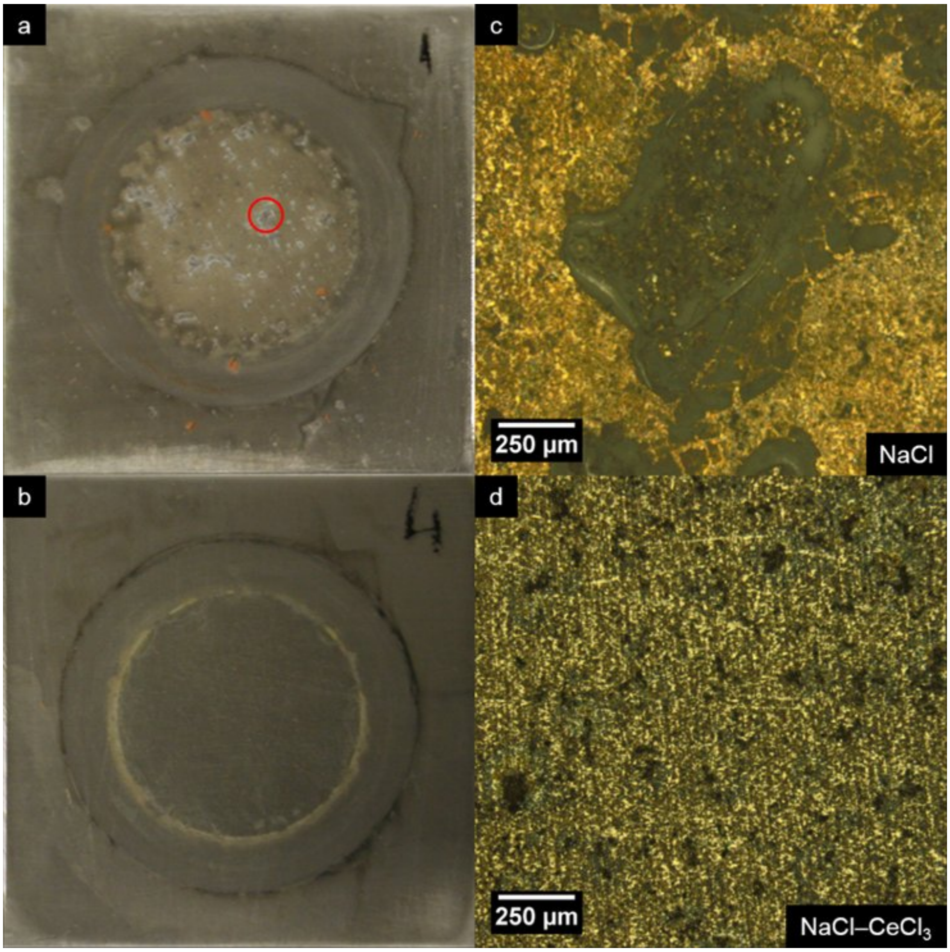

Figure 7.3: Photographs (a, b) and optical micrographs (c, d) of two AA2024-T3 bulk samples after one hour of exposure to a 10 mM NaCl electrolyte and a 10 mM–1 mM NaCl–$CeCl_3$ electrolyte, respectively; (c) is an optical micrograph of the area indicated by the red circle in (a), and (d) is an optical micrograph of the apparently uniform surface area in (b).

The photograph of the specimen exposed to the NaCl solution (Figure 7.3(a)) shows several irregularities and a non-uniform surface area, indicating corrosive activity. The red circle indicates an area showing such corrosive activity, and an optical micrograph of the area is given in Figure 7.3(c). In contrast to the NaCl-exposed specimen, a photograph of the specimen exposed to the NaCl–$CeCl_3$ solution reveals a uniform, surface (Figure 7.3(b)) covered with some sort of a film as observed in the corresponding optical micrograph. The images and micrographs clearly show that the sample exposed to the NaCl solution has more corrosive activity than that exposed to the NaCl–$CeCl_3$ solution.

3.1.4. Discussion

The OCP measurements, PDP curves and optical micrographs show that 60 minutes of exposure to a 10 mM–1 mM NaCl–$CeCl_3$ solution is sufficient to investigate the corrosion inhibition behaviour of AA2024-T3. The data also reveal that the corrosion current I_{corr} is approximately 4 times lower on exposure of AA2024-T3 to this electrolyte than to a 10 mM NaCl solution, and suggest the formation of a protective cerium oxide film inhibiting corrosion. It is therefore concluded that exposure of AA2024-T3 to a 10 mM–1 mM NaCl–$CeCl_3$ solution for 60 minutes is suitable for the quasi *in situ* TEM studies.

3.2. Quasi *in situ* TEM studies

Using TEM an AA2024-T3 specimen is checked for suitable areas containing precipitates in the proximity of a grain boundary, as this is where the highest chemical reactivity can be expected. Grain boundaries can be distinguished due to the diffraction contrast caused by orientation differences of different grains, whereas precipitates are distinguished through mass–thickness contrast. The hereby caused variations in transmitted electron intensity can be translated into bright-field (BF-TEM) images.

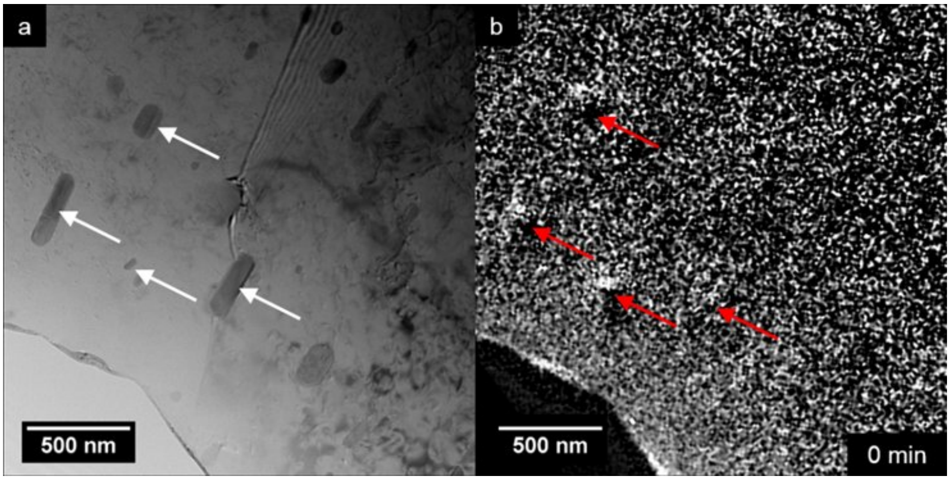

Figure 7.4: (a) BF-TEM image and (b) EFTEM O-map of the selected region on the AA2024-T3 specimen, prior to electrolyte immersion. The arrows indicate examples of precipitates, which are also visible in the O-map due to the inhomogeneous character of the oxide film around these precipitates.

A BF-TEM image of a suitable area is shown in Figure 7.4(a), and the corresponding EFTEM O-map is shown in Figure 7.4(b). The EFTEM O-map shows that the area in the field of view is largely covered with O with subtle variations in O-signal over the precipitates. The compositional analysis of precipitates numbered in Figure 7.5 is carried out using EDX. The results are given in Table 7.1.

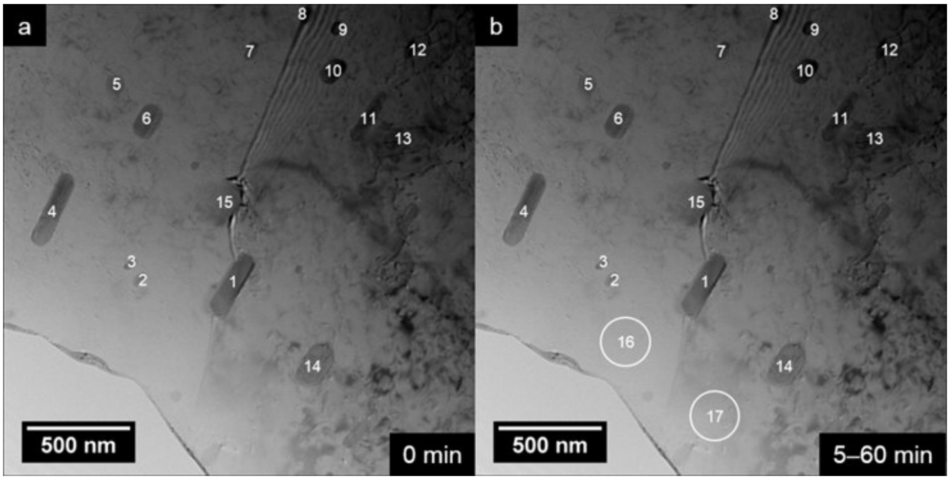

Figure 7.5: Indications of precipitates (numbered), parts of the matrix (numbered circles) from which EDX measurements have been carried out in the selected specimen region.

Table 7.1: Results from EDX measurements (within ± 1 atom% accuracy) of the numbered precipitates in Figure 7.5, prior to electrolyte immersion. The values have been rounded off to the nearest whole number.

#	O	Mg	Al	Si	Mn	Cu
1	3	-	73	1	12	10
2	12	1	72	1	6	8
3	10	2	79	1	2	5
4	10	-	71	1	10	9
5	4	2	86	1	3	4
6	5	2	80	1	6	6
7	-	2	90	-	3	4
8	3	2	87	1	3	4
9	3	2	86	1	3	5
10	4	2	85	1	3	5
11	3	2	86	1	2	5
12	4	2	87	1	2	3
13	3	2	85	1	4	5
14	11	1	72	2	7	8
15	5	2	81	1	4	6

Most precipitates in the matrix have a plate-type shape with an aspect ratio of approximately 3:1. These precipitates mainly contain manganese (Mn) and copper (Cu) (possibly $Al_{20}Mn_3Cu_2$[17]) and only minor amounts of magnesium (Mg) and silicon (Si), indicating cathodic behaviour to the Al matrix. The entire region contains O, mainly from the aluminium oxide film on the matrix, and at precipitates #2, #3, #4 and #14 in particular.

BF-TEM images (a–c) and EFTEM O-maps (d–f) of the specimen area after 5, 15 and 60 minutes of electrolyte exposure, respectively, are shown in Figure 7.6. Furthermore, EDX compositional analysis of the precipitates and parts of the matrix indicated in Figure 7.5 is executed at each of the intermediate stages of electrolyte exposure (Appendix F). From the EDX measurements, plots of the elements showing the largest variations (O and Cu) are given in Figure 7.7.

3.2.1. 5 minutes

The BF-TEM image obtained after 5 minutes of electrolyte exposure (Figure 7.6(a)) reveals no significant morphological changes in comparison to the preliminary situation (Figure 7.4(a)), and the corresponding EFTEM O-map (Figure 7.6(d)) is also very similar to the initial situation (Figure 7.4(b)). EDX measurements (Table F.1) confirm this—apart from a slight increase in O at precipitate #1 no major differences are observed.

3.2.2. 15 minutes

The BF-TEM image of the specimen area after 15 minutes of electrolyte exposure does not reveal any significant morphological changes in the matrix (Figure 7.6(b)), although a closer look at the proximities of precipitate #12 shows the appearance of a dark feature. An EDX measurement of precipitate #12 reveals an increase in Cu (Table F.2). The EFTEM O-map after 15 minutes of electrolyte exposure as shown in Figure 7.6(e) displays a uniform oxide film. EDX (Table F.2) confirms this observation, since the O-amounts have mostly increased at both precipitates and the matrix. It is concluded that an oxide film covering both the matrix and precipitates is formed after 15 minutes of electrolyte exposure—in contrast to the initial, untreated, specimen.

3.2.3. 60 minutes

The BF-TEM image of the specimen after 60 minutes of electrolyte exposure (Figure 7.6(c)) does not reveal any contrast changes concerning precipitates or the matrix, but does suggest the presence of an increased number of Cu clusters, such as observed after 15 minutes of exposure, shown by circles in Figure 7.6. EDX measurements (Table F.2) affirm that these are indeed Cu-rich phases. The EFTEM O-map after 60 minutes of exposure (Figure 7.6(f)) shows a uniformly covered oxide film, confirmed by EDX (Table F.2)—no major differences in O compared to the situation after 15 minutes of exposure are observed. It is concluded that the oxide film has stabilised, and that a significant amount of Cu is deposited at the specimen surface.

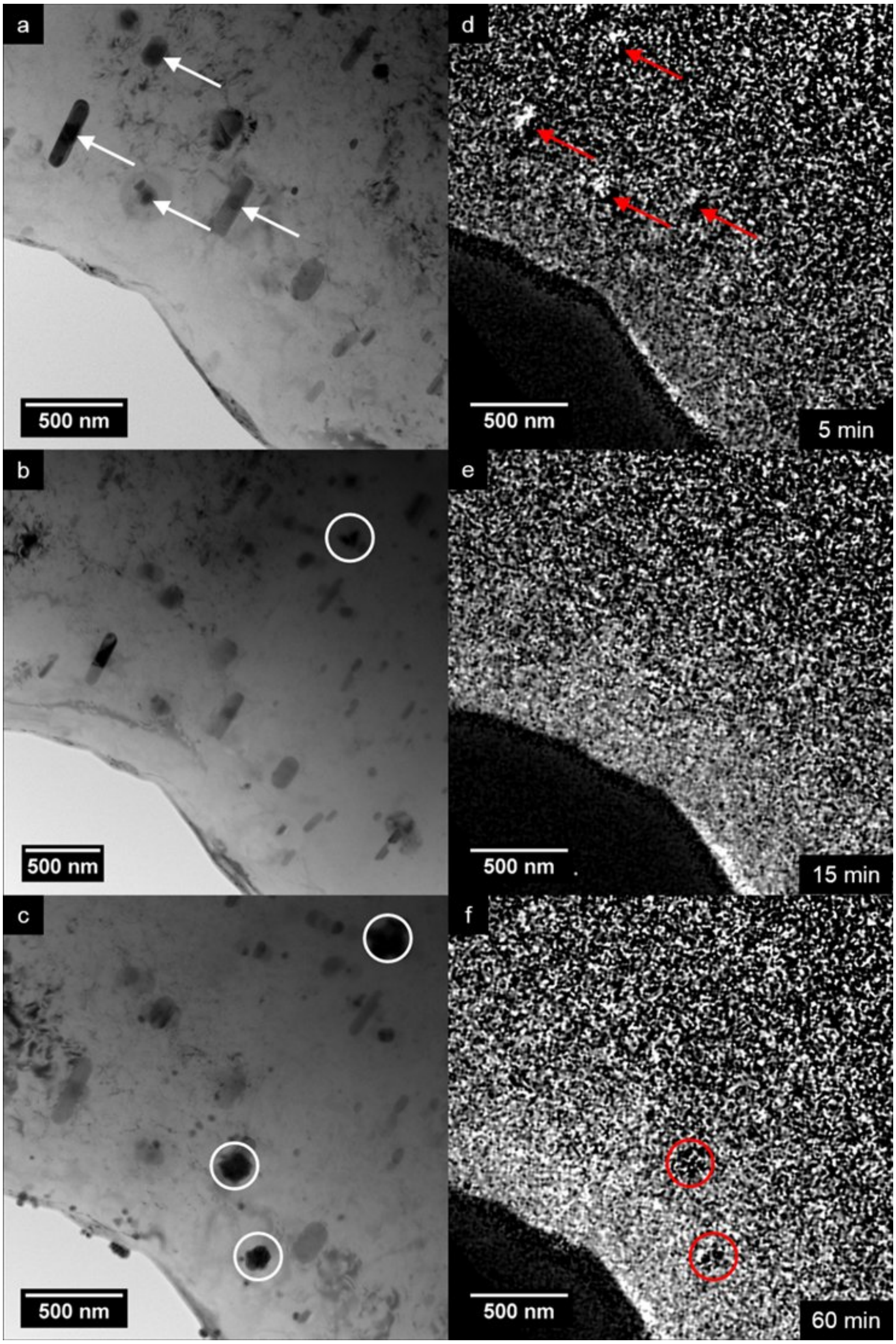

Figure 7.6: BF-TEM images (a–c) and EFTEM O-maps (d–f) of the specimen area; after 5, 15 and 60 minutes of electrolyte exposure, respectively. The arrows indicate the precipitates as given in Figure 7.5, and the circles indicate the deposition of Cu clusters.

3.2.4. Compositional analysis

From the bar graphs shown in Figure 7.7, a gradual O build-up during electrolyte immersion is observed on both matrix and precipitates. As discussed earlier, this is assigned to the formation of a uniform oxide film. Furthermore, the strong increase in Cu at precipitates #1 and #12 is prominent.

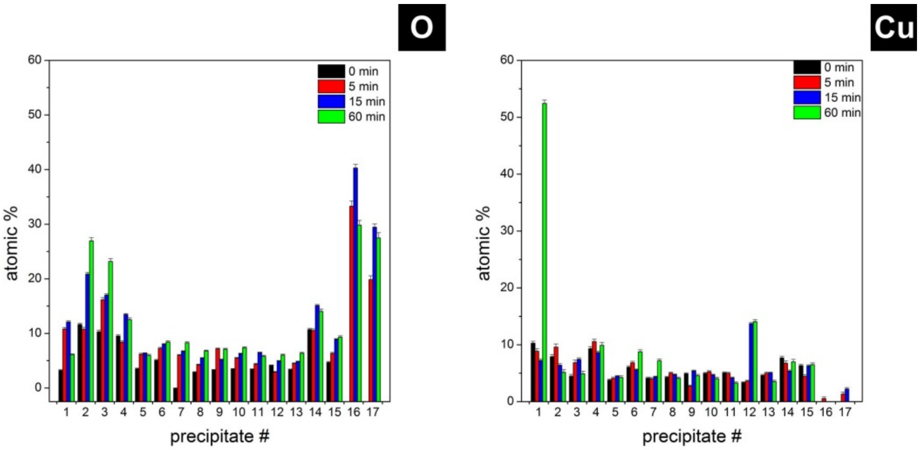

Figure 7.7: Bar graphs showing the variation in O and Cu content for each precipitate from EDX analysis. Note that no preliminary EDX measurements have been executed on the two parts of the matrix (#16–17).

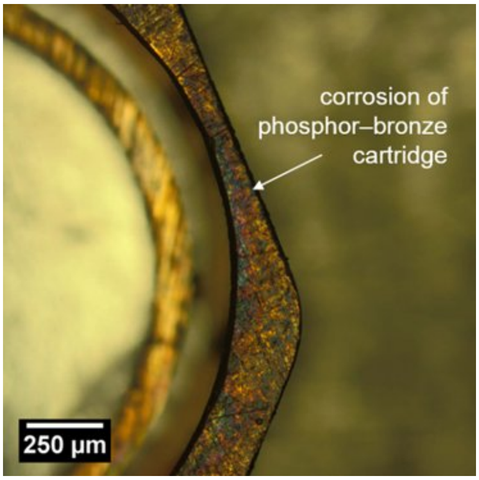

Figure 7.8: Optical micrograph of the phosphor–bronze specimen holder after conducting the quasi in situ TEM experiments and the corresponding electrolyte exposure.

The observed Cu clusters could be formed due to de-alloying of the matrix or precipitates. This would yield local corrosion attack on the specimen, visible through contrast differences in the matrix or precipitates in the BF-TEM images, Figure 7.6(b-c), or inhomogeneity of the EFTEM O-maps, Figure 7.6(e–f), due to depletion of the oxide layer.[15,16] Since there is no contrast change in the matrix close to precipitates and the oxide film seems to be quite uniform from the EFTEM O-maps, the Cu cluster is not interpreted as being a result from de-alloying of the matrix or precipitates.

From an optical micrograph of the phosphor–bronze quasi *in situ* TEM specimen holder after conducting the experiments (Figure 7.8), one could get a different impression. The cartridge has corroded on exposure to the electrolyte. It is concluded that the cartridge is the source of the observed Cu contamination of the specimen after 60 min electrolyte exposure. Another interesting observation though is that EEL-spectrum of the specimen (precipitate #1 in Figure 7.5, exposure time 20 seconds) immediately after 15 minutes of electrolyte exposure shows a strong Ce M_5-edge, but a subsequent EEL-spectrum using the same parameters from the same location shows a decrease in the peak height of Ce M_5-edge.

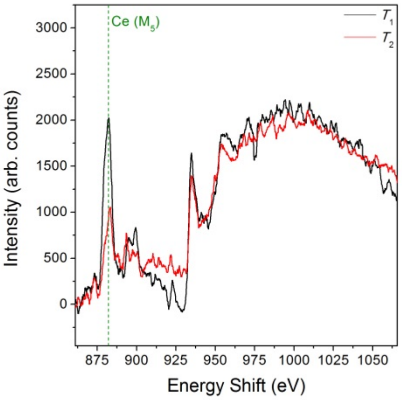

Figure 7.9: EEL-spectra showing the Ce M_5-edge[18] from precipitate #15 after 15 minutes of electrolyte exposure; T_1 is the first spectrum after electrolyte exposure and T_2 is the subsequent spectrum immediately after T_1.

3.2.5. Discussion

Analysis of the BF-TEM images, EFTEM O-maps and EDX spectra of the AA2024-T3 specimen, and of the micrograph of the specimen holder leads to two main observations that exposure of the specimen to a 10 mM–1 mM NaCl–$CeCl_3$ solution initiates the growth of an oxide film on both precipitates and prolonged exposure to the electrolyte causes the deposition of Cu rich clusters onto the specimen surface (possibly from the phosphor-bronze cartridge). Comparing the EFTEM O-maps and obtained after 5, 15 and 60 minute exposures, Figure 7.6, O cover over the specimen surface is observed from the EFTEM map after 15 minutes exposure. The EDX analysis also shows an increase in the O content. There has not been a signature of corrosion attack in the field of view as well as in the neighbouring regions even after 60 minute exposure as previously observed in *ex situ* and quasi *in situ* studies on the same material in chloride environments. The optical micrographs from the phosphor bronze cartridge indicate de-alloying of phosphor-bronze cartridge.

The observed growth of the oxide film concerning precipitates is consistent with the suggested mechanism of Ce-based corrosion inhibition of AA2024-T3—electrolyte exposure of the alloy leads to the formation of a protective oxide film. Interesting to see, however, is that the expected increase in Ce species involved with the formation of a local cerium oxide film is absent. This is explained through the observed decrease in Ce during the execution of EELS measurements, as shown in Figure 7.9. It suggests that although Ce is deposited at the specimen surface, exposure of the specimen to the TEM electron beam results in the depletion of adhered Ce. This could possibly be due to the knock-on damage of oxide ion or hydroxide ion from the volatile Ce-based compound.[19] The exact mechanism behind this still remains an open question.

A way to tackle the problem of Cu contamination could be the use of titanium (Ti) specimen cartridges instead of the phosphor–bronze holders utilised in this study. Ti being more corrosion resistant than phosphor-bronze should not give the contamination arising due to the cartridge. Initial attempts using Ti cartridge have not been successful due to problems related to the quality of the specimens. Possibilities preventing the problem concerning Ce detection would be the use of low-energy electron microscopy (LEEM)[20] or high-resolution nano-scale secondary ion mass spectrometry (NanoSIMS)[21]—avoiding high-voltage electron beams—which are possibly more suitable in accurate detection of volatile Ce based compounds than the TEM measurements carried out in this study.

4. Conclusions

OCP and PDP curves show that exposure of an AA2024-T3 specimen to a 10 mM–1 mM NaCl–$CeCl_3$ solution leads to significantly smaller corrosion rates than on exposure to a 10 mM NaCl solution, so that $CeCl_3$ inhibits corrosion of AA2024-T3.

Quasi *in situ* TEM studies and EDX and EFTEM measurements reveal the formation of a stable and uniform protective oxide film on the specimen surface after 15 minutes of electrolyte exposure. Although this oxide film is expected to be a cerium oxide film, Ce-enrichment could not be validated using the high-voltage electron beam involved in the studies. EEL-spectra did however show the initial deposition of Ce. Using TEM, EDX and EFTEM, deposition of Cu clusters onto the specimen surface has been observed after 15 minutes of exposure to the electrolyte as a result of de-alloying of the phosphor–bronze specimen holder.

This study shows preliminary results in the direction proposed mechanism of Ce-based cathodic inhibition in Al alloys, but further research is expedient in affirming the mechanisms and electrochemical principles of corrosion inhibition.

Since the high-voltage electron beam involved in this research seems to be too strong for the studies, one could repeat the studies using alternative compositional analysis techniques such as low-energy electron microscopy (LEEM) or nano-scale secondary ion mass spectrometry (NanoSIMS) instead in order to determine the chemical composition of the oxide film. Additionally, one could utilise Ti cartridges in order to prevent Cu contamination from the specimen holder.

References

1 Tiryakioğlu, M. & Stanley, J. T. in *Handbook of Aluminum: Physical Metallurgy and Processes* Vol. 1 *Handbook of Aluminum* (eds George E. Totten & D. Scott MacKenzie) Ch. 3, 81–210 (Marcel Dekker Inc., 2003).

2 Katgerman, L. & Eskin, D. in *Handbook of Aluminum: Physical Metallurgy and Processes* Vol. 1 *Handbook of Aluminum* (eds George E. Totten & D. Scott MacKenzie) Ch. 5, 259–304 (Marcel Dekker Inc., 2003).

3 Foley, R. T. Localized Corrosion of Aluminum Alloys—A Review. *Corrosion* **42**, 277–288 (1986).

4 Szklarska-Smialowska, Z. Pitting corrosion of aluminum. *Corrosion Science* **41**, 1743–1767 (1999).

5 Garcia, S. J. *et al.* in *Self-Healing Properties of New Surface Treatmens: (EFC 58)* Ch. 9, 148–183 (Maney Publishing, 2011).

6 Zhang, W. *Formation and corrosion inhibition mechanisms of chromate conversion coatings on aluminum and AA2024-T3* Doctor of Philosophy thesis, The Ohio State University, (2002).

7 El-Meligi, A. A. Corrosion Preventive Strategies as a Crucial Need for Decreasing Environmental Pollution and Saving Economics. *Recent Patents on Corrosion Science* **2**, 22–33, doi:10.2174/1877610801002010022 (2002).

8 Ashraf, P. M. & Shibli, S. M. A. Reinforcing aluminium with cerium oxide: A new and effective technique to prevent corrosion in marine environments. *Electrochemistry Communications* **9**, 443–448 (2007).

9 Andreatta, F. *et al.* Localized corrosion inhibition by cerium species on clad AA2024 aluminium alloy investigated by means of electrochemical micro-cell. *Corrosion Science* **65**, 376–386, doi:DOI 10.1016/j.corsci.2012.08.053 (2012).

10 Mishra, A. K. & Balasubramaniam, R. Corrosion inhibition of aluminium by rare earth chlorides. *Materials Chemistry and Physics* **103**, 385–393 (2007).

11 Yasakau, K. A., Zheludkevich, M. L., Lamaka, S. V. & Ferreira, M. G. Mechanism of corrosion inhibition of AA2024 by rare-earth compounds. *The Journal of Physical Chemistry B* **110**, 5515–5528, doi:10.1021/jp0560664 (2006).

12 Gao, M., Feng, C. R. & Wei, R. P. An analytical electron microscopy study of constituent particles in commercial 7075-T6 and 2024-T3 alloys. *Metallurgical and Materials Transactions A—Physical Metallurgy and Materials Science* **29**, 1145–1151, doi:DOI 10.1007/s11661-998-0240-9 (1998).

13 Groen, B. *Tecnai Basic*. (FEI Electron Optics B.V., 2002).

14 Jegdić, B. V., Živković, L. S., Popić, J. P., Bajat, J. B. & Mišković-Stanković, V. B. Electrochemical methods for corrosion testing of Ce-based coating prepared on AA6060 alloy by dip immersion method. *Journal of the Serbian Chemical Society* **78**, 1–21 (2011).

15 Malladi, S. R. K. *et al.* Early stages during localized corrosion of AA2024 TEM specimens in chloride environment. *Surface and Interface Analysis*, 1–7 (2012).

16 Malladi, S. R. K. *et al.* Quasi *in situ* analytical TEM to investigate electrochemically induced microstructural changes in alloys: AA2024-T3 as an example. *Corrosion Science* **69**, 221–225 (2013).

17 Chen, C. P., Hsu, T. C., Wang, W., Guillaumin, V. & Mankowski, G. Localized corrosion of 2024 T351 aluminium alloy in chloride media. *Corrosion Science* **41**, 421–438 (1998).

18 Arai, S. *et al.* Valence Change of Cations in Ceria-Zirconia Solid Solution Associated with Redox Reactions Studied with Electron Energy-Loss Spectroscopy. *Materials Transactions* **45**, 2951–2955 (2004).

19 Carlson, D. B. & Evans, J. E. in *The Transmission Electron Microscope* (ed Khan Maaz) 85–98 (InTech, 2012).

20 Bauer, E. Low energy electron microscopy. *Reports on Progress in Physics* **57**, 895–938 (1994).

21 Fletcher, J. S. & Vickerman, J. C. Secondary Ion Mass Spectrometry: Characterizing Complex Samples in Two and Three Dimensions. *Analytical Chemistry* **85**, 610–639 (2013).

Appendix F

Table F.1: EDX measurements of the precipitates (#1–15) and parts of the matrix (#16–17) as marked in Figure 7.5; prior to, and after 5 minutes of electrolyte exposure, respectively.

#	**Element**	**O (K)**	**Mg (K)**	**Al (K)**	**Si (K)**	**Mn (K)**	**Cu (K)**	**O (K)**	**Mg (K)**	**Al (K)**	**Si (K)**	**Mn (K)**	**Cu (K)**	**Ce (M)**
	Detector Correction	**0.51**	**0.88**	**0.92**	**0.92**	**0.99**	**0.99**	**0.51**	**0.88**	**0.92**	**0.92**	**0.99**	**0.99**	**0.99**
	k-factor	**1.889**	**1.050**	**1.030**	**1.000**	**1.372**	**1.663**	**1.889**	**1.050**	**1.030**	**1.000**	**1.372**	**1.663**	**1.532**
1	**Atomic %**	3.2		72.5	0.9	12.4	10.3	10.8		62.8	2.8	14.2	8.9	0.5
	Uncert. %	0.2		0.6	0.1	0.3	0.4	0.3		0.7	0.1	0.4	0.5	0.1
2	**Atomic %**	11.6	1.2	71.7	1.0	6.2	7.9	10.8	0.6	69.1	3.4	6.5	9.6	0.1
	Uncert. %	0.2	0.1	0.7	0.1	0.3	0.4	0.4	0.1	0.9	0.2	0.4	0.5	0.1
3	**Atomic %**	10.3	2.2	78.8	1.4	2.4	4.5	16.2	0.9	64.6	3.2	7.8	6.9	0.4
	Uncert. %	0.3	0.1	0.7	0.1	0.2	0.3	0.4	0.1	0.8	0.2	0.4	0.5	0.1
4	**Atomic %**	9.5	0.1	70.8	0.7	9.5	9.3	8.4	0.3	67.3	2.8	10.2	10.6	0.5
	Uncert. %	0.2	0.0	0.6	0.1	0.3	0.4	0.3	0.0	0.6	0.1	0.4	0.4	0.1
5	**Atomic %**	3.5	2.3	85.6	0.8	3.3	3.8	6.2	2.1	83.8	1.2	2.5	4.1	
	Uncert. %	0.1	0.1	0.5	0.0	0.1	0.2	0.2	0.1	0.6	0.1	0.2	0.2	
6	**Atomic %**	5.1	1.8	79.8	0.9	5.9	6.1	7.3	1.4	77.5	1.8	4.6	6.8	0.5
	Uncert. %	0.2	0.1	0.5	0.1	0.2	0.2	0.2	0.1	0.6	0.1	0.2	0.3	0.1
7	**Atomic %**		1.8	90.0	0.3	3.3	4.1	6.0	2.0	84.2	1.5	2.3	4.0	
	Uncert. %		0.1	0.5	0.0	0.1	0.2	0.2	0.1	0.5	0.1	0.1	0.2	
8	**Atomic %**	2.9	2.4	86.7	0.7	2.7	4.3	4.3	2.1	84.2	1.4	2.6	5.0	0.3
	Uncert. %	0.1	0.1	0.4	0.0	0.1	0.2	0.1	0.1	0.5	0.1	0.1	0.2	0.1
9	**Atomic %**	3.3	2.3	85.5	0.8	2.8	4.9	7.2	2.6	83.8	1.2	2.2	2.8	0.2
	Uncert. %	0.1	0.1	0.4	0.0	0.1	0.2	0.1	0.1	0.5	0.1	0.1	0.2	0.1
10	**Atomic %**	3.5	2.4	84.5	0.8	3.3	5.0	5.5	2.2	81.8	1.7	3.2	5.3	0.4
	Uncert. %	0.1	0.1	0.4	0.0	0.1	0.2	0.1	0.1	0.5	0.1	0.1	0.2	0.1
11	**Atomic %**	3.4	2.3	85.9	0.6	2.4	5.1	4.4	2.8	83.9	0.8	2.9	5.0	0.2
	Uncert. %	0.1	0.1	0.4	0.0	0.1	0.0	0.1	0.1	0.5	0.1	0.1	0.2	0.1
12	**Atomic %**	4.2	2.0	87.2	0.6	2.4	3.4	2.9	2.2	88.5	1.1	1.5	3.6	0.1
	Uncert. %	0.1	0.1	0.4	0.0	0.1	0.2	0.1	0.1	0.5	0.1	0.1	0.2	0.0
13	**Atomic %**	3.4	1.8	85.4	0.6	3.9	4.6	4.5	1.7	84.0	0.9	3.7	5.0	0.3
	Uncert. %	0.1	0.1	0.4	0.0	0.1	0.2	0.1	0.1	0.5	0.1	0.2	0.2	0.1
14	**Atomic %**	10.7	1.4	71.8	1.5	6.6	7.7	10.5	1.8	72.6	2.6	5.2	6.8	0.4
	Uncert. %	0.3	0.1	0.6	0.1	0.3	0.3	0.3	0.1	0.7	0.1	0.3	0.4	0.1
15	**Atomic %**	4.7	1.9	81.2	1.3	3.8	6.3	6.3	1.8	82.6	1.4	3.2	4.5	0.1
	Uncert. %	0.2	0.1	0.6	0.1	0.2	0.3	0.2	0.1	0.6	0.1	0.2	0.3	0.1
16	**Atomic %**	(no data)						33.3	0.9	61.9	3.4		0.5	
	Uncert. %							1.0	0.2	1.3	0.3		0.3	
17	**Atomic %**							19.9	1.3	74.1	3.4		1.3	
	Uncert. %							0.7	0.2	1.2	0.3		0.4	
							0 min							5 min

Table F.2: EDX measurements of the precipitates (#1–15) and parts of the matrix (#16–17) as marked in Figure 7.5; after 15 and 60 minutes of electrolyte exposure, respectively.

#	Element	O (K)	Mg (K)	Al (K)	Si (K)	Mn (K)	Cu (K)	Ce (M)	O (K)	Mg (K)	Al (K)	Si (K)	Mn (K)	Cu (K)	Ce (M)
	Detector Correction	**0.51**	**0.88**	**0.92**	**0.92**	**0.99**	**0.99**	**0.99**	**0.51**	**0.88**	**0.92**	**0.92**	**0.99**	**0.99**	**0.99**
	k-factor	**1.889**	**1.050**	**1.030**	**1.000**	**1.372**	**1.663**	**1.532**	**1.889**	**1.050**	**1.030**	**1.000**	**1.372**	**1.663**	**1.532**
1	**Atomic %**	12.1	1.2	68.6	1.5	8.9	7.2	0.5	6.1		35.0	1.3	4.9	52.5	0.2
	Uncert. %	0.2	0.1	0.4	0.1	0.2	0.3	0.1	0.1		0.3	0.1	0.2	0.6	0.1
2	**Atomic %**	20.9	1.2	61.2	4.4	5.2	6.4	0.7	27.0	0.8	58.5	3.9	4.1	5.2	0.5
	Uncert. %	0.3	0.1	0.5	0.1	0.2	0.3	0.1	0.6	0.1	0.9	0.2	0.4	0.5	0.1
3	**Atomic %**	17.0	1.5	64.6	3.1	5.8	7.4	0.5	23.2	1.5	63.3	2.9	4.2	4.9	0.2
	Uncert. %	0.3	0.1	0.4	0.1	0.2	0.3	0.1	0.5	0.1	0.8	0.2	0.4	0.4	0.1
4	**Atomic %**	13.5	0.8	65.0	3.3	8.2	8.6	0.6	12.5		63.3	3.1	10.6	9.9	0.5
	Uncert. %	0.2	0.1	0.4	0.1	0.2	0.2	0.1	0.4		0.8	0.2	0.5	0.5	0.1
5	**Atomic %**	6.4	2.2	82.6	1.5	2.8	4.5	0.1	6.0	2.5	83.0	1.1	3.1	4.3	
	Uncert. %	0.1	0.1	0.4	0.0	0.1	0.2	0.0	0.2	0.1	0.7	0.1	0.2	0.3	
6	**Atomic %**	8.0	1.3	77.2	1.7	5.8	5.6	0.5	8.4	1.7	72.3	1.4	6.6	8.8	0.5
	Uncert. %	0.1	0.1	0.3	0.1	0.1	0.2	0.1	0.2	0.1	0.6	0.1	0.2	0.4	0.1
7	**Atomic %**	6.7	2.3	82.9	0.9	2.4	4.4	0.4	8.3	2.1	79.4	1.4	1.6	7.2	0.1
	Uncert. %	0.1	0.1	0.3	0.0	0.1	0.1	0.0	0.2	0.1	0.6	0.1	0.1	0.3	0.1
8	**Atomic %**	5.5	2.1	82.8	1.2	3.4	4.8	0.3	6.8	1.5	84.1	1.3	1.9	4.1	0.3
	Uncert. %	0.1	0.0	0.3	0.0	0.1	0.1	0.0	0.2	0.1	0.6	0.1	0.1	0.2	0.0
9	**Atomic %**	5.2	1.6	82.4	1.6	3.5	5.4	0.3	7.1	1.7	83.5	0.8	2.1	4.6	0.2
	Uncert. %	0.1	0.1	0.3	0.0	0.1	0.1	0.0	0.2	0.1	0.6	0.1	0.2	0.3	0.0
10	**Atomic %**	6.3	1.9	80.9	1.7	4.2	4.7	0.3	7.4	1.7	82.7	1.6	2.4	4.0	0.2
	Uncert. %	0.1	0.0	0.3	0.0	0.1	0.1	0.0	0.2	0.1	0.6	0.1	0.2	0.3	0.1
11	**Atomic %**	6.5	1.9	82.4	1.3	3.3	4.2	0.4	5.8	1.4	87.2	0.8	1.4	3.3	0.2
	Uncert. %	0.1	0.0	0.3	0.0	0.1	0.1	0.0	0.2	0.1	0.6	0.1	0.1	0.2	0.0
12	**Atomic %**	5.0	1.8	77.4	0.8	0.3	13.7	1.0	6.0	1.2	86.1	0.8		14.1	
	Uncert. %	0.1	0.0	0.3	0.0	0.0	0.2	0.0	0.2	0.1	0.6	0.1		0.3	
13	**Atomic %**	4.9	1.4	82.9	1.0	4.4	5.1	0.3	6.4	2.3	85.2	0.8	2.1	3.5	0.3
	Uncert. %	0.1	0.0	0.3	0.0	0.1	0.1	0.0	0.2	0.1	0.6	0.1	0.1	0.2	0.1
14	**Atomic %**	15.1	1.3	70.9	2.1	4.9	5.4	0.4	14.0	1.7	70.1	2.0	4.7	7.0	0.5
	Uncert. %	0.2	0.1	0.4	0.1	0.2	0.1	0.1	0.5	0.1	0.8	0.2	0.4	0.5	0.1
15	**Atomic %**	8.9	2.0	76.2	1.6	4.5	6.3	0.3	9.3	1.7	77.4	1.2	3.5	6.5	0.3
	Uncert. %	0.1	0.1	0.4	0.1	0.1	0.2	0.1	0.3	0.1	0.7	0.1	0.2	0.3	0.1
16	**Atomic %**	40.3	1.3	55.6	2.8				29.8	0.7	67.4	2.1			
	Uncert. %	0.7	0.1	0.7	0.2				0.9	0.2	1.1	0.2			
17	**Atomic %**	29.5	1.0	63.3	4.0		2.2		27.5	2.8	66.7	3.0			
	Uncert. %	0.6	0.1	0.8	0.2		0.3		1.0	0.2	1.3	0.3			
								15 min							60 min

As the values detected for Ce are below the accuracy of EDX, the variation of Ce from EDX for this study has been discredited. EEL spectra show Ce, but the compound formed being unstable under the electron beam, it is necessary for the future studies to stabilise the compound or use alternative techniques to detect Ce.

Chapter 8 CONCLUSIONS AND FUTURE WORK

1. Conclusions:

In this study, application of several TEM techniques to understand the structure, and one of the most important properties, corrosion, of aluminium (Al) alloys is presented. The key results from the *in situ* heat-treatment and corrosion studies are:

1. The *in situ* heating combined with (S)TEM imaging has been successful in following the various stages of precipitation in Al alloys: formation of clusters of solute atoms, nucleation of precipitates on dislocations, growth of lath-like intermediate precipitates and the distribution of these precipitates in three dimensions and with nanoscale precision.[1]
2. By imaging at a sub-micron scale while heating, it has been possible to gain the following insights while heating a specimen of commercial AA 2024-T3:
    a. Heating from 180 °C upwards results in redistribution of copper (Cu), along with a change in the size of the grain-boundary precipitates enriched in Cu. The grain boundaries also containing magnesium (Mg) are responsible for a localised corrosion attack.
    b. From 220 °C upwards, the formation of lath-like nanoprecipitates is observed. These precipitates have been identified as Cu, Mg rich S-phase type precipitates.
    c. The rate of precipitation of the lath-type precipitates varies with the temperature. The precipitates reach their maximum length, ~ 120 nm, approximately the thickness of the foil, in nearly 18 minutes when heated at 225 °C, while the same length is reached within 2 minutes at 250 °C and approximately 1 minute at 270 °C.
    d. Analysing the length versus time profiles of the precipitates at 225 °C shows the classical volume diffusion controlled growth.
    e. Heating beyond 300 °C causes the precipitates to dissolve. At 330 °C, the nanoprecipitates dissolve completely into the matrix, whereupon the Cu-rich grain-boundary precipitates start to shrink. Heating gradually from 330 to 410 °C causes most of the Cu to dissolve from the precipitates to the matrix.
    f. Throughout the heating process, manganese (Mn) rich precipitates remain intact.

3. Although there is an influence of the surfaces, there is an excellent correspondence between the *in situ* measurements on a submicron specimen and *ex situ* experiments on bulk from the literature. The shape and evolution of the precipitates are very similar.
4. In addition to the increased speed of the dynamic structural analysis, it is now possible to observe the evolution of 'individual' precipitates. For example, with the technology to achieve HR-STEM combined with *in situ* specimen heating, it is possible to predict models for precipitate growth.
    a. For instance, in case of the S-type precipitates growing at 200 °C in AA2024-T3, the Cu $(210)_{Al}$ planes, where in the neighbouring (210) plane Al is replaced by Mg (Mg is larger than Al and Cu smaller than Al, compensating largely each other's volume change) forms a Cu-Mg slab. Through a sequence of varying slab-slab distance, different S-type compositions arise.
5. From the *ex situ* corrosion experiments,[2] it has to be noted that while carrying out corrosion experiments on TEM specimens, it is advisable to avoid salt solutions of high concentrations as there is a possibility of salt crystal precipitation on the area of interest or complete dissolution of the area of interest.
6. Exposure to oxygen (O_2) bubbled through aqueous (aq.) hydrochloric acid (HCl) of pH=3 seems to be a good environment to carry out *in situ* corrosion studies on AA 2024-T3.
7. Using the quasi *in situ* studies,[3] by following a specific specimen area after repeated exposure to O_2 bubbled through aq. HCl of pH=3, de-alloying of a grain-boundary precipitate of ~200 nm is observed by monitoring the changes in the EELS Cu-$L_{2,3}$-edge and EFTEM elemental maps.
8. The *in situ* corrosion experiments[4] show the possibility to carry out chemical reactions in aggressive environments in the TEM.
    a. From the studies on AA 2024-T3, the moments of initiation of corrosion, the way the corrosive attack of an anodic precipitate as well as the attack around a cathodic precipitate has been documented.
    b. Compared to the existing quasi *in situ* methods based on surface probe microscopy to monitor corrosion, this is a major step forward in observing changes during corrosion on a sub-micron scale.
9. The preliminary quasi *in situ* corrosion inhibition studies show promising results in the direction of understanding the mechanism of corrosion protection by cathodic inhibitors.

2. Suggestions for future work

The *in situ* heat-treatment experiments and the current approach, i.e. *ex situ* and quasi *in situ* experiments prior to *in situ* corrosion experiments have opened up several possibilities for many interesting future studies. While the heat-treatment and the tomography experiments combined with the compositional analysis can be extended to several new alloy systems as well as other materials on one hand, the combination of heating and chemical reactions in the nanoreactor is a very exciting possibility. For instance, the microstructural changes corresponding to the grain boundary precipitates, as well as the precipitation of S-type phases which are anodic with respect to the aluminium matrix are highly detrimental for the corrosion behaviour of these alloys. Combining these microstructural changes with the *in situ* corrosion experiments gives the possibility to simulate some of the changes an engineering alloy goes through during its lifetime, on a sub-micron scale. These sorts of studies combined with compositional analysis and the possibility to evaluate the changes in 3-dimensions provides a wealth of knowledge on developing new alloy systems too.

Another interesting application of the combined heating and *in situ* chemical reactions could be in the area of steels. Stainless steels, though known to have very good corrosion resistance are prone to intergranular corrosion if they undergo sensitisation,[5,6] i.e. during operations like welding or any other process that could lead to an increase in the temperature within a range of 420 – 850 °C for prolonged durations, the precipitation of carbide phases at grain boundaries makes them prone to localised corrosion. Preliminary *in situ* heat-treatment experiments on stainless steel 316 have already shown some phase transformations.

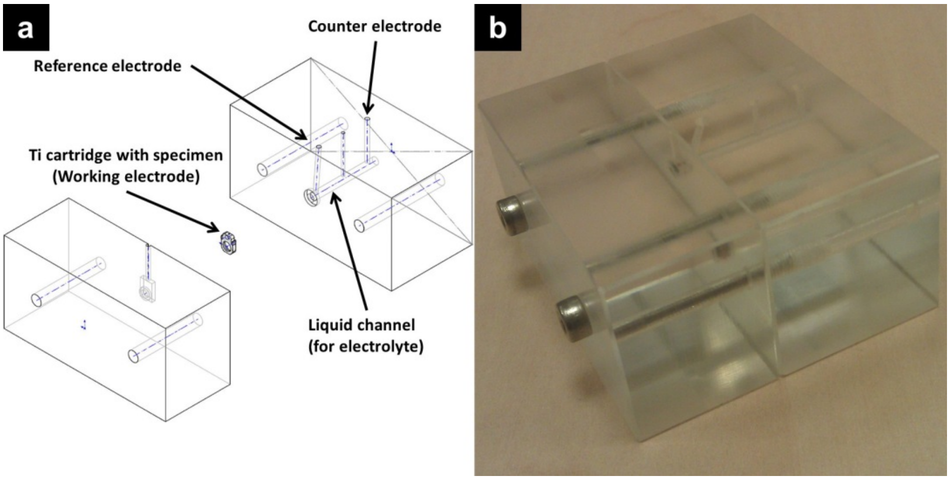

Figure 8.1: (a) Conceptual sketch and (b) photograph of an electrochemical cell developed for quasi in situ electrochemical studies involving TEM. The cell consists of two halves made of Perspex, with a fluid channel and electrodes in one half and groove to embed a cartridge containing TEM specimen on the other.

The possibility to combine TEM investigations with electrochemical experiments is another exciting prospect. This could be possible either by quasi *in situ* as well as *in situ* experiments. For the quasi *in situ* experiments, an electrochemical cell where the cartridge for the quasi *in situ* holder (made of titanium) can be used as a working electrode has already been developed, Figure 8.1. Using this method, it is possible to carryout TEM investigations at intermediate stages of an electrochemical experiment.

In order to carry out *in situ* electrochemical experiments, it is necessary to combine the ideas from the nanoreactor with an electrical measurement setup. While the gas reactor has been shown in this study, it is also possible to use the nanoreactor with liquids in-between the two halves. It has successfully been shown that it is possible to carry out electrical measurements within the TEM using MEMS based devices.[7] By combining these two concepts of liquid cell nanoreactors and *in situ* electrical measurements, it should be possible to build devices not just for *in situ* electrochemical studies but also for many other exciting *in situ* TEM investigations.

References:

1 Malladi, S. K. *et al.* Real-Time Atomic Scale Imaging of Nanostructural Evolution in Aluminum Alloys. *Nano Lett.*, doi:10.1021/nl404565j (2013).

2 Malladi, S. R. K. *et al.* Early stages during localized corrosion of AA2024 TEM specimens in chloride environment. *Surface and Interface Analysis*, n/a-n/a, doi:10.1002/sia.5193 (2012).

3 Malladi, S. R. K. *et al.* Quasi *in situ* analytical TEM to investigate electrochemically induced microstructural changes in alloys: AA2024-T3 as an example. *Corrosion Science* **69**, 221-225, doi:10.1016/j.corsci.2012.12.006 (2013).

4 Malladi, S. *et al.* Localised corrosion in aluminium alloy 2024-T3 using *in situ* TEM. *Chemical Communications* **49**, 10859-10861, doi:10.1039/c3cc46673f (2013).

5 Briant, C. L., Mulford, R. A. & Hall, E. L. Sensitization of Austenitic Stainless Steels, I. Controlled Purity Alloys. *Corrosion* **38**, 468-477, doi:10.5006/1.3577362 (1982).

6 Mulford, R. A., Hall, E. L. & Briant, C. L. Sensitization of Austenitic Stainless Steels II. Commercial Purity Alloys. *Corrosion* **39**, 132-143, doi:10.5006/1.3580828 (1983).

7 Rudneva, M., Zandbergen, H. W., In-situ Electrical Measurements in Transmission Electron Microscopy (Casimir PhD series, 2013).

SUMMARY

Transmission electron microscopy (TEM) has been well known as a powerful characterisation tool to understand the structure and composition of various materials down to the atomic level. Over the years, several TEM studies have been carried out to understand the compositional, structural and morphological changes a material undergoes as a consequence of an external stimulus (thermal, environmental, electrical as well as mechanical) *post mortem*. With the recent advancements in the areas of TEM and microelectronics, it is now possible to integrate the external stimuli in the TEM, making it possible to carry out *in situ* TEM studies. In the present study, we have used microelectromechanical system (MEMS) based devices to investigate heat-treatment and corrosion *in situ* in a commercial aluminium alloy, AA 2024-T3.

Aluminium alloys go through several thermal and mechanical treatments before a final product is formed and during these processes, they undergo a complex compositional and structural evolution at the atomic level which in turn influences their properties like mechanical strength and resistance to corrosion. One of the common microstructural features of most of the commercial alloys is the formation of numerous nanometre sized second phase particles, known as intermetallic precipitates during heat-treatment. By investigating different samples taken at intermediate stages during the heat-treatment of bulk samples, a sequence of precipitation and its influence on the mechanical properties has been established. However, a link between all these stages by investigating the same location in one sample as a function of time and temperature is missing. In this study, using *in situ* heating in a high-resolution scanning transmission electron microscope (STEM), we have investigated the three-dimensional compositional and structural evolution of metal alloys during heat treatments, revealing in unparalleled detail where and how precipitates nucleate, grow or dissolve.

The next part of the study is related to the influence of the nanoscale intermetallic particles on the corrosion behaviour of aluminium alloys. Due to the differences in the electrochemical potentials between the intermetallic phases and the aluminium matrix, most of the commercial aluminium alloys are highly susceptible to a localised corrosive attack. This phenomenon has been well investigated by quite a few *ex situ* electrochemical methods combined with analytical microscopic techniques. Here, we investigate the corrosion *in situ* in a gas-liquid-material system using a functional MEMS device called nanoreactor. As there have been no TEM studies investigating electrochemical corrosion of aluminium alloys *in situ* in a TEM, we have decided to investigate the well-studied AA2024-T3 alloy system to validate our approach.

In order to determine a suitable experimental window prior to the *in situ* TEM studies, we have carried out *ex situ* and quasi *in situ* corrosion studies on conventional TEM specimens. Using analytical TEM studies like electron energy loss spectroscopy (EELS), energy filtered TEM (EFTEM) and energy dispersive spectroscopy of X-rays (EDX), we observe that oxygen bubbled through aqueous HCl is a suitable environment for carrying out *in situ* corrosion experiments in the TEM at room temperature. Using these conditions, we have investigated the initiation of localised corrosive attack in AA2024-T3. Finally, using our quasi *in situ* approach, we have also carried out some preliminary investigations on understanding the corrosion inhibition mechanisms of Ce-based inhibitors.

The *in situ* TEM heat-treatment and analytical techniques used in this study are expected to accelerate investigations on new alloy compositions suggested by computational methods. Environmental TEM studies using the nanoreactor can be extended to investigate microstructural and morphological changes during chemical reactions in various gas-liquid-material systems on the nanoscale, combined with the influence of temperature. Therefore, this study expands the scope of TEM as not just a characterisation tool, but also as a laboratory to carry out many interesting *in situ* experiments on the nanoscale.

SAMENVATTING

Transmissie-elektronenmicroscopie (TEM) is een bekend en krachtig gereedschap om de structuur en samenstelling van materialen te karakteriseren tot op atomair niveau. Door de jaren heen zijn er vele *post mortem* TEM studies uitgevoerd om veranderingen in de samenstelling, structuur en vorm van materialen te begrijpen als gevolg van externe stimuli (thermisch, gas, elektrisch of mechanisch). Door de recente vooruitgang op het gebied van TEM en micro-elektronica is het nu mogelijk om externe stimuli in de TEM aan te bieden aan een materiaal, genaamd *in situ* TEM. In de huidige studie hebben we micro-elektromechanische systemen (MEMS) gebruikt om warmtebehandeling en corrosie van de commerciële aluminium legering AA 2024-T3 *in situ* te onderzoeken.

Aluminium legeringen ondergaan verscheidene thermische en mechanische behandelingen voordat er een uiteindelijk product ontstaat. Tijdens deze behandelingen vinden er complexe veranderingen plaats in samenstelling en structuur op atomair niveau, wat weer eigenschappen als mechanische sterkte en corrosiebestendigheid van de legering beïnvloedt. Een gangbare microstructureel verschijnsel tijdens de warmtebehandeling van de meeste commerciële legeringen is de vorming van talrijke nanometers grote tweede-fase deeltjes, ofwel intermetallische precipitaten. Door verschillende monsters te nemen van bulk legeringen op verschillende momenten tijdens de warmtebehandeling is precipitaatvorming en haar invloed op mechanische eigenschappen in kaart gebracht. Echter, een direct verband tussen deze stadia door bestudering van dezelfde locatie in hetzelfde monster als functie van tijd en temperatuur ontbreekt. In deze studie is *in situ* verhitting van legeringen in een raster (scanning) transmissie-elektronenmicroscoop (STEM) gebruikt om de driedimensionale evolutie van samenstelling en structuur tijdens een warmtebehandeling te bestuderen in niet eerder vertoond detail, met name wat betreft de nucleatie, groei en verdwijning van precipitaten.

Het volgende deel van de studie is gewijd aan de invloed van de nanometers grote intermetallische deeltjes op het corrosiegedrag van aluminium legeringen. Door het verschil in de elektrochemische potentiaal tussen de intermetallische fasen en de aluminium matrix zijn de commerciële aluminium legeringen erg gevoelig voor lokale corrosie initiatie. Dit fenomeen is uitgebreid onderzocht in een aanzienlijk aantal *ex situ* elektrochemische studies in combinatie met analytische microscooptechnieken. In deze studie is de corrosie *in situ* onderzocht in een gas-vloeistof-materiaal systeem met behulp van een MEMS device, nanoreactor genaamd. Omdat deze *in situ* methode in een TEM niet eerder is toegepast voor de bestudering van elektrochemische corrosie, hebben we besloten de methode te valideren met de bekende AA2024-T3 legering.

Om de geschikte experimentele conditie vast te stellen hebben we eerst *ex situ* en quasi *in situ* corrosie studies verricht aan conventionele TEM preparaten. Gebruik makend van analytische TEM methoden als elektron-energie-verlies-spectroscopie (EELS), energie gefilterde TEM (EFTEM) en energie dispersieve röntgenspectroscopie (EDX), hebben we geconstateerd een gas bestaande uit zuurstof, HCl en water een reagens is voor *in situ* TEM corrosie studies bij kamertemperatuur. Hiervan gebruik makend hebben we de lokale corrosie initiatie bestudeerd in AA2024-T3. Tot slot hebben we ook onze quasi *in situ* benadering gebruikt voor enkele voorstudies van de corrosie remmende werking van op Ce gebaseerde stoffen.

De in deze studie gebruikte *in situ* TEM technieken en analytische methoden kunnen toekomstige studies aan nieuwe legeringen zoals gesuggereerd door berekeningen versnellen. *In situ* TEM met nanoreactoren kan uitgebreid worden naar onderzoek van microstructurele en morfologische veranderingen tijdens chemische reacties in verscheidene gas-vloeistof-materiaal systemen op de nanoschaal, ook gecombineerd met temperatuursveranderingen. Zodoende vergroot deze studie de horizon van TEM niet alleen als karakteriseringsgereedschap, maar ook als laboratorium om vele interessante *in situ* experimenten te doen op de nanoschaal.

ACKNOWLEDGEMENTS

This book is a result of inspiration, guidance, support and contribution from several wonderful people I came across during the four years spent at the National Centre for HREM, TU Delft. The book would remain incomplete without expressing my gratitude to all of them.

I can never forget the warm welcome from my supervisors when I first came to the Netherlands for my PhD interview. Joining the group of Prof.dr. Henny Zandbergen was an instantaneous decision. Henny is probably the best experimentalist I have ever seen and his enthusiasm to carry out an experiment has always been the same right from day one. He is always ready with a solution to deal with the experimental challenges and has designed and got at least *five* TEM holders manufactured, specifically for this study. His creative inputs, scientific acumen and above all his ability to inspire have been the main driving force for completing my PhD. I would always be indebted to him and wish him many more years of enthusiastic experimenting. Hopefully, I can learn how he does it someday. Operating a complicated instrument like a TEM needs very precise guidance and I cannot imagine any better guidance than from my daily supervisor, Dr.ir. Frans Tichelaar. Frans has not only taught me how to handle the microscope but also how to approach and plan experiments as well as present the results in a systematic manner. Henny and Frans have always been available for interesting discussions and joined the experiments on several occasions, I could not have asked for any better guidance for my PhD.

Next I would like to thank my paranymphs, Maria and Qiang. Qiang has been my true mentor in every sense and has played a significant role in not just refining my TEM abilities but also developing my personality by being critical when required and not allowing me to lose my focus. And Maria, she has been one of the best, all-rounded personalities I have ever come across. She has not just been a wonderful neighbour but also a great friend. I hope I can learn from her how to balance work and life outside work. These two people have always been there for me and would like to thank them from the bottom of my heart.

Working at TU Delft and working with M2i has provided me great opportunities for fruitful collaboration with academia and industry. I would like to take this opportunity to thank Dr.ir. Arjan Mol and Prof.dr. Herman Terryn. The discussions with them on corrosion have been very informative and productive. I would also like to thank my industrial partners Dr. Fouzia Hannour (TATA Steel) and Dr. Hans Mulders (FEI Company) and my program manager Dr. Derk Bol for their support. I would like to

thank Dr. Marijn van Huis (now at University of Utrecht) for his encouragement and theoretical inputs in making the conclusions from my experimental results stronger. The collaboration with Dr. Joost Batenburg (CWI Amsterdam and University of Antwerp) to reveal the 3-dimensional information from tomography has been one of the most significant results from my study and I would like to thank Joost for his timely reconstructions. I had the chance to collaborate with the group of Prof. Aleksandra Czyrska-Filemonowicz at AGH Krakow and I would like to thank her and Dr. Beata Dubiel for their hospitality and for allowing us to use their microscope.

None of this scientific work would have progressed smoothly without the managerial support from our group secretary, Marijke van der Veen as well as the HR department from M2i Office. I would like to thank Marijke, Monica Reulink and Gitty Bouman (at M2i), Sharon Djadoenath (formerly at M2i) for all their support in helping me settle down at my work place without ever being worried about any legal procedures.

There is one law that is valid most of the times in experimental research, Murphy's Law, and Tom de Kruijff has always been geared-up to combat it as much as possible. The technical support from Dr. Vasili Svetchnikov, Dr. Ulrike Ziese, Danny de Gans, Jan Groen, Leon van Luijk, Eef Grafhorst, and Merlijn Camp has been crucial in completing my experiments. I would like to thank all of them for their prompt technical support. Special thanks to Dr. Gregory Pandraud and Dr. Chenggang Shen for their relentless efforts to produce the MEMS devices, which are the most important components for *in situ* TEM studies. The spontaneous support from Dr. Paul Alkemade and Hozanna Miro whenever I had any issues with the FIB is also highly appreciated.

A big thanks to several current and former group members: Jouk (for very interesting and informative scientific discussions as well as non-scientific discussions on cricket), Mauro (my first office mate and thanks for helping me settle in Delft), Adrian (my FIB mentor); for interesting discussions and tips from Emrah, Chang-Ming, Ganesh and Meng-Yue; for having pleasant conversations and being wonderful colleagues- Anil, Shiv, Tatiana, Chao, Masha (these people started working around the same time and changed the dynamics of our group), Leonardo (the boss), Ahmet and Chunhui; Dieter and Jelle (the youngest ones, great fun having them in my office and always kept me on my toes).

I would also like to thank many people outside the group for making my stay in the Netherlands memorable: Igor, Dilyana, Eric (with frequent visits from Leiden), Önnaz, Farid, Hugo, Jose, Yaiza (from 3mE), Eric, Sander (fussball buddies), Olaf and Ben (from DENS), Greg Schneider (now at Leiden), Ben Schneider (also neighbour and a great friend), Abrar, Girish, Govind, Jai, Krishna, Mallesh, Murali, Venkat, Venkatesh, Waqas, Zubair (friends from the Indian subcontinent) and most importantly the Ajax Zami Selectie (without a doubt the best team for ultimate fun in the Netherlands); special thanks to the affectionate and welcoming families: Sharmila-bodi and Shibu-da, Xiaoli and Qiang; Renuka and Vijayendar garlu; Anna and Bart Duijndam (also for providing me a great place to stay).

During a PhD, there are phases of extreme joy, which can be shared with everyone; and extremely frustrating times, which I could only vent on my family. Though they have physically not been with me, I am not sure how to thank my parents and my brother for their love and support, despite my occasional rude behaviour and lack of communication.

Finally, I would like to thank my 'guru' to whom I have dedicated this thesis, Late Prof. R. Balasubramaniam (more popular as Bala sir among his students). He not only introduced me to the area of electrochemistry and corrosion but also motivated me to pursue a career in science seriously. It is really unfortunate that he passed away at a very young age and his sudden demise is an irreparable loss to the Indian scientific community. The time spent at Kanpur and during my undergraduate studies introduced me to some of the most amazing teachers and great individuals I would like to take this opportunity to thank a few of my teachers, Dr. Gouthama, Dr. Rajiv Shekar, Dr. K.N. Rai, Dr. B. Basu and Dr. J. Viplava Kumar. Some of the courses they taught have been extremely useful even for my PhD studies.

I consider myself extremely fortunate to have been in the company of all the wonderful people mentioned here.

Sairam Malladi
Delft, January 2014

CURRICULUM VITÆ

Sairam K Malladi

born on 8th May 1986 in Hyderabad, India

December 2013 – Present
Postdoctoral Research Fellow
Kavli Institute of Nanoscience Delft,
Technische Universiteit Delft, Delft, The Netherlands

September 2009 – November 2013
Doctor of Philosophy in Applied Physics
Kavli Institute of Nanoscience Delft,
Technische Universiteit Delft, Delft, The Netherlands
Thesis: In-situ TEM Studies: Heat-treatment and Corrosion
Promotor: Prof.dr. H.W. Zandbergen
Worked on Materials Innovation Institute (M2i) project in collaboration with TATA Steel and FEI company

July 2007 – July 2009
Master of Technology in Materials Science and Engineering
Indian Institute of Technology Kanpur, Kanpur, India
Thesis: Novel Polarization Method for Optimizing Electrodeposition of Specular Nanocrystalline Nickel
Promotor: Prof.dr. R. Balasubramaniam
Award for Academic Excellence, 2007 – 08 for securing perfect CPI of 10.0/10.0

September 2003 – May 2007
Bachelor of Technology in Metallurgy and Materials Technology
Mahatma Gandhi Institute of Technology, Jawaharlal Nehru Technological University, Hyderabad, India
First class with distinction

PUBLICATIONS

In peer reviewed journals

Directly related to the thesis:

1. Malladi SRK, Xu Q, U Ziese, Tichelaar FD, Zandbergen HW. Order-disorder transformations in Cu_3Au to calibrate MEMS based heaters for *in situ* TEM studies. Ultramicroscopy 2014 (in preparation).
2. Malladi SRK, Stap JH, González-García Y, Tichelaar FD, Mol JMC, Zandbergen HW. Corrosion inhibition studies on aluminium alloy 2024-T3 in NaCl-$CeCl_3$ solutions. Corrosion Science 2014 (in preparation).
3. Malladi SK, Xu Q, van Huis MA, Tichelaar FD, Batenburg KJ, Yücelen E, Dubiel B, Czyrska-Filemonowicz A, Zandbergen H. Real-Time Atomic Scale Imaging of Nanostructural Evolution in Aluminum Alloys. Nano Letters 2013.
4. Malladi S, Shen C, Xu Q, de Kruijff T, Yücelen E, Tichelaar F, Zandbergen H. Localised corrosion in aluminium alloy 2024-T3 using in situ TEM. Chemical Communications 2013.
5. Malladi SRK, Tichelaar FD, Xu Q, Wu MY, Terryn H, Mol JMC, Hannour F, Zandbergen HW. Quasi *in situ* analytical TEM to investigate electrochemically induced microstructural changes in alloys: AA2024-T3 as an example. Corrosion Science 2012.
6. Malladi SRK, Xu Q, Tichelaar FD, Zandbergen HW, Hannour F, Mol JMC, Terryn H. Early stages during localized corrosion of AA2024 TEM specimens in chloride environment. Surface and Interface Analysis 2012.

Other collaborative work:

7. Hellmann R, Cotte S, Cadel E, Malladi S, Karlsson LS, Lozano-Perez S, Cabié M, Seyeux A. Nanometre-scale evidence for dissolution-reprecipitation control of silicate glass corrosion. Science 2014 (submitted)
8. Du S, Lin K, Malladi S, Lu Y, Xu Q, Steinberger-Wilckens R, Dong H. A simple approach for PtNi–MWCNT hybrid nanostructures as high performance electrocatalysts for the oxygen reduction reaction. Nano Letters 2014 (submitted)
9. Du S, Lu Y, Malladi SK, Xu Q, Steinberger-Wilckens R. A simple approach for PtNi–MWCNT hybrid nanostructures as high performance electrocatalysts for the oxygen reduction reaction. Journal of Materials Chemistry A 2014.
10. Schneider GF, Xu Q, Hage S, Luik S, Spoor JNH, Malladi S, Zandbergen H, Dekker C. Tailoring the hydrophobicity of graphene for its use as nanopores for DNA translocation. Nature Communications 2013.

11. Rudneva M, van Veldhoven E, Malladi SK, Maas D, Zandbergen HW. Novel nanosample preparation with a helium ion microscope. Journal of Materials Research 2013.
12. Xu Q, Wu M-Y, Schneider GF, Houben L, Malladi SK, Dekker C, Yucelen E, Dunin-Borkowski RE, Zandbergen HW. Controllable Atomic Scale Patterning of Freestanding Monolayer Graphene at Elevated Temperature. ACS NANO 2013.

In international conferences

Directly related to the thesis:

13. Sairam K Malladi, Meng-Yue Wu, Qiang Xu, Chunhui Liu, Ahmet Erdamar, Frans Tichelaar, Henny Zandbergen. Correlating *in situ* Heat-Treatment and Environmental TEM Studies in Aluminium Alloys. 2014 MRS Spring Meeting & Exhibit, April 21-25, 2014, San Francisco, California (Submitted).
14. S. R. K. Malladi, Q. Xu, C. Shen, G. Pandraud, F. D. Tichelaar, H. W. Zandbergen. Studies on localized corrosion in aluminium alloys using in situ transmission electron microscopy, in: Proceedings of the 15th European Microscopy Congress, EMC 2012, Manchester, United Kingdom, from 16th – 21st September 2012, (Oral Presentation)
15. S. R. K. Malladi, Q. Xu, G. Pandraud, F. D. Tichelaar, H. W. Zandbergen, K. Kulawik, B. Dubiel, A. Czyrska-Filemonowicz. Phase transformations in Al alloys during heat treatment investigated by in situ TEM, in: Proceedings of the 15th European Microscopy Congress, EMC 2012, Manchester, United Kingdom, from 16th – 21st September 2012, poster # 314, in session PS2.7, (Poster).
16. S. R. K. Malladi, Q. Xu, F. D. Tichelaar, H. W. Zandbergen, F. Hannour, J. M. C. Mol, H. Terryn. Ex situ TEM corrosion studies on aluminium alloy 2024-T3 in chloride environment, in: Proceedings of the VIth Aluminium Surface Science & Technology, ASST 2012, Sorrento, Italy, from 27th – 31st May 2012, abstract in pg. 91, article #25 in published proceedings (Oral Presentation).
17. S. R. K. Malladi, F. D. Tichelaar, H. W. Zandbergen. Quasi In-situ Oxidation Studies on Aluminum Alloy 2024-T3, 17th International Microscopy Congress (IMC17), Rio de Janeiro, Brazil, from 19 to 24 September 2010 (Poster).

Other collaborative work:

18. Rudneva M, van Veldhoven E, Malladi SK, Zandbergen HW. Application of Helium Ion Microscope for Sample Modification at Nanoscale. Microscopy and Microanalysis 2013;19:856.

19. Rudneva M, van Veldhoven E, Malladi S, Maas D, Zandbergen HW. Application of the Helium Ion Microscope as a Sculpting Tool for Nanosamples. MRS Proceedings 2012;1455.
20. Rudneva M, van Veldhoven E, Malladi S, Maas D, Zandbergen HW. Modification of the samples with helium ion microscope combined with local heating, in: Proceedings of the 15th European Microscopy Congress, EMC 2012, Manchester, United Kingdom, from 16th – 21st September 2012.